Int. J. Advanced Design and Manufacturing Technology, 2024, Vol. 17, No. 3, pp. 1-9

DOI: ***ISSN: 2252-0406*** ***https://admt.isfahan.iau.ir***

Online Reliable Chatter Detection of Milling Flexible Part Using Synthetic Criterion

Hosam Shadoud, Nahid Zabih Hosseinian, Behnam Moetakef-Imani *

Department of Mechanical Engineering,
Ferdowsi University of Mashhad, Iran
E-mail: hosam.shadoud@mail.um.ac.ir,
nahid.zabihhosseinian@ontariotechu.net, imani@um.ac.ir
*Corresponding author

Received: 1 June 2023, Revised: 26 February 2024, Accepted: 8 September 2024

Abstract: In machining processes, the self-excited vibration between the cutting tool and the workpiece is an important issue that can result in undesirable effects, for example, poor quality of the final surface, low dimensional accuracy, breakage of the tool, and excessive noise. To anticipate this problem, statistical features of the vibration signal, such as mean, variance, and standard deviation, have been extracted from online measurements. The synthesis criterion (SC), which is based on the standard deviation (STD) and the one-step autocorrelation function (OSAF), has been employed to detect quickly the threshold of chatter vibration. In this article, flexible workpieces with varying cutting depths have been selected to detect online chatter vibrations during milling operations. In order to collect an analog vibration signal, an STM32 card has been selected with a sampling rate up to 20 kSPS. A high-bandwidth, lightweight film piezoelectric sensor is attached to the workpiece. Unlike other sensors, such as load cells or acceleration sensors, the film piezoelectric sensors do not alter the dynamics of the system. In this research, cost-effective hardware is also developed to capture vibration signals reliably and efficiently. The experimental results confirm that the developed SC algorithm can efficiently predict the onset of chatter vibration as it was able to detect the onset of chatter vibrations within 0.18 sec. Thus, the SC algorithm can considerably enhance the milling operations of flexible parts.

Keywords: Chatter Vibrations, Flexible Parts, One-Step Autocorrelation Function (OSAF), Piezoelectric Sensor, Synthetic Criterion (SC)

Biographical notes: Hosam Shadoud received his BSc in Mechanical Engineering from Albaath University, located in the city of Homs in Syria. In pursuit of his Master's and PhD degrees, he opted to continue his studies at Ferdowsi University of Mashhad (FUM) in Iran, under the supervision of Prof. Moetakef-Imani. His research endeavors focus on the chatter detection vibrations in machining processes. **Nahid Zabih Hosseinian** completed her first master's degree at FUM, where she conducted research on decreasing the effect of undesired boring bar's vibrations via active Voice Coil Actuators (VCA). Currently, she continues her research as a second master at Ontario Tech University, Canada. **Behnam Moetakef-Imani** is a Professor of Mechanical Engineering at FUM university, in Iran. He received his PhD in Manufacturing from the McMaster University, Canada. His ongoing researches focus on CAD/CAM, Machining Dynamics, and various types of machining operations.

Research paper

1 INTRODUCTION

Milling is a highly complex process, involving the periodic cutting effects of the tool's cutting teeth on the workpiece. Regenerative waves are one of the most notable causes of self-excited or chatter vibration in milling, which can significantly impact the quality of the machined surface. Achieving a high material removal rate (MRR) and an acceptable surface quality are primary objectives of milling operations. However, as MRR increases, chatter vibrations tend to occur, necessitating the use of lower MRR and lower cutting depths to minimize undesirable interactions between tools and workpieces, as noted by Tlusty [1-2].

Dynamic vibrations play a crucial role in the cutting process due to the fluctuation of the dynamic cutting force and the flexibility of the tool and workpiece. Also, a stability lobe diagram has been developed to assist in the selection of stable cutting parameters [3-4]. In recent years, numerous research studies have been conducted with the aim of acquiring signals of chatter during the milling process. A range of sensors and signals have been employed for chatter detection, including cutting forces [5-6], vibration signals [7-9], servo current [10], sound [11-15], and acoustic emission [9].

Due to the complex non-linear characteristics of chatter during the machining process, several methods have been proposed for online chatter recognition in three distinct domains: frequency, time, and time-frequency. In this regard, a novel approach for online chatter detection based on the development of artificial neural networks was suggested by [11], [16-20]. Specifically, different schemes of the Self-organizing map (SOM) neural network, recursive neural network (RNN), and convolutional neural network (CNN) were utilized for representing the occurrence of chatter through signal feature processing and deep learning. While intelligent control systems proved to be effective for monitoring and recognizing chatter, the robustness, accuracy, and response rate of the neural network were heavily dependent on continuous self-learning, training, and testing processes [21].

In [22], a novel coherence function about the acceleration of the tool in the x direction and an audio signal chatter detection method was proposed for turning operations, which was evaluated for its ability to detect chatter in the early stages of machining in the frequency domain. The experimental findings indicate that this method was sensitive to the onset of chatter. However, this method was not entirely independent of the machining parameters, and therefore, the optimal threshold for chatter detection may need to be updated by adjusting the mentioned parameters. Besides, an on-line dependent chatter detection method in milling was investigated [23], and a discrete comb filtering method was suggested to isolate the chatter frequency.

A novel synthetic criterion (SC) for early chatter recognition proposed by [11], integrates standard deviation (STD) and one-step autocorrelation function (OSAF) for the online recognition of chatter vibrations. Furthermore, this paper presents a revised fast algorithm for OSAF that significantly improves the computational efficiency compared to the original SC algorithm, thereby saving valuable time for online suppression of chatter vibrations. The experimental setup involved the acquisition of vibration signals through two accelerometers mounted on the spindle house, thus enabling the validation and verification of the proposed SC method.

The work presented in this paper proposes a synthetic criterion (SC) for online chatter recognition. When the SC integrates standard deviation (STD) and One-Step Autocorrelation Function (OSAF), it results in an enhanced sensitivity and accuracy of chatter recognition compared to the traditional method [11]. The application of the SC method is a significant improvement in the detection of chatter vibrations during machining operations. The vibrations are captured by light weighted piezoelectric sensors that are mounted on workpieces of varying sizes. Unlike other sensors, they are distinguished by their ability to capture the vibration signals without altering the dynamics of the vibrating system. Additionally, these sensors are characterized by a high bandwidth and cost-effectiveness, making them a suitable choice for data collection purposes.

2 MODELING

Chatter vibrations are commonly observed when a machining process transitions from a stable stage to an unstable one. These signal vibrations involve three distinct stages: the stable stage, the transition stage, and the unstable stage [11]. While vibrations are negligible during the stable stage, they become more pronounced in the chatter stage. Therefore, the transition stage is particularly important for identifying chatter. Two changes occur in the transition stage: an increase in amplitude in the time domain and a shift in the dominant frequency band in the frequency domain, which lead to chatter vibrations.

This paper employs a synthesis criterion (SC) to identify chatter vibrations, which is based on the integration of the standard deviation (STD) and the one-step auto correlation function (OSAF), which will be described.

1.1. Standard Deviation (STD)

One of the characteristics of a signal is STD which provides insight into the trend of increasing signal amplitude in the frequency domain. This feature is defined by the following Equation:

$$\sigma = \sqrt{\frac{\sum_{i=1}^{N}(x_i - \bar{x})^2}{N-1}} \quad (1)$$

Where, x_i is the sampled data, $\bar{x}$ is defined as the average data and N is the number of samples.

1.2. One-Step Auto Correlation Function (OSAF)

For processing random signals, OSAF is a beneficial method. It also defines the interdependence of a signal at one particular moment on the same signal at a different moment, within the time domain. If the sampling interval for chatter vibration is selected correctly, the OSAF can detect changes in the dominant frequency. A simple harmonic signal is defined by:

$$x_i(t) = A_i \, sin(2\pi f_i t + \theta_i) \quad (2)$$

Where, θ_i is considered to be a random variable. The expression of the OSAF according to the autocorrelation function is represented as follows:

$$\rho_{1i} = cos \, 2\pi f_i \Delta \quad (3)$$

The sampling interval (Δ) is determined based on the Nyquist frequency $f_n = 1/(2\Delta)$. Additionally, f_i increases as ρ_{1i} decreases. Harmonic vibration signals can be represented by the following:

$$x(t) = \sum_{i=1}^{n} x_i(t) = \sum_{i=1}^{n} A_i \, sin(2\pi f_i t + \theta_i) \quad (4)$$

The original algorithm of OSAF for this condition is as follows:

$$\rho_1 = \frac{\sum_{i=1}^{n} A_i^2 \, cos(2\pi f_i \Delta)}{\sum_{i=1}^{n} A_i^2} = \frac{\sum_{i=1}^{n} A_i^2 \rho_{1i}}{\sum_{i=1}^{n} A_i^2} \quad (5)$$

In this Equation, A_i^2 is replaced by $S(f_i)$,the power spectrum, in i[th] frequency (f_i). So, the following Equation will be obtained:

$$\rho_1 = \frac{\sum_{i=1}^{n} S(f_i) \, cos(2\pi f_i \Delta)}{\sum_{i=1}^{n} S(f_i)} \quad (6)$$

According to the aforementioned Equation, the original algorithm of OSAF has a monotonic relationship between ρ_1 and the dominant frequency band [11].

1.3. The Fast Algorithm of OSAF

To calculate OSAF in "Eq. (6)", the power spectrum function $S(f_i)$ should be calculated using the discrete fourier transform (DFT) method. Therefore, to improve the computational efficiently, a fast algorithm for OSAF was introduced in [11], which can detect vibration signals online. Fast OSAF calculates the required time series directly as follows:

$$\rho_1 = \frac{NC - A^2}{NB - A^2} \quad (7)$$

A, B, and C parameters are:

$$A = \sum_{i=1}^{N} x_i, \; B = \sum_{i=1}^{N} x_i^2, \; C = \sum_{i=1}^{N} x_i \, x_{i-1} \quad (8)$$

In this research, N refers to experimental samples that have been acquired at each sliding window. Furthermore, the computational efficiency of OSAF was improved by implementing "Eq. (7)", which outperforms "Eq. (6)".

1.4. Synthesis Criterion (SC)

The STD is a value that indicates the magnitude of variations in a signal in the time domain. On the other hand, the OSAF is a feature that captures the changes in the dominant frequency band of the vibration signal. By combining these two functions, the SC is generated [11], obtained as follows:

$$SC = \frac{\sigma}{\bar{\sigma}} \, (1 + 2^E) \quad (9)$$

Where, $\bar{\sigma}$ is the mean of STD of all sections calculated in the stable stage, $\sigma/\bar{\sigma}$ is the ratio of instantaneous STD and the mean of the total standard deviation. E is a sign function:

$$E = sgn(\rho_1 - \bar{\rho}_1 - 1.96 \, \sigma_{\rho 1}) \quad (10)$$

In this Equation, $(\bar{\rho}_1)$ is also considered as the mean of OSAF calculation in the stable stage, $\sigma_{\rho 1}$ is the STD of ρ_1 and the scaling factor 1.96. This scaling factor represents the quantile of 97.5% confidence interval, a number commonly used for statistical calculation, from a normal distribution. If:

$\rho_1 < \bar{\rho}_1 + 1.96 \, \sigma_{\rho 1} \rightarrow E = -1$
and
$\rho_1 > \bar{\rho}_1 + 1.96 \, \sigma_{\rho 1} \rightarrow E = +1,$
then

SC can be described as follows:

$$SC = \begin{cases} 1.5\sigma/\bar{\sigma} \;\; , \; E = -1, \\ 2\sigma/\bar{\sigma} \;\; , \; E = 0, \\ 3\sigma/\bar{\sigma} \;\; , \; E = 1. \end{cases} \quad (11)$$

1.5. Online Chatter Recognition by SC

Establishing the threshold value of SC is a crucial step in online chatter recognition. The initial threshold value may be determined due to two essential conditions [11]:

$$\sigma > 1.875\bar{\sigma} \quad (12)$$

$$\rho_1 > \bar{\rho}_1 + 1.96\,\sigma_{\rho 1} \tag{13}$$

By applying both conditions simultaneously chatter vibrations occur and the threshold is equal to the following expression:

$$SC_{lim} = 1.875 \times 3 = 5.625 \tag{14}$$

The online chatter recognition by SC is:

$$SC \geq SC_{lim} \tag{15}$$

When the SC value reaches a predetermined threshold, an alarm is triggered using the above-mentioned "Eqs. (14) and (15)".

In order to achieve early chatter recognition and online control using the SC, the following procedure is typically followed: First, vibration signals are sampled in the stable stage of milling, and their parameters such as the A, B, and C are computed. The length of the sliding data section (N) and the calculation timers are then set by the user. In this paper, the length of data in sliding windows (N) is selected by trial and error to 300 samples. Then, $\bar{\sigma}, \bar{\rho}_1$ and $\sigma_{\rho 1}$ in each window are calculated. When the SC value reaches its threshold, chatter vibrations will be reported. Finally, by adjusting the milling parameters, chatter vibrations could be avoided.

3 THE TESTBED

To validate the SC algorithm in identifying chatter vibration, milling tests with different cutting conditions were conducted. For this process, a 4-teeth high speed steel end mill with a diameter of 10 mm and a length of 70 mm was employed. The experimental setup involved the utilization of two distinct flat strip workpieces with a width of 20, thickness of 10, and lengths of 50 mm and 70 mm, respectively, made of aluminum alloy 7075T6. As shown in "Fig. 1".

To acquire the signals, an STM32F103C8T6 data acquisition card was used with a sampling rate of 20 kHz. To receive signals in a more suitable range, the piezoelectric sensor with two resistors of 1 and 2 mega-ohms in the form of a series circuit was connected. The sensor signal is input to pin (A0) of the stm32 card. The following is a schematic of the circuit of this sensor ("Fig. 2"):

The acquired vibration signals were analyzed by MATLAB software. In all experiments, 10 mm of workpiece was clamped in vise. The testbed is depicted in "Fig. 3".

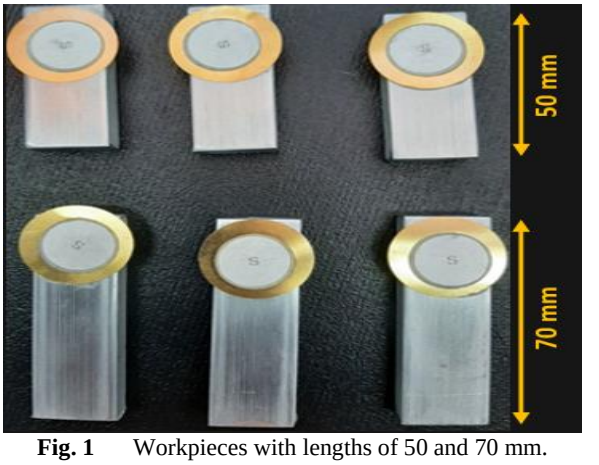

Fig. 1 Workpieces with lengths of 50 and 70 mm.

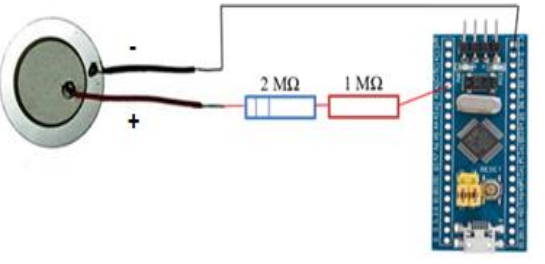

Fig. 2 Schematic of the circuit.

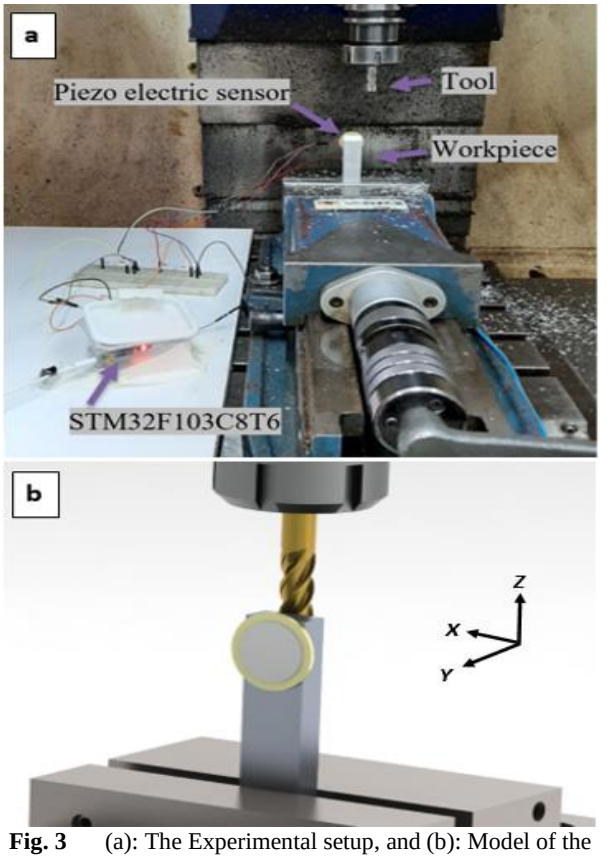

Fig. 3 (a): The Experimental setup, and (b): Model of the process.

4 EXPERIMENTAL TESTS

In this experiment, vibration signals under different cutting depths and constant spindle speeds and feeds were compared to investigate chatter during milling. These vibration signals are captured by using a piezoelectric sensor mounted on the workpiece along Y direction.

The workpieces should be fixed, so 10 mm of each piece were clamped in the milling lockdown vise. The SC for workpieces with a free length of 40 mm with a depth of 1, 4, and 6 mm and a workpiece of 60 mm with 0.5,1,4 and 6 mm, was investigated. For each section, 300 samples were selected as a computational part. To detect chatter vibrations, it is necessary to calculate the $\bar{\sigma}$, $\bar{\rho}_1$and $\sigma_{\rho 1}$ parameters of the vibration signals in the stable stage.

For the workpiece of 40 mm and at axial cutting depths of 1, 4, and 6 mm, the vibration signal was obtained. The following Figures illustrate the investigation of the chatter signal by the SC method (“Fig. 4”).

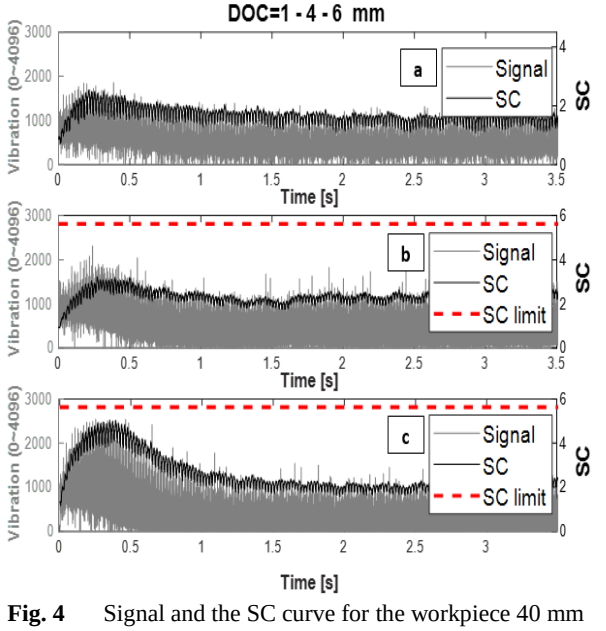

Fig. 4 Signal and the SC curve for the workpiece 40 mm and DOC: (a): 1, (b): 4 and (c): 6 mm.

During milling tests, the maximum SC values were found to be 2.5, 3.2, and 4.2 for cutting depths of 1 mm, 4 mm, and 6 mm, respectively. Notably, all three SC values were found to be less than the threshold value, indicating stable signals based on the SC method. However, increasing the free length of the workpiece resulted in higher levels of chatter vibration. To identify the most stable signal using the SC method for a 60 mm workpiece, two cutting depths of 0.5 mm and 1 mm were utilized, with the corresponding SC values presented in “Fig. 5”.

During the conducted milling tests, it was observed that the vibration signal remained stable at cutting depths of 0.5 mm and 1 mm.

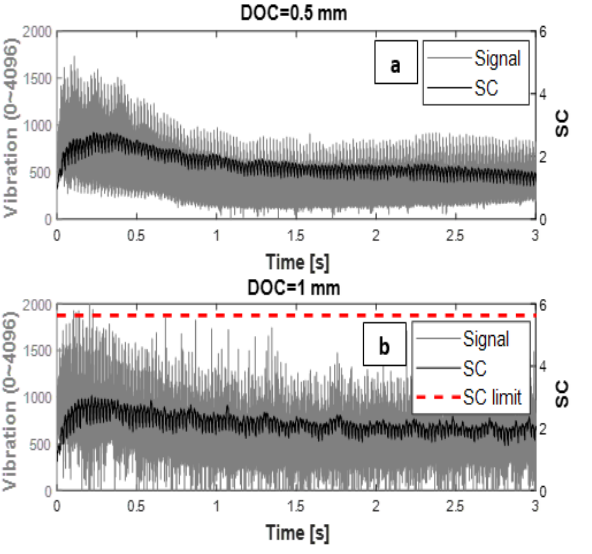

Fig. 5 The comparison of stability by SC method between DOC: (a): 0.5 and (b): 1 mm for the workpiece 40 mm.

Figure 6 presents the vibration signals for cutting depths of 0.5 mm, 4 mm, and 6 mm, as depicted using the STD and the OSAF diagrams in the time domain. Specifically, “Fig. 6 (a)” demonstrates a signal with a cutting depth of 0.5 that remains in a steady state, with minor fluctuations observed throughout the milling process, with different peak-to-peak ranging between 140 and 900 integer values.

During this process, the vibration signal exhibited significant fluctuations at cutting depths of 4 mm and 6 mm, as evidenced by the STD diagram. Specifically, at a cutting depth of 4 mm, the peak-to-peak fluctuations in “Fig. 6 (d)” remained less than 1008 integer values before 0.17 seconds. However, after this point, the difference increased to approximately 2920 integer values. Similarly, at a cutting depth of 6 mm in “Fig. 6 (g)”, the maximum difference was 2213 integer values before 0.1 seconds, with this difference significantly increasing to 3050 integer values. In the STD diagram, the fluctuations observed at a cutting depth of 0.5 mm in “Fig. 6 (b)” remained within a narrow range, with a peak-to-peak value of approximately 56.2 around a mean value of 200. However, “Figs. 6 (e) and (h)”, which demonstrate STD at cutting depths of 4 mm and 6 mm, the mean value increased sharply after 0.25 seconds and 0.15 seconds, respectively, reaching values of 764 and 954, respectively. Similarly, in the OSAF diagram, the amplitude widened at cutting depths of 4 mm and 6 mm, as shown in Figs 6 (f) and (i). They evidenced peaks in 0.14, and 0.06 seconds which reached 0.904 and 0.986 respectively. The signal, in turn, fluctuated around 0.4

and 0.65, respectively, at the end of the domain. Conversely, at the cutting depth of 0.5 mm, the OSAF diagram exhibited limited fluctuations around 0.94, within a range of approximately 0.0806, as depicted in "Fig. 6 (c)".

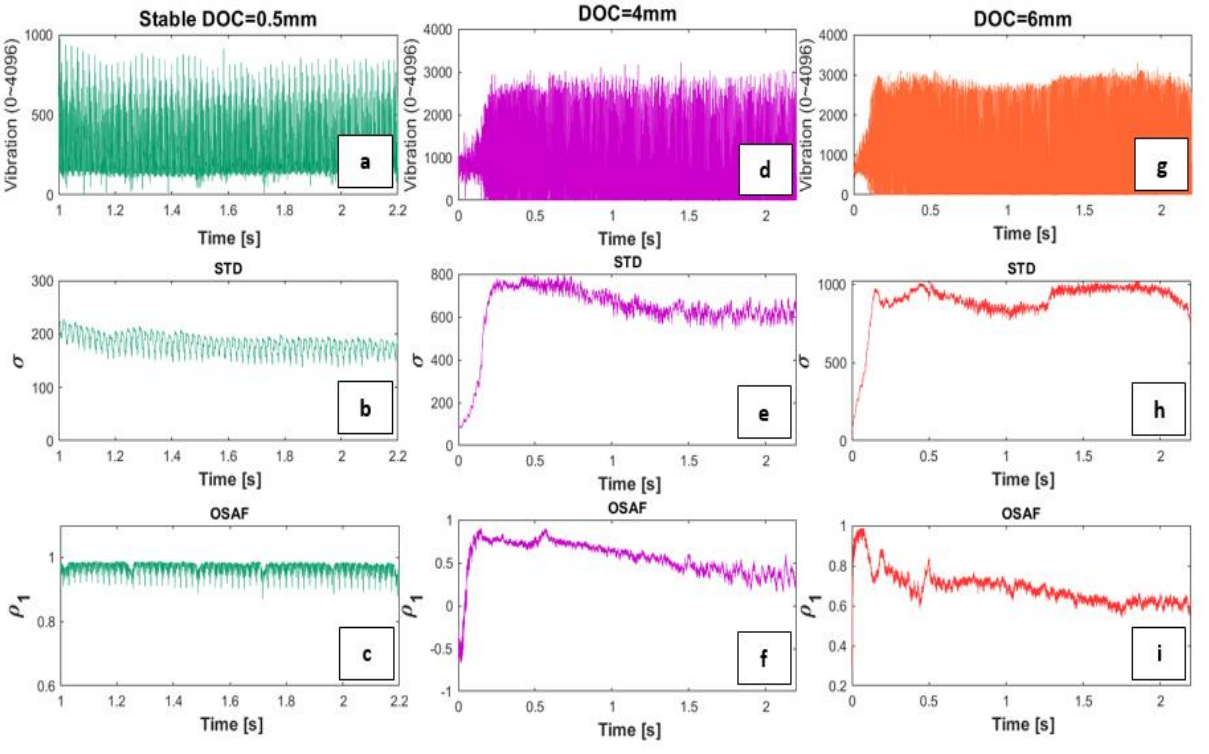

Fig. 6 The vibration time domain curve, STD, and OSAF curves. (Left) DOC 0.5 mm, (Middle) DOC 4 mm, (Right) DOC 6 mm.

So, this method is utilized for chatter detection at cutting depths of 4 mm and 6 mm. As depicted in "Figs 7 and 8", in these two depths of cut, chatter vibrations were observed. Specifically, a sharp increase in the SC was noted at the beginning of the 4 mm cutting depth, in "Fig. 7 (b)" with a maximum value of approximately 6.67 reached more than the SC threshold, being reached by 1.3 seconds.

The SC curve subsequently fluctuated around its threshold value for the remainder of the recorded time. Similarly, the SC curve for a cutting depth of 6 mm, as shown in "Fig. 8 (b)", exhibited an initial increase within the first 0.15 seconds, with the value exceeding the threshold range of SC_{lim} of 7.5 to 8.8.

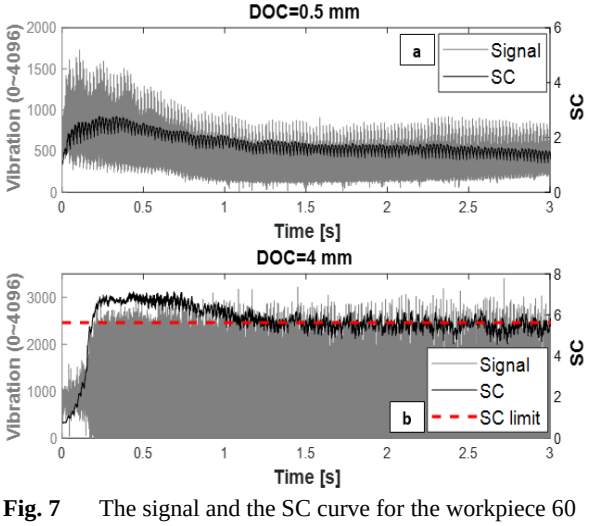

Fig. 7 The signal and the SC curve for the workpiece 60 mm and DOC: (a): 0.5 and (b): 4 mm.

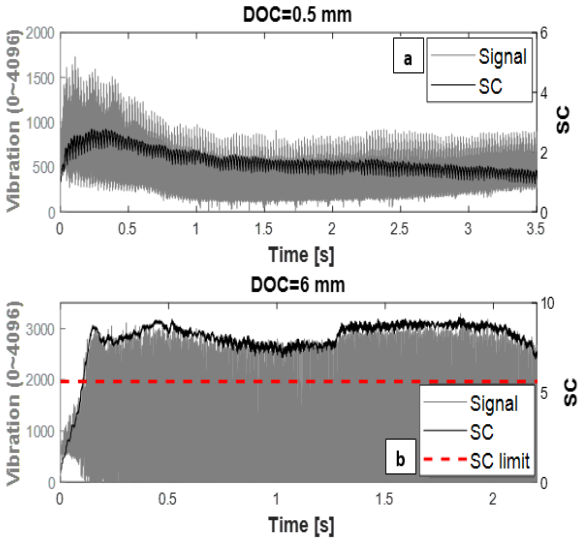

Fig. 8 Signal and the SC curve for the workpiece 60 mm and DOC: (a): 0.5 and (b): 6 mm.

Figure 9 showcases the Discrete Fourier Transforms (DFTs) of the vibration signals obtained from the free length workpiece measuring 40 mm in length and subjected to cutting depths of 1, 4, and 6 mm, along with the workpiece measuring 60 mm in length and subjected to cutting depths of 0.5, 1, 4, and 6 mm in "Fig. 10".

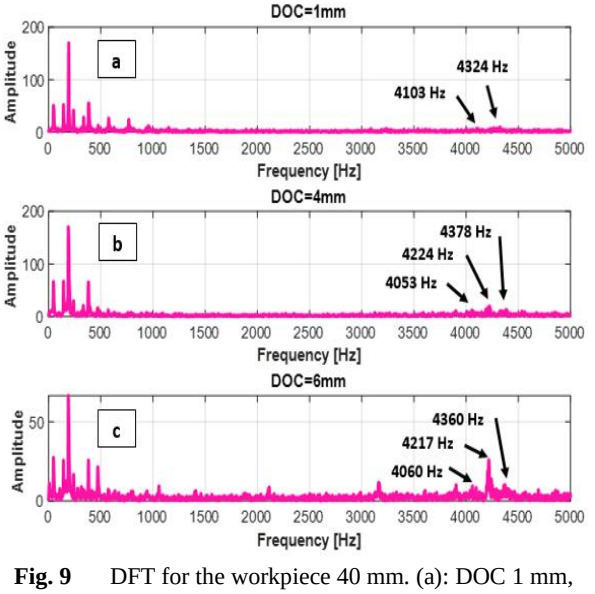

Fig. 9 DFT for the workpiece 40 mm. (a): DOC 1 mm, (b): DOC 4 mm, and (c): DOC 6 mm.

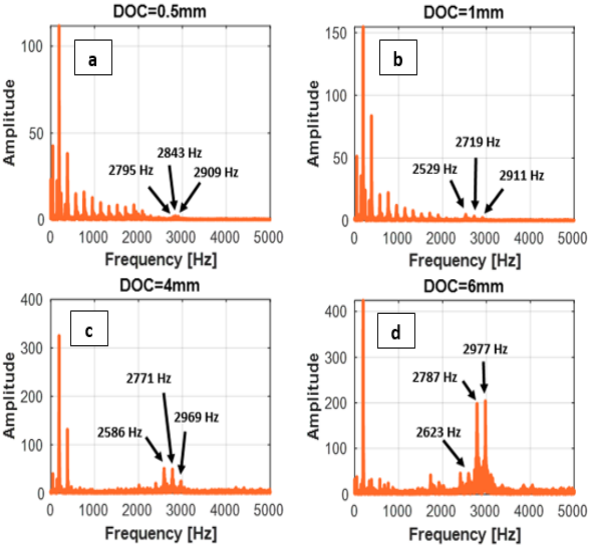

Fig. 10 DFT for the workpiece 60 mm. (a): DOC 0.5 mm, (b): DOC 1 mm, (c): DOC 4 mm, and (d): DOC 6 mm.

According to the findings presented in "Fig. 9", the free-length workpiece measuring 40 mm exhibits a dominant frequency of approximately 4200 Hz. Notably, this frequency had a significant increase in amplitude, rising from 9.8 at a cutting depth of 1 mm to 25.82 at a cutting depth of 6 mm. Similarly, the dominant frequency observed at a cutting depth of 6 mm in "Fig. 10", is approximately 2780 Hz, with the amplitude of the corresponding DFTs exhibiting an upward trend, increasing from 1.7 to 208 as the cutting depths vary from 0.5 to 6 respectively. These results indicate a decline in the dominant frequency of the signal with increasing free length of the workpiece, while the energy of the signal is shown to be directly proportional to the amount of axial depth of cut.

Figure 11 shows the milling surface of the workpiece with a free length of 60 mm and cutting depths of 0.5,1,4, and 6 mm. The machined surfaces depicted in "Figs. 11 (a) and (b)" exhibit a smooth texture with no visible chatter marks, thereby indicating a stable machining process with cutting depths of 0.5 and 1 mm. In contrast, the machined surfaces illustrated in "Figs. 11 (c) and (d)" demonstrate evidence of chatter vibration, evident from the visible chatter marks present at cutting depths of 4 and 6 mm, respectively. These experimental findings are consistent with the observations obtained from our developed online SC method.

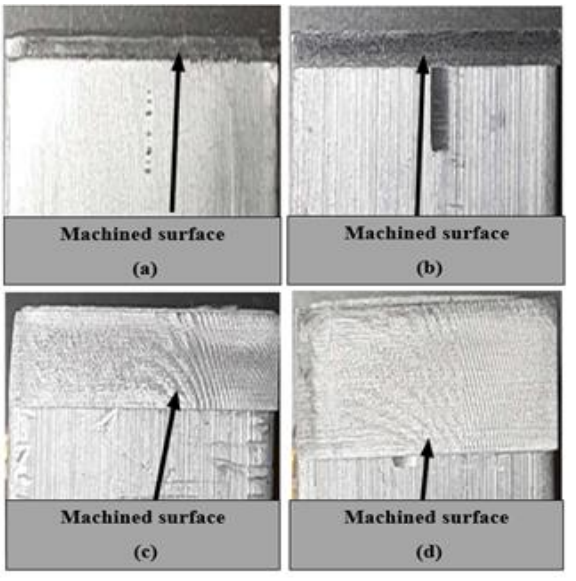

Fig. 11 Machined surface for the workpiece 60 mm. (a): DOC 0.5 mm, (b): DOC 1 mm, (c): DOC 4 mm, and (d): DOC 6 mm.

5 CONCLUSIONS

The primary objective of this study was to employ the SC method for the online detection of chatter vibrations during the milling process. This method involved the combination of the STD and the OSAF techniques. To validate the efficacy of the SC method, milling tests were designed and conducted, aimed at detecting chatter vibrations promptly. The SC method was proposed due to its robustness and high detection speed, making it a potent tool for the online recognition of chatter during the milling process. The use of the SC was essential for detecting chatter vibrations in the stable signal at different workpiece lengths. As the length of the workpiece increased, the cutting depth required for the stable signal to detect chatter decreased. Also, for analyzing the vibration signals, accelerometers were employed; however, in this paper, piezoelectric sensors were utilized. Owing to the lightweight of the sensor, there is no interference to the dynamic of the system at all. Additionally, the high bandwidth of these flexible sensors along with cost-effectiveness, make them an ideal choice for capturing vibration signals reliably and efficiently. The experimental results confirm the efficiency of the proposed algorithms in predicting the onset of chatter vibration using the developed hardware.

REFERENCES

[1] Tlusty, J., Manufacturing Processes and Equipment, 1st Edition, Prentice Hall, NJ, 2000, pp. 978-0201498653.

[2] Tsai, N. C., Chen, D. C., and Lee, R. M., Chatter Prevention for Milling Process by Acoustic Signal Feedback, The International Journal of Advanced Manufacturing Technology, Vol. 47, 2010, pp. 1013-1021, https://doi.org/10.1007/s00170-009-2245-y.

[3] Altintaş, Y., Budak, E., Analytical Prediction of Stability Lobes in Milling, CIRP annals, Vol. 44, No. 1, 1995, pp. 357-362, https://doi.org/10.1016/S0007-8506(07)62342-7.

[4] Altintaş, Y., Lee, P., A General Mechanics and Dynamics Model for Helical End Mills, CIRP Annals, Vol. 45, No. 1, 1996, pp. 59-64, https://doi.org/10.1016/S0007-8506(07)63017-0.

[5] Moradi, H., Movahhedy, M. R. and Vossoughi, G., Dynamics of Regenerative Chatter and Internal Resonance in Milling Process with Structural and Cutting Force Nonlinearities, Journal of Sound and Vibration, Vol. 331, No. 16, 2012, pp. 3844-3865, https://doi.org/10.1016/j.jsv.2012.03.003.

[6] Altintas, Y., Eynian, M., and Onozuka, H., Identification of Dynamic Cutting Force Coefficients and Chatter Stability with Process Damping, CIRP Annals, Vol. 57, No. 1, 2008, pp. 371-374, https://doi.org/10.1016/j.cirp.2008.03.048.

[7] Vela-Martínez, L., Jáuregui-Correa, J. C., and Álvarez-Ramírez, J., Characterization of Machining Chattering Dynamics: An R/S Scaling Analysis Approach, International Journal of Machine Tools and Manufacture, Vol. 49, No. 11, 2009, pp. 832-842, https://doi.org/10.1016/j.ijmachtools.2009.05.010

[8] Kuljanic, E., Sortino, M., and Totis, G., Multisensor Approaches for Chatter Detection in Milling, Journal of Sound and Vibration, Vol. 312, No. 4-5, 2008, pp. 672-693, https://doi.org/10.1016/j.jsv.2007.11.006.

[9] Kuljanic, E., Totis, G., and Sortino, M., Development of an Intelligent Multisensor Chatter Detection System in Milling, Mechanical Systems and Signal Processing, Vol. 23, No. 5, 2009, pp. 1704-1718, https://doi.org/10.1016/j.ymssp.2009.01.003.

[10] Liu, H., Chen, Q., Li, B., Mao, X., Mao, K., and Peng, F., On-Line Chatter Detection Using Servo Motor Current Signal in Turning, Science China Technological Sciences, Vol. 54, 2011, pp. 3119-3129, https://doi.org/10.1007/s11431-011-4595-6.

[11] Jia, G., Wu, B., Hu, Y., Xie, F., and Liu, A., A Synthetic Criterion for Early Recognition of Cutting Chatter, Science China Technological Sciences, Vol. 56, 2013, pp. 2870-2876, https://doi.org/10.1007/s11431-013-5360-9.

[12] Wiercigroch, M., Budak, E., Sources of Nonlinearities, Chatter Generation and Suppression in Metal Cutting, Philosophical Transactions of the Royal Society of London. Series A: Mathematical, Physical and Engineering Sciences, Vol. 359, No. 1781, 2001, pp. 663-693, https://doi.org/10.1098/rsta.2000.0750.

[13] Faassen, R. P. H., Van de Wouw, N., Oosterling, J. A. J., and Nijmeijer, H., Prediction of Regenerative Chatter by Modelling and Analysis of High-Speed

Milling, International Journal of Machine Tools and Manufacture, Vol. 43, No. 14, 2003, pp. 1437-1446, https://doi.org/10.1016/S0890-6955(03)00171-8.

[14] Yuan, L., A Study of Chatter in Robotic Machining and A Semi-Active Chatter Suppression Method Using Magnetorheological Elastomers (MREs), Master of Engineering Thesis, School of Mechanical, Material, Mechatronic and Biomedical Engineering, University of Wollongong, 2017.

[15] Tsai, N.C., Chen, D. C., and Lee, R. M., Chatter Prevention for Milling Process by Acoustic Signal Feedback, The International Journal of Advanced Manufacturing Technology, Vol. 47, 2010, pp. 1013-1021, https://doi.org/10.1007/s00170-009-2245-y.

[16] Zhang, C. L., Yue, X., Jiang, Y. T., and Zheng, W., A Hybrid Approach of Ann and Hmm for Cutting Chatter Monitoring, In Advanced Materials Research, 2010, Vol. 97, pp. 3225-3232, https://doi.org/10.4028/www.scientific.net/AMR.97-101.3225.

[17] Qu, S., Zhao, J., and Wang, T., Experimental Study and Machining Parameter Optimization in Milling Thin-Walled Plates Based on NSGA-II, The International Journal of Advanced Manufacturing Technology, Vol. 89, 2017, pp. 2399-2409, https://doi.org/10.1007/s00170-016-9265-1.

[18] Cao, H., Zhou, K., Chen, X., and Zhang, X., Early Chatter Detection in End Milling Based on Multi-Feature Fusion and 3σ Criterion, The International Journal of Advanced Manufacturing Technology, Vol. 92, 2017, pp. 4387-4397, https://doi.org/10.1007/s00170-017-0476-x.

[19] Chen, Y., Li, H., Jing, X., Hou, L., and Bu, X., Intelligent Chatter Detection Using Image Features and Support Vector Machine, The International Journal of Advanced Manufacturing Technology, Vol. 102, 2019, pp. 1433-1442, https://doi.org/10.1007/s00170-018-3190-4.

[20] Zhu, W., Zhuang, J., Guo, B., Teng, W., and Wu, F., An Optimized Convolutional Neural Network for Chatter Detection in The Milling of Thin-Walled Parts, The International Journal of Advanced Manufacturing Technology, Vol.106, 2020, pp. 3881-3895, https://doi.org/10.1007/s00170-019-04899-1.

[21] Wu, G., Li, G., Pan, W., Raja, I., Wang, X., and Ding, S., A State-of-Art Review on Chatter and Geometric Errors in Thin-Wall Machining Processes, Journal of Manufacturing Processes, Vol. 68, 2021, pp. 454-480, https://doi.org/10.1016/j.jmapro.2021.05.055.

[22] Hynynen, K. M., Ratava, J., Lindh, T., Rikkonen, M., Ryynänen, V., Lohtander, M., and Varis, J., Chatter Detection in Turning Processes Using Coherence of Acceleration and Audio Signals, Journal of Manufacturing Science and Engineering, Vol. 136, No. 4, 2014, https://doi.org/10.1115/1.4026948.

[23] Cao, H., Zhou, K., Chen, X., and Zhang, X., Early Chatter Detection in End Milling Based on Multi-Feature Fusion and 3σ Criterion, The International Journal of Advanced Manufacturing Technology, Vol. 92, 2017, pp. 4387-4397, https://doi.org/10.1007/s00170-017-0476-x.

Int. J. Advanced Design and Manufacturing Technology, 2024, Vol. 17, No. 3, pp. 11-23

DOI: ***ISSN: 2252-0406*** ***https://admt.isfahan.iau.ir***

Optimal Trajectory Planning of a Cable-Driven Parallel Robot by Direct Collocation Approaches

Milad Badrikouhi *, Mahdi Bamdad
Mechanical and Mechatronics Engineering School,
Shahrood University of Technology, Iran
E-mail: badrykoohimilad@gmail.com, bamdad@shahroodut.ac.ir
*Corresponding author

Received: 29 February 2024, Revised: 9 June 2024, Accepted: 8 September 2024

Abstract: Trajectory planning in cable-driven robots is more challenging than rigid-link ones. To maintain the robot control, the cable tensions must be positive during motion. This paper presents a direct collocation approach to solve the optimal trajectory planning based on the minimization of a robot's tension and tension-rate objective functions. Besides, during robot motion, the cables must be tensile. The configuration of a cable parallel robot composed of a 3-cable and a prismatic actuator neutralizes the moving platform's weight while improving tensionability. To generate smooth trajectories, the proposed method is compared with two standard approaches: GPOPS-II software package which uses Legendre-Gauss-Radu quadrature orthogonal collocation polynomials and direct collocation by using B-spline interpolation curves. Despite the efficiency of using B-spline functions in trajectory planning, numerical simulations demonstrate that the Hermite-Simpson direct collocation approach has a substantial benefit in the computation cost and accuracy for trajectory planning of a cable-driven parallel robot. Also, by choosing appropriate constraints and cost functions, the cable forces in the parallel robot can be well managed.

Keywords: B-Spline Interpolation Curves, Cable-Driven Parallel Robot, Direct Collocation, GPOPS-II, Trajectory Planning

Biographical notes: Milad Badrikouhi received his BSc from Guilan University, (2008), MSc from the Iran University of Science and Technology, (2012), and PhD from Shahrood University of Technology, (2022) all in Mechanical Engineering. His research interests include robot dynamics and kinematics, design, and optimal control of serial and parallel robots. **Mahdi Bamdad** received his BSc, MSc, and PhD in Mechanical Engineering in 2004, 2006, and 2010, respectively. He is currently an associate professor at the Shahrood University of Technology (Iran). His research interests are in the areas of mechanisms design and optimization of robotic systems.

Research paper

1 INTRODUCTION

In comparison with rigid links parallel robots, cable robots, have various profits such as low cost, low inertia, and friction, high payload-to-weight ratio, and large workspace toward serial robots[1-2]. Numerous Cable-Driven Parallel Robots (CDPRs) that have the benefit of this characteristic were constructed. The NIST RoboCrane, the SkyCam movable camera system, the flight simulator, and the virtual reality simulator are some of the CDPR applications [3-4]. However, the cables are flexible, and they can only bear the tension. Thus, *n*-DOF CDPR should have minimum *n*+1 cables to preserve the cable tension and manipulate the robot [5]. Similarly, for CDPRs that have *n*-DOF and *n* cables, instead of one more cable, another actuator can be used. As a remarkable example, a prismatic actuator was utilized to retain tension in all cables [6]. Also, a pneumatic muscle could play as the spinal cord rule in the design of biological cable robots to imitate the human neck [7]. In this work, the central spine is used to keep all cables in tension.

Optimal trajectory planning for the CDPR based on the definite cost functions provides a wide range of solutions [1], [8-11]. One of the best approaches to solving the problem of trajectory planning is optimal control theory. Two classes of direct and indirect approaches were considered for the optimal control problem (OCP) [12]. The indirect technique uses Pontryagin's Minimum Principle. As an example, the time-energy optimal control problem for a CDPR with bounds on joint torques was solved by Bamdad [13].

Besides the indirect method's advantages, it has a major defect due to falling in a local minimum. The boundary value problem is solved challenging since the results are sensitive to the unknown initial conditions [12]. Thus, in this paper, the direct approach is selected.

The direct method converts the trajectory planning to a parameter optimization problem. It uses discretizing the control and state variables. The key point about the direct method is that initial guesses have a low effect on the results. The integration process in the direct technique is essentially implicit. Compared to the indirect method, there is no need for analytical analysis and defining quasi-state variables. The key benefit of direct collocation is its directness. Also, the point and path constraints can be easily applied to the problem. Because of the discrete nature of the problem, there is no need for the shooting process, and high sensitivity to initial guess is removed. Thus, direct collocation is an influential nonlinear optimization technique that could be considered for systems with unstable dynamics and high nonlinearity. New research has established the potential of this approach [14-15]. In this article, an attempt is made to select a reliable direct method with minimum runtime to solve the trajectory optimization problem. On this basis, three direct methods of GPOPS-II, B-spline curves, and Hermit-Simpson collocation are compared with each other.

One of the direct approaches that convert the OCP to a discrete constrained minimization problem is the pseudo-spectral method. GPOPS-II uses the variable-order Gaussian quadrature methods as a standard software package [16]. In this technique, the state/control variables are approximated by interpolating polynomials, where the nodes are the roots of orthogonal polynomials. An example of GPOPS-II is minimum jerk trajectory tracking for redundant robots [17]. Also, Campbell and Kunkel attend to solve the unstructured tracking problem for a robot arm that has a flexible joint [18].

Also, trajectory planning has recently been mostly constructed by several interpolation functions such as polynomial, spline, and Bessel. Due to the main advantage of using spline curves on trajectory planning over polynomial and Bessel curves, several types of research based on B-spline curves could be found in prior literature. As an example, for a CDPR, a new pick-and-place solution by using the B-splines curves is presented in [19]. Also, acceleration and jerk optimization during trajectory have been found for parallel robots by B-spline curves in [20].

Mainly on the CDPR trajectory planning, because of the physical characteristics of cables, the special properties of cables must be considered. A minimum cable force limit is required to maintain all the cables in tension. Also, the maximum tension that cables can bear safely must be declared. In this regard, a model predictive controller is presented by Santos et al. which handles the tension distribution of the cables [21]. Also in [22], by optimal force allocation control, differentiable continuous tensions are guaranteed in over-constrained CDPR. In this work, the tension management of the cables is considered. Thus, the main contribution of this paper is:

1- A Hermite-Simpson fast-direct collocation method adapting to the dynamic model of a CDPR is introduced and employed to obtain the optimal trajectory in an off-line mode. For this purpose, also Gaussian quadrature by GPOPS-II and B-spline interpolation function which are well-known algorithms are selected to compare the numerical results and show the superiority of the Hermit-Simpson method.

2- Two practical cost functions are introduced regarding the management of cable tensions. The first scenario is the minimum tension trajectory planning and the second is the minimum tension rate. The problem constraints consist of tension limits so that the cables are always under control.

3- A hybrid CDPR consisting of a spine that exerts the normal force on the end-effector is offered. The normal force maintains all the cables tightened.

The remainder of this work is arranged as follows: Sections 2, 3, and 4 explain three well-known approaches of direct collocation scheme, Hermite-Simpson direct collocation, GPOPS-II, and using B-spline curves. Section 5 presents the CDPR, and the kinematics and dynamics are formulated. Section 6 signifies the problem statement. The dynamic Equation and the objective functions are considered. Minimum tension and minimum tension rate are selected as cost functions. The discretized dynamic Equation of motion is stated as the equality constraints and, the boundary conditions are expressed. Additionally, the cable forces must be maintained tensile during CDPR motion. In section 7, the dynamic model is verified by the ADAMS model. Section 8 discusses the simulation results of trajectory planning by three techniques, and ultimately, in section 9, the paper's conclusion is presented.

2 HERMITE-SIMPSON DIRECT COLLOCATION

The goal of CDPR trajectory planning is to generate the optimum controls according to the given objective function along with the physical limits such as maintaining positive cable tension. Thus, in a direct method, the CDPR state and controls are discretized. Commonly, the dynamic modeling of the CDPR is $\dot{\mathbf{x}}(t) = \mathbf{f}(\mathbf{x}(t), \mathbf{u}(t))$, where $\mathbf{x} \in \mathbf{R}^n$ and $\mathbf{u} \in \mathbf{R}^m$ designate the vector of states and controls. The problem is to find $\mathbf{u}(t)$, $\forall t \in [0, T]$, such that a given objective function J is minimized:

$$\begin{aligned} \underset{\mathbf{x}(t),\mathbf{u}(t)}{\text{minimize}} \quad & J(\mathbf{x}(t),\mathbf{u}(t)) = \int_0^T \phi(\mathbf{x}(t),\mathbf{u}(t),t) \\ \text{subject to} \quad & \dot{\mathbf{x}}(t) = \mathbf{f}(\mathbf{x}(t),\mathbf{u}(t)) \\ & \mathbf{h}(\mathbf{x}(t),\mathbf{u}(t)) = 0 \\ & \mathbf{g}(\mathbf{x}(t),\mathbf{u}(t)) \le 0 \\ & 0 \le t \le T \end{aligned} \tag{1}$$

Φ is the objective function, and **h** and **g** are formulated as the list of constraints [12]. This continuous system is converted to a discretized system with a finite number of variables by direct collocation. All approaches in direct methods divide the phase duration (time) into N -1 intervals, $0=t_1<t_2<\ldots<t_N=T$ where the points are denoted as a node. We use $\mathbf{x}_k = \mathbf{x}(t_k)$. Let us indicate the control by $\mathbf{u}_k = \mathbf{u}(t_k)$. Thus, a discrete-time dynamic is $\mathbf{x}(k+1) = f(\mathbf{x}(k), \mathbf{u}(k), k)$. We can collocate dynamic modeling via different approaches such as trapezoidal, Hermite-Simpson, etc. However, because of the adequate numerical accuracy, the Hermite-Simpson is applied for discretizing.

$$\begin{aligned} \underset{\mathbf{x}(k),\mathbf{u}(k)}{\text{minimize}} \quad & J(\mathbf{x}_k,\mathbf{u}_k) = \sum_{k=1}^{N} \phi(\mathbf{x}_k,\mathbf{u}_k) \qquad (k = 1,2,...,N) \\ \text{subject to} \quad & \mathbf{x}_{k+1} - \mathbf{x}_k = \frac{h}{6}(\mathbf{f}_k + 4\bar{\mathbf{f}}_{k+1} + \mathbf{f}_{k+1}) \quad (k = 1,2,...,N-1) \\ & \bar{\mathbf{x}}_{k+1} = \frac{1}{2}(\mathbf{x}_{k+1} + \mathbf{x}_k) + \frac{h}{8}(\mathbf{f}_k - \mathbf{f}_{k+1}) \\ & \bar{\mathbf{f}}_{k+1} = \mathbf{f}(\bar{\mathbf{x}}_{k+1}, \bar{\mathbf{u}}_{k+1}) \\ & \mathbf{h}(\mathbf{x}_k,\mathbf{u}_k) = 0 \\ & \mathbf{g}(\mathbf{x}_k,\mathbf{u}_k) \le 0 \end{aligned} \tag{2}$$

Where, $h = (t_N - t_1) / (N-1)$ is the time between two nodes. Now, the optimal control problem converts to the optimization of an NLP problem. The optimization problem is defined in such a way that the state and control values, $\mathbf{x}_k$ and $\mathbf{u}_k$ are selected at each node in such a way that the dynamic Equations, boundary conditions, and all constraints are satisfied. In addition, the control values should be minimized according to the objective function simultaneously. The analytic Sequential quadratic programming, SQP solver is selected to solve this problem because it is faster and more precise rather than other algorithms, especially the evolutionary algorithm. In the optimization problem, selecting a reasonable initial guess can accelerate convergence and minimize the solution time. First, the optimization variables must be limited based on the physical nature of the joint variables and actuator forces. If it is considered $\mathbf{y}_k=(\mathbf{x}_k,\mathbf{u}_k)$, it is supposed a lower bond $\mathbf{l_b}$ and upper bound $\mathbf{u_b}$ for each state and control variable $\mathbf{y}_k$ as $\mathbf{l_b}<\mathbf{y}_k<\mathbf{u_b}$. In this paper, the linear initial guess between the boundary values of each state and control variable is considered in "Eq. (3)".

$$\mathbf{y}_k^0 = \mathbf{y}_1 + \frac{k-1}{N-1}(\mathbf{y}_N - \mathbf{y}_1) \qquad (k = 1,2,...,N) \tag{3}$$

Which $\mathbf{y}_k^0$ is the initial guess. Also, $\mathbf{y}_1$ and $\mathbf{y}_N$ are initial and final values.

3 GPOPS-II

GPOPS-II is a MATLAB package offered for solving OCPs for nonlinear dynamics. GPOPS-II utilizes a direct collocation technique by the pseudospectral functions [16]. The continuous-time OCP is approximated using a new class of variable-order Legendre-Gauss-Radau quadrature orthogonal collocation polynomials resulting in an NLP. As stated, GPOPS-II approximates both states and controls that translate the OCP into an NLP for each (K=1, 2, …, N-1) interval. The critical points of a solution by GPOPS-II are [23]:

- The algebraic constraints can be used.
- GPOPS-II can use automatic mesh refinement.
- To develop the required gradients, hessian and Jacobian, automatic differentiation is accessible.

4 B-SPLINE CURVES

B-spline curves are an interconnected set of Bezier curves in the following general form [12]:

$$x(t)=\sum_{i=1}^{n} B_{i,k}(t)C_i \quad t_1 \le t \le t_N \tag{4}$$

The Equations of B-spline curves consist of two parts, basic functions $B_{i,k,}$ and control points C_i. To calculate $B_{i,k}$, one must first determine the number of Bezier curves and their degrees. Then, the time should be divided by the number of curves. Each point is called a node thus the time node vector is formed $\mathbf{t}$= [t_1, t_2, …, t_N]. A value of time may be repetitive numerous times in a node vector, named the number of repetitions. The difference between the order of the curve, k_i, and the number of repetitions m_i determines the degree of smoothness s_i.

$$s_i = k_i - m_i \tag{5}$$

s_i designates the level of continuity in the node, which is equal to the s_i -1 order of derivation. By these assumptions, the basic functions can be calculated using the following relations:

$$B_{i,1}(t)=\begin{cases}1 \text{ if } t_i \le t \le t_{i+1}\\ 0 \text{ otherwise}\end{cases} \tag{6}$$

$$B_{i,k}(t)=\frac{t-t_i}{t_{i+k+1}-t_i}B_{i,k-1}(t)+\frac{t_{i+k}-t}{t_{i+k}-t_{i+1}}B_{i+1,k-1}(t)$$

The control points organize the curve and produce a continuous concept. B-spline curves behave quite locally. By changing one of the control points, only the shape of the curve in the vicinity of the control point changes and the rest of the B-spline curve remains unchanged.

5 CDPR MODELING

A prismatic central linkage is used in this CDPR to supply structural stability. This central spine with wire actuation is utilized to obtain various important benefits while the advantages of a CDPR are needed. In "Fig. 1", the CDPR CAD model is illustrated. This platform has 3-DOF: pitch, roll, and heave. In this mechanism, the cylinder is fixed at point *O* to the base and attached to the EE at point P_m by a 2-DOF Cardan joint. Universal joint limits the platform's rotation about the Z-axis as a single rotational DOF. Two other movements, moving forward/backward and moving left/right are also prevented.

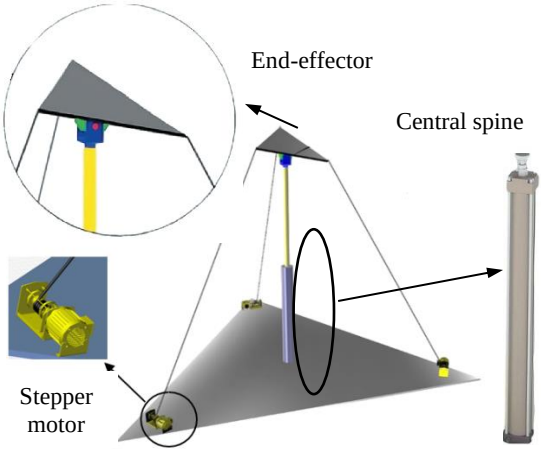

Fig. 2 CDPR CAD model.

A prismatic actuator is used to eliminate the gravitational effects for any CDPR configuration. Thus, it makes the potential energy constant. The use of a prismatic joint has some advantages. The prismatic actuator supports the end-effector's weight while improving the tensionability condition. Positive tension must be guaranteed during CDPR motion. The cylinder moves the moving platform up and down, and the cables are designed to direct the EE. Since the pneumatic cylinder tolerates the EE weight, to guide the EE, using powerful motors is not necessary.

For kinematic analysis, the reference frame [A: XYZ] is fixed at point *O* to the base, and the moving frame [B: xyz] is attached to the EE at point $P_{m,}$ the EE center of mass. The EE coordinate $\mathbf{x}$ is expressed in [z, α, β] ^{T}. z denotes the height of the P_m, α denotes the EE pitch angle around the X-axis, and β denotes the EE roll angle around the Y-axis. In inverse kinematics, these coordinates are considered. The $\mathbf{q}$ = [l_1, l_2, l_3, d] ^{T} is the joint coordinate. l_i is the cable length, and d is the cylinder position. Since the pneumatic cylinder is fixed to the base, $z = d+d_0$, in which the fixed length of the pneumatic cylinder d_0 is considered 0.5m. The angle between the right-hand side of the X-axis and OSi is θ_i (i=1,2,3). The schematic diagram of the mechanism is introduced in "Fig. 2". To obtain the cable length, we form the following Equations:

$$\mathbf{OS}_i + \mathbf{S}_i\mathbf{P}_i = \mathbf{OP}_i \longrightarrow l_i = \left\|\mathbf{S}_i\mathbf{P}_i\right\| = \left\|\mathbf{OP}_i - \mathbf{OS}_i\right\| \tag{7}$$

$\mathbf{OS}_i$ is a constant vector. Also, $\mathbf{OP}_i = \mathbf{z} + \mathbf{P}_m\mathbf{P}_i$, in which $\mathbf{z}$ is known. For $\mathbf{P}_m\mathbf{P}_i$, we have $\mathbf{P}_m\mathbf{P}_i = \mathbf{R_m{}^o P_i}$. $\mathbf{R_m{}^o}$

$=\mathbf{R}_{PR}=\mathbf{R}_y(\beta)\mathbf{R}_x(\alpha)$ is the rotation matrix of the EE. Also, $\mathbf{P}_i$ is the primary position of the vector $\mathbf{P}_m\mathbf{P}_i$ relative to the frame [B]. Consequently, the inverse kinematic Equation is:

$$z = d + d_0,\ \ l_i = \left\| \mathbf{z} + \mathbf{R}_y(\beta)\mathbf{R}_x(\alpha)\mathbf{P}_i - \mathbf{OS}_i \right\| \tag{8}$$

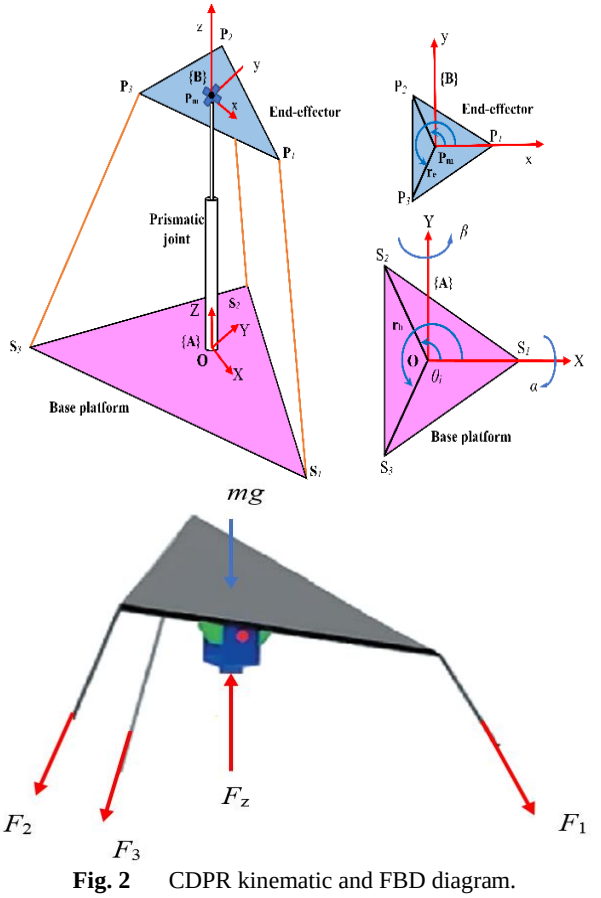

Fig. 2 CDPR kinematic and FBD diagram.

By velocity loop closure, the Jacobian is calculated. **I**, **J**, **K** is the unit vector of a frame [A], and **i**, **j**, **k** is the unit vector of [B]. The relationship between the joint velocities and EE velocity is explained in the following Equation:

$$\dot{\mathbf{q}} = \mathbf{J}_x\dot{\mathbf{x}} \tag{9}$$

In which $\mathbf{J}_x$ is the Jacobian, $\dot{\mathbf{q}}$ is the velocity vector of the joints, and $\dot{\mathbf{x}}$ is the EE velocity. First, we notice the next Equation, which is established in every closure loop of the parallel platform.

$$\mathbf{OP}_m + \mathbf{P}_m\mathbf{P}_i = \mathbf{OS}_i + \mathbf{S}_i\mathbf{P}_i \tag{10}$$

In the next step, we differentiate from each term of Eq. (10). First, by considering prismatic joint, $d\mathbf{OP}_m/dt = \dot{z}\mathbf{K}$ with pitch–roll rotation, we have:

$$\left(\frac{d\,\mathbf{P}_m\mathbf{P}_i}{dt}\right)_{\mathbf{fix}} = \boldsymbol{\Omega}\times\mathbf{P}_m\mathbf{P}_i,\ \boldsymbol{\Omega} = \dot{\alpha}\mathbf{I} + \dot{\beta}\mathbf{J} \tag{11}$$

Also, $\mathbf{OS}_i$ is a constant vector. As a result, $d\mathbf{OS}_i/dt=0$. Also, l_i direction through a unit vector $\mathbf{s}_i$ is calculated as follows:

$$\mathbf{s}_i = \frac{\mathbf{S}_i\mathbf{P}_i}{l_i} \longrightarrow \mathbf{S}_i\mathbf{P}_i = l_i\mathbf{s}_i \tag{12}$$

The angular velocity vector of the cables, Ω_{li} is perpendicular to $\mathbf{s}_i$, and cables do not rotate around themselves, as a result:

$$\frac{d\,(l_i\mathbf{s}_i)}{dt} = \dot{l}_i\mathbf{s}_i + \boldsymbol{\Omega}_{l_i}\times l_i\mathbf{s}_i \tag{10}$$

Therefore, the final Equation for velocity loop closure is rewritten as:

$$\dot{z}\,\mathbf{K} + (\dot{\alpha}\mathbf{I} + \dot{\beta}\mathbf{J})\times\mathbf{P}_m\mathbf{P}_i = \dot{l}_i\mathbf{s}_i + \boldsymbol{\Omega}_{l_i}\times l_i\mathbf{s}_i \tag{11}$$

For calculating $\mathbf{J}_x$, the cross product of the vector $\mathbf{s}_i$ satisfies the following Equation.

$$\dot{z}\,\mathbf{K}.\mathbf{s}_i + ((\dot{\alpha}\mathbf{I} + \dot{\beta}\mathbf{J})\times\mathbf{P}_m\mathbf{P}_i).\mathbf{s}_i = \dot{l}_i\mathbf{s}_i.\mathbf{s}_i + (\boldsymbol{\Omega}_{l_i}\times l_i\mathbf{s}_i).\mathbf{s}_i \tag{12}$$

Considering $\mathbf{P}_m\mathbf{P}_i = \mathbf{E}_i$, "Eq. (12)" simplifies to:

$$\dot{z}\,\mathbf{K}.\mathbf{s}_i + \dot{\alpha}(\mathbf{I}\times\mathbf{E}_i).\mathbf{s}_i + \dot{\beta}(\mathbf{J}\times\mathbf{E}_i).\mathbf{s}_i = \dot{l}_i \tag{13}$$

Rewriting "Eq. (13)" results in:

$$[\mathbf{K}.\mathbf{s}_i \,|\, (\mathbf{I}\times\mathbf{E}_i).\mathbf{s}_i \,|\, (\mathbf{J}\times\mathbf{E}_i).\mathbf{s}_i\,][\dot{z}\ \ \dot{\alpha}\ \ \dot{\beta}]^T = \dot{l}_i \tag{14}$$

From "Eq. (5)", $\dot{z} = \dot{d}$, using "Eq. (14)" for i = 1, 2, 3, $\mathbf{J}_x$ is derived as:

$$\mathbf{J}_x = \begin{bmatrix} \mathbf{K}.\mathbf{s}_1 & (\mathbf{I}\times\mathbf{E}_1).\mathbf{s}_1 & (\mathbf{J}\times\mathbf{E}_1).\mathbf{s}_1 \\ \mathbf{K}.\mathbf{s}_2 & (\mathbf{I}\times\mathbf{E}_2).\mathbf{s}_2 & (\mathbf{J}\times\mathbf{E}_2).\mathbf{s}_2 \\ \mathbf{K}.\mathbf{s}_3 & (\mathbf{I}\times\mathbf{E}_3).\mathbf{s}_3 & (\mathbf{J}\times\mathbf{E}_3).\mathbf{s}_3 \\ 1 & 0 & 0 \end{bmatrix} \tag{15}$$

The manipulator dynamic Equation of motion can be obtained from the Newton-Euler formulation. In this case, the cable mass and friction are neglected. Let $\mathbf{W}_{env} = [F_z, T_x, T_y]^T$ be the wrench applied on the EE center by the environment and $\boldsymbol{\tau}=[T_1, T_2, T_3, F_z]^T$ is the actuator force where T_i is the tensions and F_{zc} is the cylinder force. The EE position/orientation relative to the world

coordinate systems is denoted by three variables in $\mathbf{x}=[z, \alpha, \beta]^T$. After CDPR Jacobian $\mathbf{J_x}$ calculated from "Eq. (11)", nonlinear differential Equations of motion for the CDPR is rewritten as:

$$\mathbf{D(x)}\ddot{\mathbf{x}}+\mathbf{C(x,\dot{x})}+\mathbf{G(x)}=\mathbf{J}_x{}^T\boldsymbol{\tau} \tag{16}$$

In which $\mathbf{D(x)}$ signifies the CDPR mass matrix, $\mathbf{C(x,\dot{x})}$ signifies the Coriolis and centrifugal matrix, and $\mathbf{G(x)}$ signifies the gravity effect, all will be presented in Appendix A. The CDPR Jacobian $\mathbf{J_x}$ is calculated from "Eq. (15)". As a result, the state space can be developed as below:

$$\begin{cases} x_1=z \\ x_2=\dot{z} \\ x_3=\alpha \\ x_4=\dot{\alpha} \\ x_5=\beta \\ x_6=\dot{\beta} \end{cases} \longrightarrow \begin{cases} \dot{x}_1=x_2 \\ \dot{x}_2=\left(\mathbf{D}^{-1}(\mathbf{x})\left(\mathbf{J}_x{}^T\boldsymbol{\tau}-\mathbf{G(x)}-\mathbf{C(x,\dot{x})}\right)\right)_1=A_1 \\ \dot{x}_3=x_4 \\ \dot{x}_4=\left(\mathbf{D}^{-1}(\mathbf{x})\left(\mathbf{J}_x{}^T\boldsymbol{\tau}-\mathbf{G(x)}-\mathbf{C(x,\dot{x})}\right)\right)_2=A_2 \\ \dot{x}_5=x_6 \\ \dot{x}_6=\left(\mathbf{D}^{-1}(\mathbf{x})\left(\mathbf{J}_x{}^T\boldsymbol{\tau}-\mathbf{G(x)}-\mathbf{C(x,\dot{x})}\right)\right)_3=A_3 \end{cases} \tag{17}$$

6 PROBLEM STATEMENT

Due to trajectory planning, the direct collocation method should be adapted with CDPR modeling. First, from the dynamics, the states are the joint position and velocity, and the controls are the actuator. Thus, the optimization variables are:

$$\mathbf{y}_k=[z_k,\dot{z}_k,\alpha_k,\dot{\alpha}_k,\beta_k,\dot{\beta}_k,F_{1_k},F_{2_k},F_{3_k},F_{z_k}] \tag{18}$$

In which k = 1, 2, …, N. The NLP variables that should be optimized based on the cost function are $\mathbf{y}=(\mathbf{y}_1, \mathbf{y}_2, \ldots, \mathbf{y}_N)^T$. The trajectory planning problem is to detect $\mathbf{y}$ in all nodes considering boundary conditions and constraints. This problem is prescribed with cable force and force rate in the objective functions. The inequality constraints include positive force in the cables. "Table 1" explains the objective function. From "Eq. (17)" and using "Eq. (3)", the dynamic constraint is established as the equality constraint: Minimize J

Table 1 Cost functions definition

Cost functions	Continuous form
Minimum– tension	$J=\frac{1}{2}\int_{t_1}^{t_N}(T_1{}^2+T_2{}^2+T_3{}^2)\mathrm{d}t$
Minimum – tension–rate	$J=\frac{1}{2}\int_{t_1}^{t_N}\left[\left(\frac{dT_1}{dt}\right)^2+\left(\frac{dT_2}{dt}\right)^2+\left(\frac{dT_3}{dt}\right)^2\right]\mathrm{d}t$

Subject to:

$$\begin{cases} x_{1_{k+1}}-x_{1_k}-\frac{h}{6}(x_{2_k}+4\bar{x}_{2_{k+1}}+x_{2_{k+1}})=0 \\ x_{2_{k+1}}-x_{2_k}-\frac{h}{6}(A_{1_k}+4\bar{A}_{1_{k+1}}+A_{1_{k+1}})=0 \\ x_{3_{k+1}}-x_{3_k}-\frac{h}{6}(x_{4_k}+4\bar{x}_{4_{k+1}}+x_{4_{k+1}})=0 \\ x_{4_{k+1}}-x_{4_k}-\frac{h}{6}(A_{2_k}+4\bar{A}_{2_{k+1}}+A_{2_{k+1}})=0 \\ x_{5_{k+1}}-x_{5_k}-\frac{h}{6}(x_{6_k}+4\bar{x}_{6_{k+1}}+x_{6_{k+1}})=0 \\ x_{6_{k+1}}-x_{6_k}-\frac{h}{6}(A_{3_k}+4\bar{A}_{3_{k+1}}+A_{3_{k+1}})=0 \end{cases} \quad (k=1,2,\ldots,N-1) \tag{19}$$

The boundary conditions are the second list of constraints.

$$\begin{aligned} &z_1=0.5\,\mathrm{m}, \quad \dot{z}_1=0\ \mathrm{m/s}, \quad z_N=1\mathrm{m}, \quad \dot{z}_N=0\ \mathrm{m/s} \\ &\alpha_1=0\,\mathrm{rad}, \quad \dot{\alpha}_1=0\ \mathrm{rad/s}, \quad \alpha_N=0.35\,\mathrm{rad}, \quad \dot{\alpha}_N=0\ \mathrm{rad/s} \\ &\beta_1=0\,\mathrm{rad}, \quad \dot{\beta}_1=0\ \mathrm{rad/s}, \quad \beta_N=0.2\,\mathrm{rad}, \quad \dot{\beta}_N=0\ \mathrm{rad/s} \end{aligned} \tag{20}$$

For cable constraints, it must be considered positive tension otherwise, the CDPR performance will be troubled.

$$F_{i_k}\geq F_{allow} \quad \begin{cases} (i=1,2,3) \\ (\mathrm{k}=1,2,\ldots,N) \end{cases} \tag{21}$$

At time t_k, $F_{ik}= F_i(t_k)$ represents the tension (i=1,2,3). F_{allow} is the minimum cable force and is 10N. The CDPR parameters are denoted in "Table 2". SQP by the suggested procedure in "Fig. 3" solves this trajectory planning problem.

Table 2 The cable robot parameters

Parameters	Value	Unit
Angle	θ_1 =0 θ_2 =120 θ_3 =240	degree
Base radius	r_b =0.8	m
EE radius	r_e =0.2	m
EE mass	m=100	Kg
EE moment of inertia	I=1	Kg.m^2
Initial time	t_1 =0	s
Final time	t_N =2	s

Algorithm Direct collocation trajectory planning of a CDPR

Input:
1: Get the parameters: θ_i, r_b, r_e, m, I, t_1, t_N.
2: Define lower bond **lb** and upper bond **ub**.
3: Define the boundary values by Eq. (20).
4: Define the linear initial guess matrix $\mathbf{y_k^0}$ ("Eq. (3)").
5: Consider the NLP variables $\mathbf{y}=\mathbf{y_k^0}$.
Constraint function.
6: **For** k=1 to N-1 **do**
7: Consider dynamics constraints ("Eq. (19)").
8: **End for**
9: Set the boundary conditions ("Eq. (20)") and positive tensions ("Eq. (21)").
Objective function.
10: **For** k=1 to N-1 **do**
11: Define the ***objective function*** ("Table 1").
12: **End for**
Direct collocation method:
13: **While** the optimality condition is satisfied **do**
14: Call the ***Objective function*** and ***Constraint function***.
15: Compute new trajectory **y** by NLP iterative search algorithm.
16: **End while**
Output:
17: Report optimal trajectory $\mathbf{y_s}=\mathbf{y}$.

Fig. 3 The proposed algorithm.

7 DYNAMIC MODEL VERIFICATION

To verify the dynamic modeling, a model is implemented through ADAMS software. As shown in "Fig. 4", this model includes complete details of the CDPR. To verify, nonlinear actuator controls are considered.

$$\begin{cases} T_1 = 2\sin(\frac{\pi t}{2}), \text{unit}:\text{N} \\ T_2 = 2-2\sin(\frac{\pi t}{2}), \text{unit}:\text{N} \\ T_3 = 2\sin(\frac{\pi t}{2}), \text{unit}:\text{N} \\ F_z = 980.6+10\sin(\frac{\pi t}{2}), \text{unit}:\text{N} \end{cases} \quad (22)$$

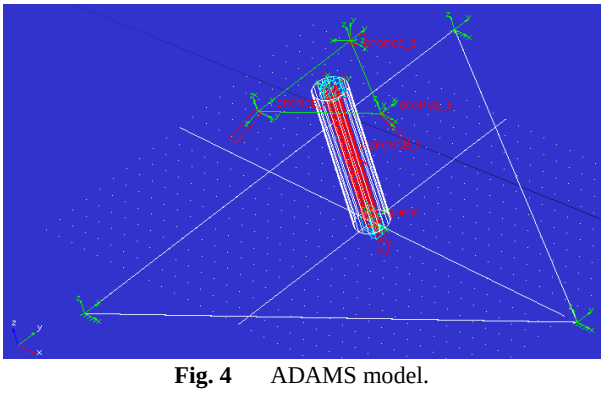

Fig. 4 ADAMS model.

The simulation results of both methods are quite similar. The model simplification causes small inaccuracies between the MATLAB and ADAMS models. It is considered the ideal universal joint in MATLAB. Thus, the EE gravitational force has no torque around the center of the U-joint, but in ADAMS there is. Also, in the MATLAB model, it is considered that the moving platform has no thickness. Some minor errors may be caused by the numerical errors of the ordinary differential Equation solver in ADAMS, which are reasonable in a sense. Therefore, the accuracy of the dynamic model is verified ("Fig. 5").

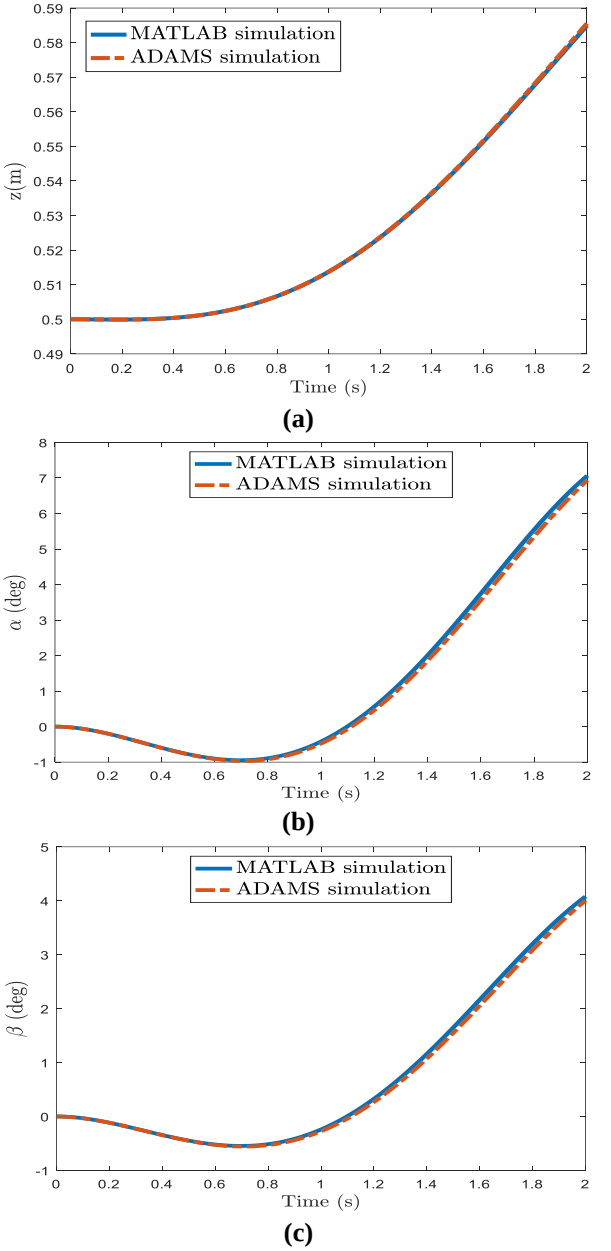

Fig. 5 Results of the MATLAB and ADAMS simulation: (a): EE center of mass z position, (b): roll angle, and (c): pitch angle.

8 TRAJECTORY PLANNING WITH HERMITE-SIMPSON, GPOPS-II, AND B-SPLINE CURVES METHODS

For simulation, the computer specification is Windows 7 Pro, Intel (R) Core (TM) i5 CPU M-480 @ 2.67GHz and 4GB RAM. MATLAB has been used for simulation. We can compare GPOPS-II, Hermite-Simpson, and B-spline methods corresponding to the minimization of the cost function. Solving the trajectory planning problem by minimizing tension and tension rate is summarized in "Table 3". The runtime is divided into ten nodes.

Also, three stopping criteria for SQP solver are defined. Generally, the stopping criteria are thresholds that, if crossed, stop the iterations. *TolX* is the minimum size of a step. If the solver takes a step tinier than *TolX*, the iterations finish. *TolFun* is a minimum change in the cost function value during a step. The process will be completed when $|J(\mathbf{x}_k) - J(\mathbf{x}_{k+1})| < TolFun$. At last, *MaxIter* is the number of solver iterations. If the number of iterations exceeds the *MaxIter*, the simulation is ended. The stopping criteria for the three methods are considered the same, $TolX = TolFun = 10^{-3}$, and *MaxIter* = 30000. First, solving the trajectory planning problem through minimizing tension is considered. The results for direct collocation, GPOPS-II, and B-spline are illustrated in "Fig. 6".

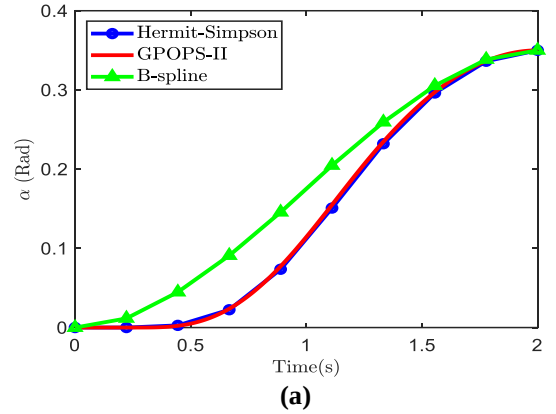

(a)

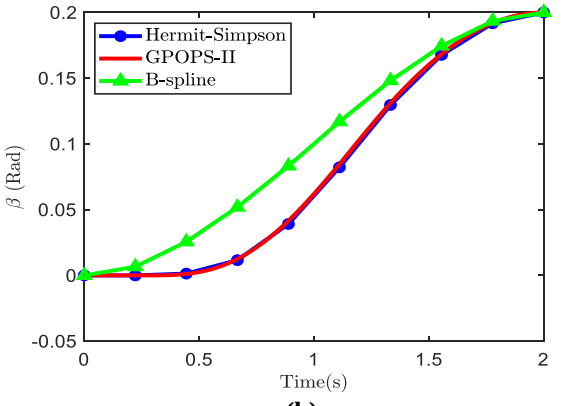

(b)

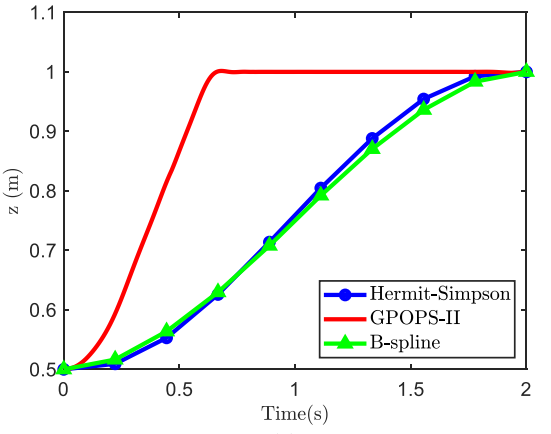

(c)

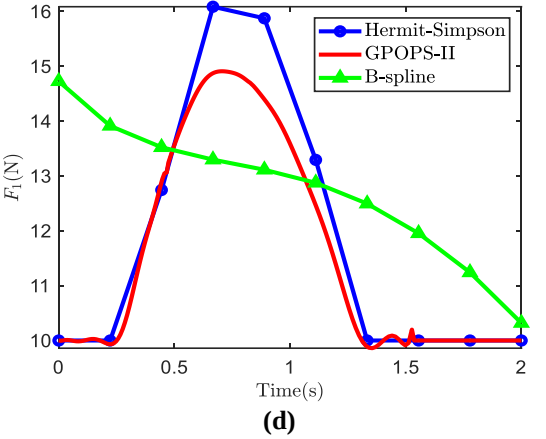

(d)

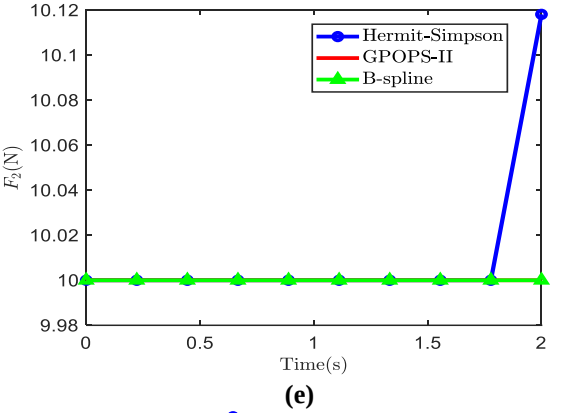

(e)

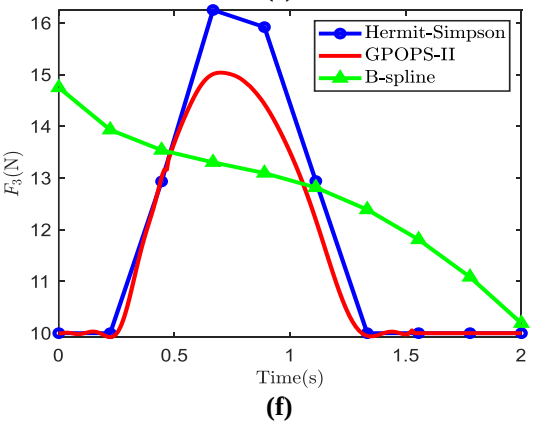

(f)

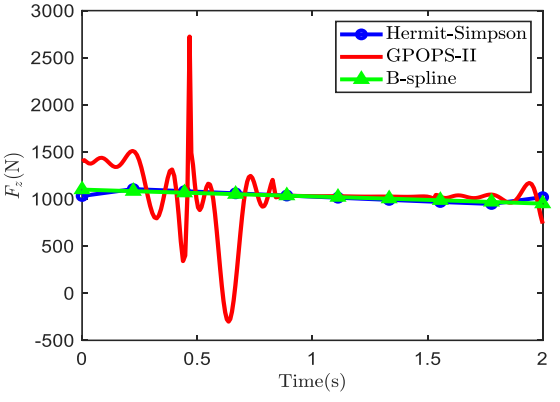

(g)

Fig. 6 Results through minimizing cable's tension.

Table 3 Results for the minimum-tension cost function

Methods	Runtime (s)	Cost function value
Hermite-Simpson	0.86	399
GPOPS-II	10.31	385
B-spline	7.73	427

The results show that Hermit-Simpson's method is superior to other methods in terms of problem-solving time. Also, in the GPOPS-II method, there are drastic changes in increasing or decreasing the force of the pneumatic cylinder, which is not desirable at all. Therefore, as two reliable methods, the results related to the Hermit-Simpson method and B-splines function are proposed. From the viewpoint of the cost function, the results of the Hermit-Simpson method are superior to the B-spline technique. It can also be seen that the changes related to the cable forces in terms of time are less in the case of the B-spline method, and smoother forces have been obtained. Second, the problem is considered by minimizing the tension rate of the cables. The results are shown in "Fig. 7".

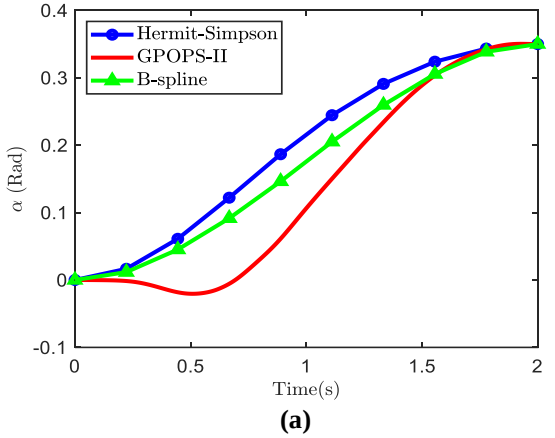

(a)

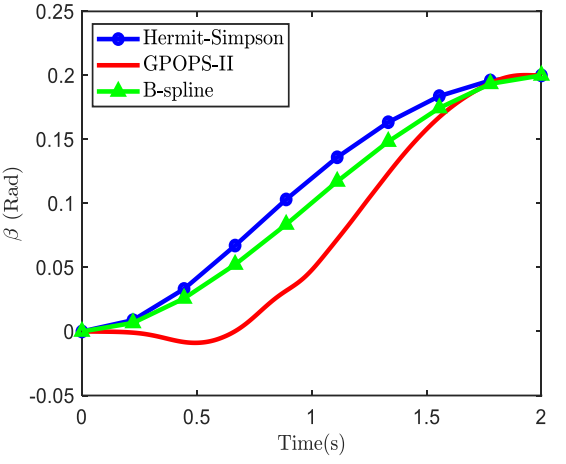

(b)

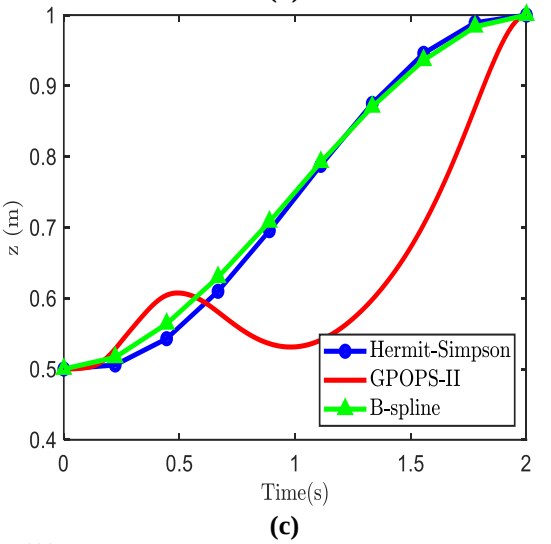

(c)

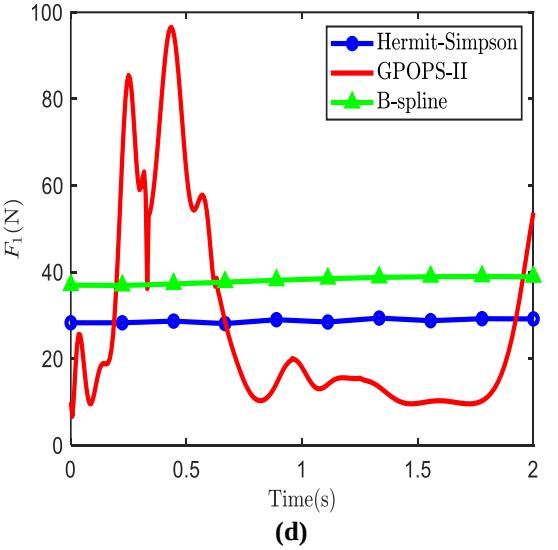

(d)

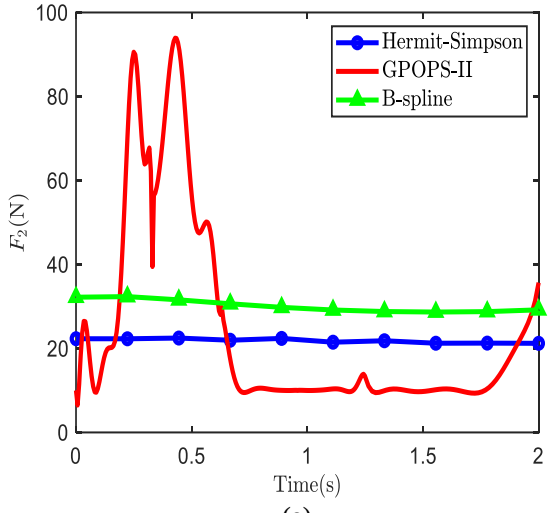

(e)

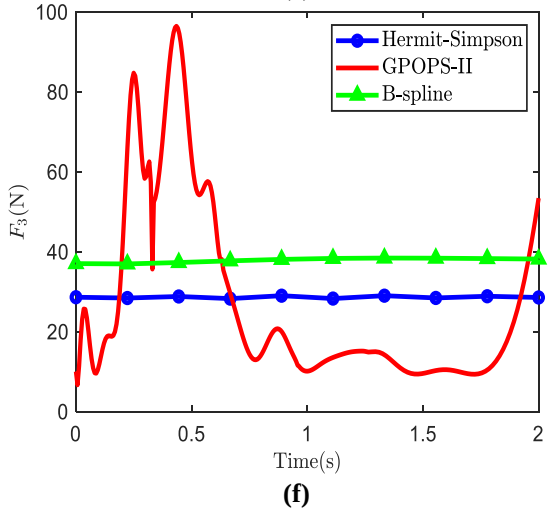

(f)

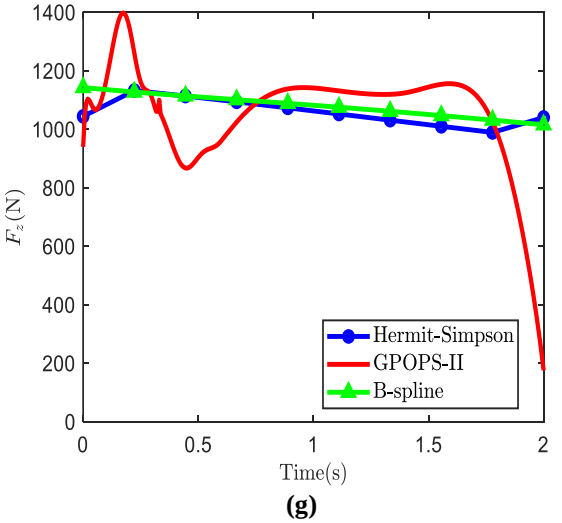

(g)

Fig. 7 Results through minimizing cable's tension rate.

The results show that the B-Spline method is the most time-consuming in terms of runtime. In the GPOPS-II method, there are severe changes in the tension of the cables and the pneumatic cylinder force, which proves that this method is not desirable for meeting the control demands. It is clear from the value of the objective function in "Table 4" that this method could not minimize the value of the cost function. From the viewpoint of minimizing the objective function, the results of the Hermite-Simpson method are significantly superior to the B-spline method.

Table 4 Results for the minimum-tension-rate cost function.

Methods	runtime (s)	Cost function value
Hermite-Simpson	1.16	0.95
GPOPS-II	1.08	272640
B-spline	7.11	10.61

Finally, the cable tensions obtained from two objective functions, minimum-tension and minimum-tension-rate by Hermit-Simpson direct collocation are compared in "Fig. 8".

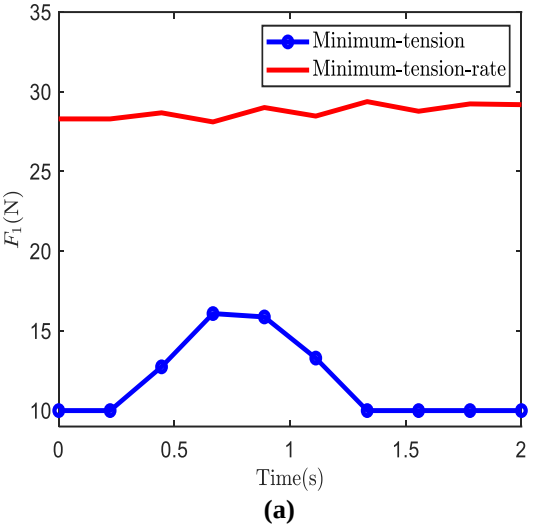

(a)

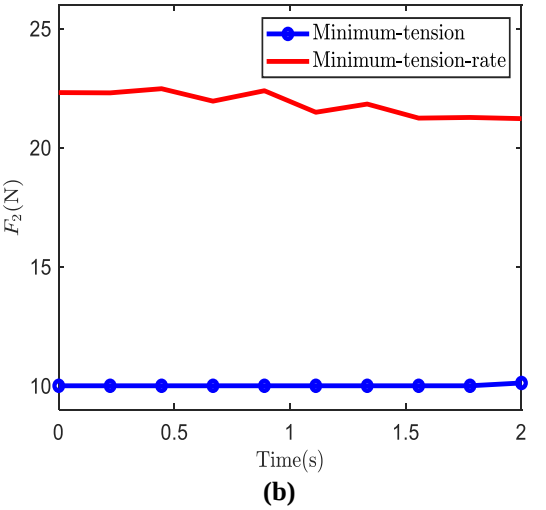

(b)

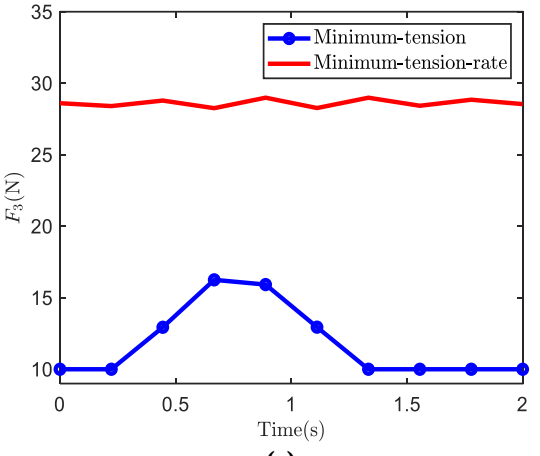

(c)

Fig. 8 Comparing results through minimizing cable's tension and cable's tension-rate.

From "Table 5" and "Fig. 8", it can be seen that if the designer wants the changes in cable forces to be minimal, the function of minimum-tension-rate can be used. However, using this function increases the amount of cable forces. Otherwise, the forces obtained from the simulation with the objective function of minimum-tension give acceptable results.

Table 5 Results of the Hermit-Simpson direct collocation for the minimum-tension (J1) and minimum-tension-rate (J2) objective function

Cost function selection	J_1	J_2
J_1	399	105
J_2	2123	0.95

9 CONCLUSIONS

The development of optimal trajectory planning algorithms is a main issue in efficiently performing cable-driven parallel robot tasks. Direct collocation schemes are considered in this paper to solve the trajectory planning problem for CDPRs. First, the optimization problem and direct schemes were introduced. Then the CDPR kinematics and dynamics are obtained. Next, the problem statement of the trajectory planning is expressed in detail. The trajectory planning's key emphasis was on the cable tensions in the cable robot with the prismatic actuator considering the boundary conditions and positive cable tension constraints. Before the trajectory planning, the MATLAB model is verified by an ADAMS model. The two models have a good agreement in the results of motion parameters to the nonlinear input forces and thus, the CDPR dynamics is correct ("Fig. 5"). Direct collocation approaches in trajectory planning including Hermite-Simpson, GPOPS-II, and B-spline method are compared in "Tables 3 and 4". The results from the minimum-tension objective function from "Table 3 and Fig. 6" in this simulation show that using the Hermite-Simpson and B-spline methods has good performance in minimizing the cost function rather than GPOPS-II. But the Hermite-Simpson is the most accurate and fast among the methods. The results obtained from the minimum-tension-rate objective function from "Table 4 and Fig. 7" show that GPOPS-II is not desirable in satisfying the control demands and could not minimize the value of the objective function. Also, the Hermite-Simpson has a better performance and less runtime rather than B-spline. Thus, this shows that the Hermite-Simpson direct collocation technique is an appropriate method for this trajectory planning problem. Furthermore, this technique can be simply formulated and proposed for other case studies. Also, by comparing the cable tensions in "Table 5 and Fig. 8", the role of cost functions in cable tension management is determined. In the case where minimum-tension-rate is used, the changes in tensions will be less, but the value of cable tensions and consequently the energy consumed is more. As in research [14] and [15], the use of the direct collocation method has brought reliable results. In various research, indirect methods [8], polynomial and harmonic functions [24], and other basic functions have been used for trajectory planning. This issue may be directly related to the unfamiliarity of the direct collocation method. Also, due to the existence of ready toolboxes such as GPOPS-II and default MATLAB software commands, researchers have usually used these toolboxes and commands or previously known methods. Apparently, there are some limitations in this research. In dynamic modeling, the ideal universal joint is considered. Also, friction between the CDPR elements, cable mass, and the moving platform thickness are neglected. But despite this, the presented model has a good match with the Adams model. On the other hand, the mathematical complexities of modeling have been avoided. Also, due to the time limit, three direct methods were compared in solving the trajectory optimization problem, and in future research, other methods can be used in solving the trajectory planning problem.

10 APPENDIX OR NOMENCLATURE

$\mathbf{E}_i$ is the vector from the EE center to the attachment point of the cables after pitch-roll rotation. Hence:

$$\mathbf{E}_i)_{fix} = \mathbf{R}_{\mathbf{PR}}\,\mathbf{E}_i)_{mov}$$

In which $\mathbf{R}_{\mathbf{PR}}$ is the pitch-roll rotation matrix. $\mathbf{E}_i)_{mov}$ is calculated as:

$$\mathbf{E}_1)_{mov} = [r_e \quad 0 \quad 0]^T$$
$$\mathbf{E}_2)_{mov} = [-r_e/2 \quad \sqrt{3}r_e/2 \quad 0]^T$$
$$\mathbf{E}_3)_{mov} = [-r_e/2 \quad -\sqrt{3}r_e/2 \quad 0]^T$$

Hence, $\mathbf{E}_i)_{fix}$ is obtained as follows:

$$\mathbf{E}_1 = [r_e cos\beta \quad 0 \quad -r_e sin\beta]^T$$
$$\mathbf{E}_2 = [\frac{\sqrt{3}r_e sin\alpha sin\beta}{2} - \frac{r_e cos\beta}{2} \quad \frac{\sqrt{3}r_e cos\alpha}{2} \quad \frac{r_e sin\beta}{2} + \frac{\sqrt{3}r_e cos\beta sin\alpha}{2}]^T$$
$$\mathbf{E}_3 = [\frac{-r_e cos\beta}{2} - \frac{\sqrt{3}r_e sin\alpha sin\beta}{2} \quad \frac{-\sqrt{3}r_e cos\alpha}{2} \quad \frac{r_e sin\beta}{2} - \frac{\sqrt{3}r_e cos\beta sin\alpha}{2}]^T$$

Also, the elements of "Eq. (16)" are presented as follows:

$$\mathbf{D(x)} = \begin{pmatrix} m & 0 & 0 \\ 0 & I & 0 \\ 0 & 0 & I \end{pmatrix}, \mathbf{C(x,\dot{x})} = 0, \mathbf{G(x)} = [mg \quad 0 \quad 0]^T$$

REFERENCES

[1] Sohrabi, S., Mohammadi Daniali, H., and Fathi, A., Trajectory Path Planning of Cable Driven Parallel Manipulators, Considering Masses and Flexibility of The Cables, ADMT Journal, Vol. 9, No. 3, 2017, pp. 57-64.

[2] Shahabi, E., Hosseini, M., Kinematic Synthesis of a Novel Parallel Cable Robot as Artificial Leg, ADMT Journal, Vol. 9, No. 3, 2017, pp. 1-10.

[3] Hussein, H., Santos, J. C., and Gouttefarde, M., Geometric Optimization of a Large Scale Cdpr Operating on A Building Facade, In 2018 IEEE/RSJ International Conference on Intelligent Robots and Systems (IROS), 2018: IEEE, pp. 5117-5124.

[4] Phuoc Tho, T., Truong Thinh, N., Evaluating Cable Tension Distributions of CDPR for Virtual Reality Motion Simulator, Mechanics Based Design of Structures and Machines, 2023, pp. 1-19.

[5] H. D. Taghirad, Parallel Robots: Mechanics and Control, CRC press, 2013.

[6] Behzadipour, S., and Khajepour, A., Design of Reduced Dof Parallel Cable-Based Robots, Mechanism and Machine Theory, Vol. 39, No. 10, 2004, pp. 1051-1065.

[7] Zhao, X., Zi, B., and Qian, L., Design, Analysis, And Control of a Cable-Driven Parallel Platform with A Pneumatic Muscle Active Support, Robotica, Vol. 35, No. 4, 2017, pp. 744-765.

[8] Korayem, M. H., Bamdad, M., Tourajizadeh, H., Korayem, A. H., and Bayat, S., Analytical Design of Optimal Trajectory with Dynamic Load-Carrying Capacity for Cable-Suspended Manipulator, The International Journal of Advanced Manufacturing Technology, Vol. 60, No. 1, 2012, pp. 317-327.

[9] Badrikouhi, M., Bamdad, M., Novel Manipulability for Parallel Mechanisms with Prismatic-Revolute Actuators, GA-DP Trajectory Planning Application, Mechanics of Solids, Vol. 56, No. 2, 2021, pp. 278-291.

[10] Riyahi Vezvari, M., Nikoobin, A., Optimal Balancing of Spatial Suspended Cable Robot in Point-To-Point Motion Using Indirect Approach, ADMT Journal, Vol. 10, No. 3, 2017, pp. 87-96.

[11] Alibakhshi, R., Trajectory Optimization of Spherical Parallel Robots Using Artificial Neural Network, ADMT Journal, Vol. 7, No. 1, 2014.

[12] Betts, J. T., Survey of Numerical Methods for Trajectory Optimization, Journal of Guidance, Control, and Dynamics, Vol. 21, No. 2, 1998, pp. 193-207.

[13] Bamdad, M., Time-Energy Optimal Trajectory Planning of Cable-Suspended Manipulators, in Cable-Driven Parallel Robots: Springer, 2013, pp. 41-51.

[14] Hereid, A., Cousineau, E. A., Hubicki, C. M., and Ames, A. D., 3D Dynamic Walking with Underactuated Humanoid Robots: A Direct Collocation Framework for Optimizing Hybrid Zero Dynamics, in 2016 IEEE International Conference on Robotics and Automation (ICRA), 2016: IEEE, pp. 1447-1454.

[15] Kolathaya, S., Guffey, W., Sinnet, R. W., and Ames, A. D., Direct Collocation for Dynamic Behaviors with Nonprehensile Contacts: Application to Flipping Burgers, IEEE Robotics and Automation Letters, Vol. 3, No. 4, 2018, pp. 3677-3684.

[16] Patterson, M. A., and Rao, A. V., GPOPS-II: A MATLAB Software for Solving Multiple-Phase Optimal Control Problems Using Hp-Adaptive Gaussian Quadrature Collocation Methods and Sparse Nonlinear Programming, ACM Transactions on Mathematical Software (TOMS), Vol. 41, No. 1, 2014, pp. 1-37.

[17] Freeman, P., Minimum Jerk Trajectory Planning for Trajectory Constrained Redundant Robots, Washington University in St. Louis ProQuest Dissertations Publishing, 2012.

[18] Campbell, S., Kunkel, P., General Nonlinear Differential Algebraic Equations and Tracking Problems: A Robotics Example, Applications of Differential-Algebraic Equations: Examples and Benchmarks, 2018, pp. 1.

[19] Qian, S., Bao, K., Zi, B., and Zhu, W., Dynamic Trajectory Planning for A Three Degrees-of-Freedom Cable-Driven Parallel Robot Using Quintic B-Splines, Journal of Mechanical Design, Vol. 142, No. 7, 2020, pp. 073301.

[20] Li, Y., T. Huang, T., and Chetwynd, D. G., An Approach for Smooth Trajectory Planning of High-Speed Pick-and-Place Parallel Robots Using Quintic B-Splines, Mechanism and Machine Theory, Vol. 126, 2018, pp. 479-490.

[21] Santos, J. C., Chemori, A., and Gouttefarde, M., Redundancy Resolution Integrated Model Predictive Control of Cdprs: Concept, Implementation and Experiments, in 2020 IEEE International Conference on Robotics and Automation (ICRA), 2020: IEEE, pp. 3889-3895.

[22] Ueland, E., Sauder, T., and Skjetne, R., Optimal Force Allocation for Overconstrained Cable-Driven Parallel Robots: Continuously Differentiable Solutions with Assessment of Computational Efficiency, IEEE Transactions on Robotics, Vol. 37, No. 2, 2020, pp. 659-666.

[23] Dal Bianco, N., Bertolazzi, E., Biral, F., and Massaro, M., Comparison of Direct and Indirect Methods for Minimum Lap Time Optimal Control Problems, Vehicle System Dynamics, Vol. 57, No. 5, 2019, pp. 665-696.

[24] Rahaghi, M. I., Barat, F., Solving Nonlinear Optimal Path Tracking Problem Using a New Closed Loop Direct–Indirect Optimization Method: Application on Mechanical Manipulators, Robotica, Vol. 37, No. 1, 2019, pp. 39-61.

Int. J. Advanced Design and Manufacturing Technology, 2024, Vol. 17, No. 3, pp. 25-30

DOI: ***ISSN: 2252-0406*** ***https://admt.isfahan.iau.ir***

Upgrading Existing CRU Heaters for Energy Saving by Adding Convection Section

Abbas Behzadi *
Esfahan Oil Refining Co.Esafahan
PhD candidate, Department of Mechanical Engineering,
University of Kashan, Kashan
E-mail: Behzadi@eorc.ir
*Corresponding author

Aliakbar Abbassianarani, Ali Arefmanesh
Department of Mechanical Engineering,
University of Kashan, Kashan
E-mail: Abbasian@kashanu.ac.ir

Received: 12 January 2024, Revised: 9 March 2024, Accepted: 25 August 2024

Abstract: Industrial heaters play a pivotal role in various processes in industries and consume significant energy resources. Increasing the energy efficiency of these heaters is of great importance in the current energy-saving scenario. This study improves existing heaters by introducing an additional convective section, using the power of computational fluid dynamics to optimize heat transfer and improve overall efficiency. This paper presents a comprehensive study on upgrading existing heaters by incorporating an additional convection section, facilitated by a thermal and computational study. The main focus is on increasing the efficiency of conventional heaters by optimizing the heat transfer process through the newly added convection section. This paper describes the methodology used to analyze, model, and simulate the reinforced system, presents the results generated by CFD, and discusses the implications of the findings on the overall efficiency of the heaters. In this regard, to study and design the optimal mode of energy saving and complying with the conditions of optimal operational performance, various plans are examined and the best method is selected for heater optimization.

Keywords: Adding Convection Section, Computational Fluid Dynamics, Efficiency Improvement, Upgrading of Existing Heaters

Biographical notes: Abbas Behzadi received his MSc in Mechanical Engineering in 2000 from Amirkabir University of Technology, Tehran, Iran. He has 24 years' experience in the oil industry, Esfahan Refining Co., and has different local certificates regarding mechanical and oil issues. He is a PhD candidate from the University of Kashan and his current research interest includes energy saving and boiler & heater optimization and retrofit. **Aliakbar Abbasianiarani & Ali Arefmanesh,** accordingly, are full Professor & Associate of Mechanical engineering at the University of Kashan, Iran. Their current research focuses on fluid mechanics, thermodynamics and heat transfer.

Research paper

1 INTRODUCTION

Due to the very high temperature of the exhaust gases from the stack of two sets of heaters in the catalytic reformer unit of Isfahan Refinery, including eight cylindrical heaters, the present research was carried out with the aim of optimizing the heaters to recover energy from flue gases and reduce the temperature of the exhaust gases. In the current situation, these gases enter the atmosphere with a temperature of about 1000 °C, so it is possible to optimize the existing heaters by using valid standards and related software. In this research, taking into account the operational conditions of the heaters and in order to increase energy efficiency and reduce environmental pollutants, various options have been investigated, and a convection section is selected and added to retrofit and optimize the existing heaters. By using these studies, the gases from combustion can be used to preheat boiler water (from 117°C to 240°C). With the aim of heat recovery, this issue will increase the efficiency of heaters, save energy, and reduce environmental pollutants.

2 PROCESS DESCRIPTION

The basic design of the research has been such that the combustion gases from four heaters 251 to 254 enter the common duct and exit the common stack with a temperature of about 1000 degrees Celsius, which wastes a lot of energy. The current research aims to use the energy of these gases in order to heat the high-pressure feed water of boilers from the temperature of 117°C to 240°C and reduce the temperature of the exhaust gas from the stack to below 200°C, (“Fig. 1”).

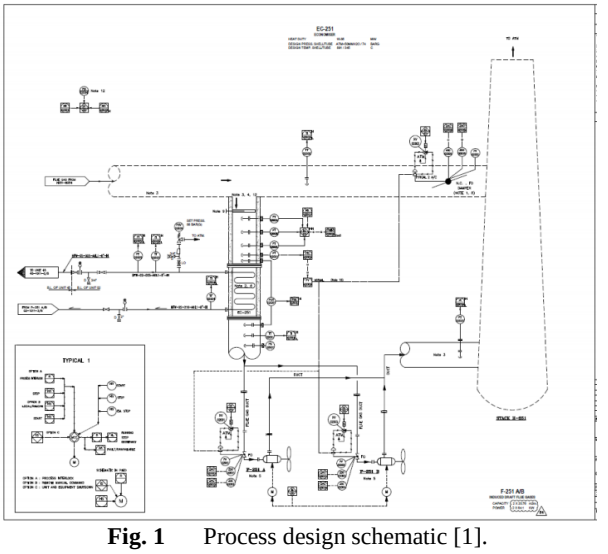

Fig. 1 Process design schematic [1].

The heaters of the catalytic conversion unit produce the feed of light fuel production units such as gasoline, and for this reason, they are important, and their failure will affect the production of light fuel in the country. In this regard, it is very important to observe the pressure of the outlet duct of the heaters to maintain the functioning of the heaters and also to maintain the flame conditions of the burners. In order to maintain the efficiency of heaters, the pressure of 10-25 mm of water in the exhaust gas duct of the heaters should be observed. In this regard, the design of the new convective part should be done considering these conditions.

3 REMOVAL OF THE DAMPER FROM THE COMMON DUCT

The use of a guillotine or damper on the common duct and Inlet guide vane at the inlet of the suction fans to adjust the required suction of the heaters is commonly used in the design of such systems, which is Acceptance of the common design standards, but considering malfunction of burners, the unfavorable experiences and the bad effect on the performance of the heaters in the use of existing dampers for high temperatures, the removal of the damper from the common duct has been investigated and suitable solutions are presented to ensure that the heaters run properly safe.

The operating conditions of the existing heaters are simulated in “Fig. 2” by considering the natural suction of air in the burners. As can be seen, the natural suction of the stack and the Stack effect are created as a result of the temperature gradient and the volumetric mass difference and are applied through the stack length.

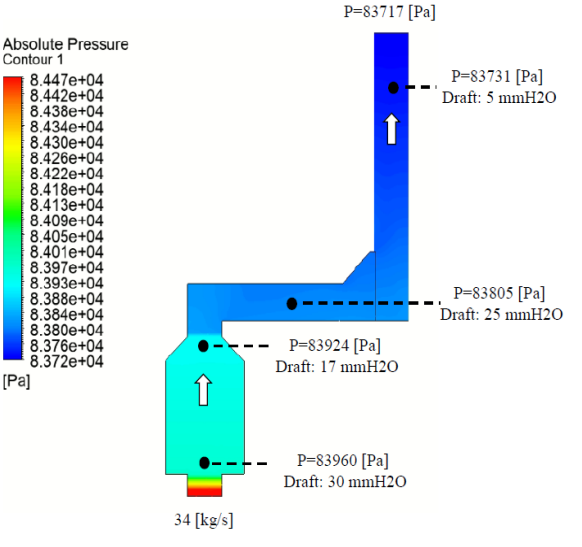

Fig. 2 Existing heaters natural draft.

4 OPTIMUM DESIGN FOR CONVECTION SECTION

Process data for the thermal calculation of a new convection section usually includes various parameters and inputs that are necessary to design an effective and efficient heat transfer system. Operating conditions include the desired temperature range, hot and cold fluid flow rates, and specific application or process requirements. Some of the key process data elements involved in the thermal calculation for a new convection section are as follows, ("Table 1").

Table 1 Process design data

Description	Value		UOM
Flue Gas Flow Rate	34.4 (124000)		Kg/s (kg/hr)
Flue Gas Temperature	900		°C
Flue Gas Density	0.35		Kg/m^3
Flue Gas Pressure in Common Duct	-10~-25		mmH2O
Flue Gas Composition	N2	71.4	Mole%
	H2O	16.7	
	O2	2.49	
	Ar	0.89	
	CO2	8.52	
BFW Inlet Temperature	*117*		°C
BFW Outlet Temperature	240		°C
BFW Inlet Pressure	60		barg
Number of Fans	2 x 50%		-

Considering the 45-year operation of the heaters, as well as the dependence of gasoline production on their performance and the lack of sufficient space, the design of the convection section has faced various problems. In this context, according to the available limited space, the design of the economizer should be done in such a way that the maximum heat exchange between the combustion gases and the feed water of the boilers takes place at the same time, and also the pressure drop should be such that the suction required by the burners is provided and there should be a negative effect on the functioning of the heaters. After reviewing the basic data documents and specifications of the heaters and taking into account the installation time of the equipment and the problems of running out of service for the heaters, in this research, various plans have been examined and studied. The establishment of the convection section on top of the existing common duct and the placement of fans on top of it and the use of a separate short stack on top of the fan to discharge the combustion gases into the atmosphere are considered the best design considering all the technical and operational aspects, ("Fig. 3").

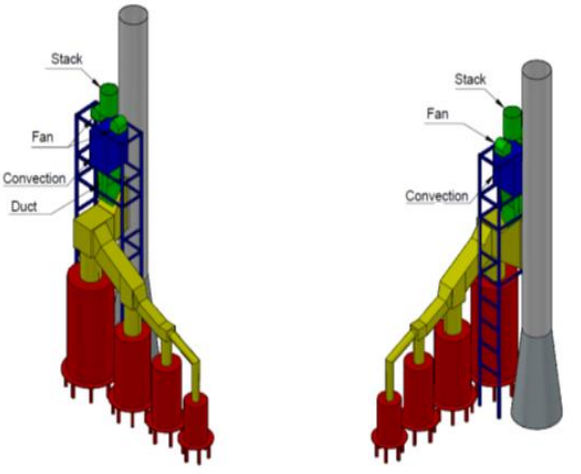

Fig. 3 Predominant schematic plan.

In this design, the gases from combustion are directed into the economizer before being connected to the stack. Then, in order to compensate for the pressure drop in the convection section, these gases enter two fans with 50% of the total capacity and are directed to the atmosphere through a separate stack.

Continuity, momentum, and energy Equations can be expressed in the form of conservative Equations for the general variable ϕ in the form of the following Equations [2].

$$div(\rho\phi\vec{v}) = div(\Gamma\nabla\phi) + S_\phi \quad (1)$$

These Equations can be as Equation (2) for each control volume or cell with a two-dimensional triangular cell in the computational domain [2].

$$\int_S n.(\rho\phi\vec{v})\,dA = \int_S n.(\Gamma\nabla\phi)\,dA + \int_{CV} S_\phi dV \quad (2)$$

In the simulation of flows that undergo separation and eddy formation, it is important to ensure an accurate simulation of the fluid field, to ensure the appropriate mesh size near the walls, respectively the layers around the walls. The height of the first grid cell of the wall is calculated using the following relations [3-4].

$$Re_x = \frac{\rho\, V\, l}{\mu} \quad (3)$$

$$C_f = \frac{0.026}{Re_x^{\frac{1}{7}}} \quad (4)$$

$$\tau_{wall} = \frac{1}{2} C_f\, \rho\, V^2 \quad (5)$$

$$u^* = \sqrt{\frac{\tau_{wall}}{\rho}} \quad (6)$$

$$H_{1st} = \frac{y^* \mu}{u^* \rho} \quad (7)$$

To calculate the height of the first wall from the grid, operating conditions at 70% load are considered and by placing the values, the height of the first cell will be equal to 0.5 mm for y*=5. In order to better detect the formation of eddies due to sudden expansion from the side of the channel, we use the K-Omega SST turbulence model in the Fluent software, which can properly cover y* less than 5 [5].

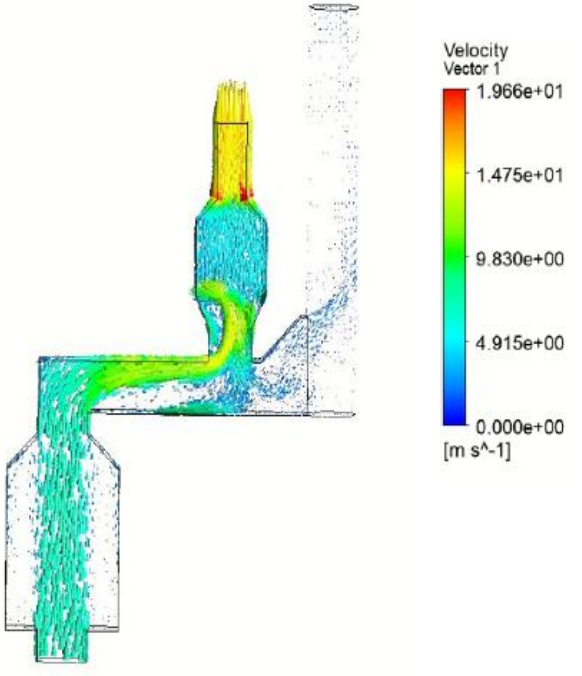

Fig. 4 Fan suction fluid speed at 37 mm of water.

After the investigations, it was determined that the following three situations would occur in this plan:

1- The suction pressure of the fan at the point of branching should be lower than the natural suction pressure of the existing stack due to the stack phenomenon: in this case, a significant percentage of the gas flow from combustion is directed to the atmosphere without passing through the convection section and exchanging heat with the water entering the boilers, which will lead to not achieving the goals of the plan.

2- The suction pressure of the fan at the branching point should be equal to the natural suction pressure of the existing stack due to the stack phenomenon: in this case, about 50% of the gas flow from combustion is directed to the atmosphere without passing through the convection section and exchanging heat with the feed water of the boilers. Therefore, 50% of the combustion gases will reach a temperature of 200°C after passing through the economizer, and the remaining 50% that will enter the stack directly will not have a noticeable temperature change.

3- The suction pressure of the fan at the branching point should be higher than the natural suction pressure of the existing stack due to the stack phenomenon: in this case, the fan suction can be adjusted in such a way that a significant percentage of the flow of combustion gases passes through the convection and exchange section. The heat is directed to the atmosphere with the feed water of the boilers, which will lead to the achievement of the goals of the project. The important point in this plan is to find the optimal performance range of the fan so that the minimum flow through the main stack is achieved simultaneously with the stability of the flames. In "Figs. 4 and 5", the results of fluid pressure and velocity analysis in the fan suction mode equal to 37 mm of water are presented.

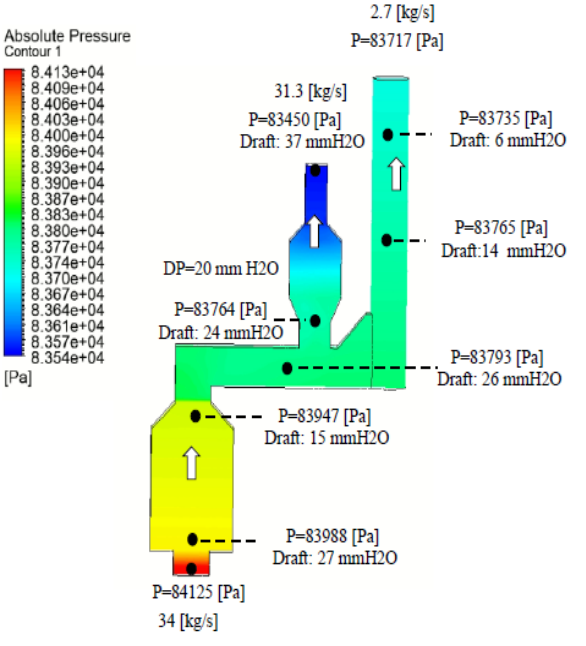

Fig. 5 Fan suction fluid pressure at 37 mm of water.

The speed and fluid pressure conditions in the suction of the fan equal to 32 mm of water are as follows, ("Fig. 6"). As can be seen, reducing the fan suction by 5 mm of water will lead to a reduction in the flow through the convection by 7 kg/s, which will only reduce the efficiency of the convection system and will not change the operation conditions of the heaters. In other words, weak suction by the fan causes some of the combustion gas to escape from the main stack, and strong suction leads air to enter the convection, and the risk in heater operation is minimal. In this regard, the CFD studies conducted show that about 8% of the exhaust gas escapes from the stack path (2.7 kg/s), which can be reduced to less than 5% with manual control. Considering the obstacles and limitations of the existing space and geometry, this design will have the least

changes on the existing infrastructure and will have the most use for diversity in the use of the convective part.

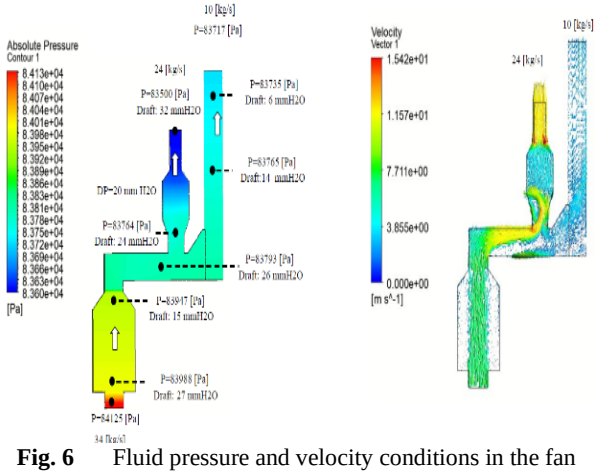

Fig. 6 Fluid pressure and velocity conditions in the fan suction at 32 mm of water.

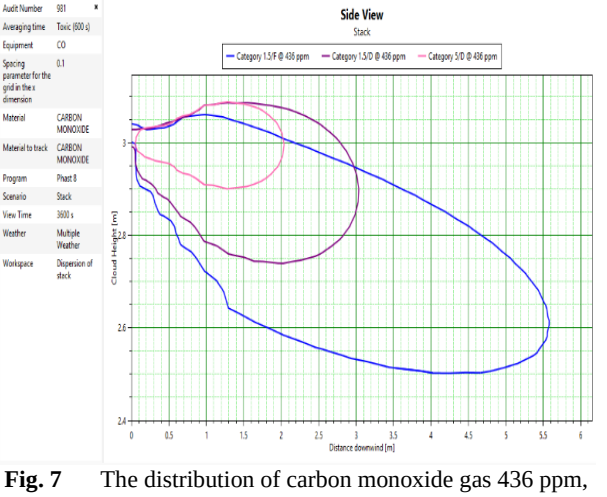

Fig. 7 The distribution of carbon monoxide gas 436 ppm, equivalent to 500 mg/Nm3 [6].

5 DISPERSION STUDY

In this research, due to the importance of the spread of polluting and environmentally damaging gases, the studies and modeling of the distribution of gases coming out of the new stack have been studied. As it is clear from these results, none of the toxic compounds of the outgoing gas stack reach the operating range of the access platforms and according to the height of the stack, it is diluted in the space above the stack.

In this work, the limit of emission of air pollutants in refinery and petrochemical industries has been considered according to the Clean Air Law. The first-class standard is applied to new units (maximum 15 years) and units whose establishment is under the rules and regulations for the establishment of production, industrial, and mineral units, the subject of notification No. 26869/100/97 dated 7/9/1397 of the Environmental Protection Organization to be biocontradictory. In this research, the studies have been done based on the first-class unit, and the height of the stack above the height of the equipment installation has been considered to be 3 meters. Figures 7 and 8 show the distribution of carbon monoxide and sulfur dioxide gases in the conditions of this research.

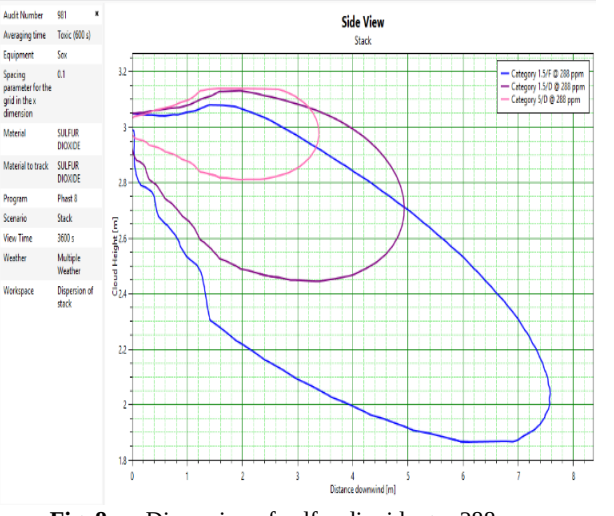

Fig. 8 Dispersion of sulfur dioxide gas 288 ppm equivalent to 752 mg/Nm3 [6].

Table 2 Convection section technical data

TUBE SPECIFICATION		
Design pressure	barg	72
Design temperature	°C	324
No. of tubes	-	360
No. of rows of tubes (banks 1,2&3)	-	4/3/8
No. of flow passes	-	4
Effective tube length	mm	4000
Tube OD	mm	114.3
Average tube wall thickness	mm	8.56
Tube material specification	-	ASTM A106 Gr B
Fin height	mm	15/21
Fin thickness	mm	1.5

6 MECHANICAL DESIGN SPECIFICATION

Designing a convective section for heaters to save energy requires careful consideration of various factors to maximize heat transfer efficiency and minimize heat loss. The technical data used in the construction of the convection section, including thermal conductivity, corrosion resistance, and specific heat, are necessary to

evaluate the heat transfer characteristics. Information on pressure drop limitations, which can affect fluid flow and system efficiency, is considered during the calculation [7], (Table 2).

7 CONCLUSION

In this research, the design of the convection cross-section has been done with the help of thermal calculations and computational dynamic modeling. The project continues with the construction and installation of practical equipment in the operational unit, and its results are examined and confirmed in practice with the performance test. By equipping the common duct of the heaters to the convection section, important achievements including the following in the field of improving the heater performance, reduction of fuel consumption and optimal energy consumption, and reduction of environmental pollution will be achieved:

- Increasing thermal efficiency by at least ten percent for each set of heaters
- Reduction of gas fuel consumption by 90 thousand tons per year for heaters about 15 percent of fuel gas reduction for heaters
- Savings of 8.4 million dollars from the cost of supplying fuel gas
- Reducing smoke emissions to the environment by 3.3 million tons for one year for all heaters
- Reducing carbon dioxide emissions to the environment by 500,000 tons for one year for all heaters.
- Payout time to return the investment of the project for five months

[8]

ACKNOWLEDGMENTS

The author is grateful to the respected managers and colleagues of Isfahan Oil Refining Holding for providing facilities and technical assistance.

REFERENCES

[1] CRU Project Documentation- P& ID Drawings, 2023.

[2] Abbasian Arani, A. A., Arefmanesh, A., and Ehteram, H., Numerical Optimization of Obstructed High Temperature Heat Exchanger for Recovery from The Flue Gases by Considering Ash Fouling Characteristics, International Journal of Numerical Methods for Heat & Fluid Flow, Vol. 30, No. 5, 2020, pp. 2273-2303.

[3] Jagad, P. I., Puranik, B. P., and Date, A. W., A Finite Volume Procedure for Fluid Flow, Heat Transfer and Solid-Body Stress Analysis, International Journal for Computational Methods in Engineering Science and Mechanics, Vol. 19, No. 3, 2018, pp. 171-184.

[4] Velten, K., Lubitz, W., and Hopf, A., Simulation of Airflow Within Horticulture High-Tunnel Greenhouses Using Open-Source CFD Software (Doctoral Dissertation, PhD Thesis, 02, 2018.

[5] Lacombe, F., Pelletier, D., and Garon, A., Compatible Wall Functions and Adaptive Remeshing for the K-Omega SST Model, In AIAA Scitech 2019 Forum, 2019, pp. 2329.

[6] CRU Project HAZOP and SILL Study, 2023.

[7] ASME PTC 4, Fired Steam Generators Performance Test Codes, 2014, https://pdfcoffee.com/asme-ptc-4-2013-pdf-free.html.

Int. J. Advanced Design and Manufacturing Technology, 2024, Vol. 17, No. 3, pp. 31-38

DOI: ***ISSN: 2252-0406*** ***https://admt.isfahan.iau.ir***

Designing and Manufacturing a New Volleyball and Comparison of Kinetic Components with Other Volleyballs

Ehsan Fakhri Mirzanag *, Mohsen Baraghamadi
Department. of Sport Biomechanics, Faculty of Educational Sciences and Psychology, University of Mohaghegh Ardabili, Ardabil, Iran
E-mail: ehsanfakhri6454@gmail.com, barghamadi@uma.ac.ir
*Corresponding author

Hediyeh Koohi
Department. of English Language Teaching, Faculty of Literature and Humanities, University of Mohaghegh Ardabili, Ardabil, Iran.
E-mail: Hediyehkoohi2001@gmail.com

Received: 18 April 2024, Revised: 9 July 2024, Accepted: 8 September 2024

Abstract: Sports equipment is widely available in the international market. The market's focus is on the design of sports equipment to prevent injury, and all equipment must be designed to enable performance without causing injury. The purpose of this study is to design and manufacture a new volleyball and comparison of kinetic components with other volleyballs. The present study is applied and developmental type. We used four full-size Federation International Volleyball (FIVB), official volleyballs (V200W MIKASA made in Japan, FOX volleyball, model Spain, made in the United States, BETA, and new volleyballs made in Iran) to determine the biomechanical components, such as stiffness and Ground Reaction Force (GRF) on that ball. Ground reaction force variables and stiffness of all samples were recorded by a force plate device (sampling rate: 1000 Hz) and Shore C (Newton's per meter N/m), respectively. There was a significant difference in all groups between stiffness ($P<0.001$), vertical ground reaction force (vGRF) ($P<0.001$), and impulse ($P=0.012$), also the LSD Post Hoc test showed that stiffness, vGRF, and impulse in new volleyball and MIKASA volleyball were less than BETA and FOX volleyballs. The results indicate that the biomechanical components of the new volleyball with MIKASA were similar. Therefore, the new volleyball design appears to be suitable for an official competition. Nonetheless, more clinical studies are needed to evaluate the kinetic and kinematic parameters of using new volleyball.

Keywords: Ground Reaction Force, Kinetic, Technology

Biographical notes: Ehsan Fakhri Mirzanag is PhD student of biomechanics and a lecturer at the University of Mohaghegh Ardabili. His current research focuses on mechanical properties characterization of sport tools in order to improve the performance of athletes. **Mohsen Baraghamadi** is an Assistant Professor of the Department of Sport Biomechanics at the University of Mohaghegh Ardabil. His research interests include Kinematics, kinetics, and nonlinear dynamics. **Hediyeh Koohi** is a bachelor student of English language teaching. Her current research focuses on technology, computer programming, and nanomechanics**.**

Research paper

1 INTRODUCTION

Volleyball is a sport that is regarded as one of the most popular in the world [1]. The International Volleyball Federation estimates that 500 million people play volleyball worldwide [2]. To interact with a ball, players must move their body's position and orientation [3]. The result of this interaction depends on the mechanical components of the ball and its kinematic parameters during contact. Collisions of low-to-high velocity are common during serve reception or after an attack [4]. Volleyballs are used in training and competition in various brands and models. A player's contact force with a particular ball could be affected by differences in the coefficient of restitution (COR) between balls. As a result, comprehending the mechanical behavior of various balls during collisions can be advantageous for coaches and athletes [4]. Balls' mechanical properties may have an impact on injuries [4]. When a ball collides with an object, it exerts force on and radiates energy to various tissues such as skin, muscles, tendons, ligaments, and bones [4]. It is possible that the amount of force transferred could result in tissue damage, including injuries like bruises and contusions of muscles, finger ligament sprains, or tendon tears [5]. Head mass and ball size are factors that impact linear and angular head acceleration and contact time, respectively, according to Queen et al.'s 2003 study, while ball inflation pressure has little effect on the impact characteristics. These findings suggest that children should only use the balls of their age. The likelihood of injury among players with smaller heads is a significant indicator, but not as important as it appears in younger people [6]. The forces involved in volleyball collisions must be considered to investigate the causes of injury and determine the design of the ball to ensure safety. On the other hand, in many team sports, participants use a piece of sporting equipment to interact with a ball [7]. In such sports, the ball is an important piece of equipment in the game and generates feedback to players. For this reason, the bounce of the ball has a remarkable effect on the way the game is played [8]. Several factors influence the bounce of the ball: internal factors such as surface texture, internal structure, and pressure; and external factors such as temperature and aerodynamic drag [9]. Previous studies have investigated the effects of varying surface designs on the aerodynamic changes surrounding balls (e.g. volleyballs and soccer balls) flying in the air [10-14]. For example, Hong et al. 2020. Examined the Aerodynamic force of the new volleyball for use in the 2020 Tokyo Olympics. The results indicate that during a float serve, the flight path may vary depending on the type of volleyball and its orientation [15]. However, few reports have explored the effects of materials on the kinetic components in volleyball studies. Biomechanical parameters, such as the vertical ground reaction force (vGRF) and its passive and active peaks, are crucial for analyzing and preventing musculoskeletal injuries [16]. According to reports, increased impact vGRF during sport activity can cause changes in the kinetic and kinematic chain [17-18], which could result in increased stress on other limb structures [19-20]. Volleyballs can exhibit significant morphological changes upon contact, and the resulting energy loss cannot be measured directly [21]. Knudson and Bahamonde 2001 examined biomechanical data collected during object contact, particularly data that included the maximal velocity. However, estimations based on these data may be incorrect because of inappropriate calculations [22]. In addition, nonlinear responses, relative velocity, and energy loss of the ball present significant challenges [23]. Therefore, instead of estimating forces, this study employed force plates to measure directly the relevant forces. Priceet al. 2008, reported that the viscoelastic material properties of the outer panels significantly affected ball impact characteristics, with outer panel materials exhibiting higher levels of viscous damping resulting in higher losses of kinetic energy [24]. The MVA200 (Mikasa Corp., Japan) is now the official volleyball of competitions. Many manufacturers invested in research to develop a similar ball. The Conti Company (Continental Chemical Industries Co., Ltd., Taiwan), one of the well-known manufacturers, provided the prototype balls for this study. In this study, the Type A ball was a prototype designed to imitate official balls, and the Type B ball was a modified version of the type A ball for specific training. Currently, information regarding the dynamics of volleyballs of varying materials and weights is rare, necessitating specific research [21]. So, this study aimed to design and manufacture a new volleyball and compare it with other volleyballs in terms of biomechanical variables. We hypothesized that the kinetics parameter in the new volleyball would be smaller than in other volleyballs.

2 PROCEDURE FOR PAPER SUBMISSION

2.1. The Manufacturing Process of a New Volleyball

2.1.1. Cutting the Panels

The first step in making a volleyball was to cut the panels that would be used to make the volleyball. The panels are made of synthetic leather, which is a durable and water-resistant material. The panels were cut into shapes that were then sewn together to form the volleyball.

2.1.2. Adding the Bladder

After the panels had been cut, the next step was to add the bladder. The bladder is the inner part of the volleyball that holds the air. It is made of latex and was inserted into the volleyball through a small hole. Once the bladder was in place, the hole was sealed to prevent

air from escaping. To maintain the strength and proper spherical shape of the new ball bladder, it was first gauged and kept inside the shelf for 24 hours to ensure that it did not have a puncture. The bladder was made with a special textile instead of rubber to create the second layer of the new volleyball. The attachment of the textile at the joints to the outer surface of the bladder segments guarantees adequate attachment of the fabric, while an adhesive layer is not necessary. Although wear of the woven fabric occurs, this wear provides an appearance to the ball which was comparable to e.g. This appearance is perceived as attractive in particular competes. Accordingly, the choice of a denim outer layer shows that the use of the sports ball enhances the value of the ball[1]. Finally, the newly designed ball textile bladder was made with pu panel synthetic leather [21] [2].

2.1.3. Adding the Graphics

Once the new volleyball had been assembled and the bladder was in place, the next step was to add the graphics.

2.2. Inclusion and Exclusion Criteria

The present research's inclusion criteria included samples of size V5 volleyballs (the competition's official size) weighing between 265-270 grams with an internal air pressure of 4psi, a diameter of 60±66 bounce from a one-meter height resisting against the test of 2000 blows at the speed of 50km/h inside the impact tester for 12 hours with no deformity (“Fig. 1”).

Fig. 1 Sports ball impact testing machine.

Finally, we used four full-size Federation International Volleyball (FIVB), official volleyballs (V200W MIKASA made in Japan, FOX volleyball, model Spain, made in the United States, BETA, and new volleyballs made in Iran) to determine the biomechanical components, for example, stiffness and ground reaction force (GRF) on that ball.

2.3. Quality Control

In the next step was quality control. New volleyball and other samples were inspected to ensure that they meet the required standards for size, weight, and shape. If any defects are found, the volleyballs sample was discarded and a new sample was in its place. In the next step to make sure there were no punctures, all the samples inside the device were placed on shelves for 24 hours.

2.3.1. Circumference Recording

After the impact test was finished, an advanced caliper was used to measure the circumference of the sample volleyballs that were healthy. The measurement method consisted of measuring various points of the volleyballs removed from the impact tester in 12 efforts (“Fig. 2”). The circumference of the sample volleyballs that were not standard-sized according to FIVB were excluded from this stud.

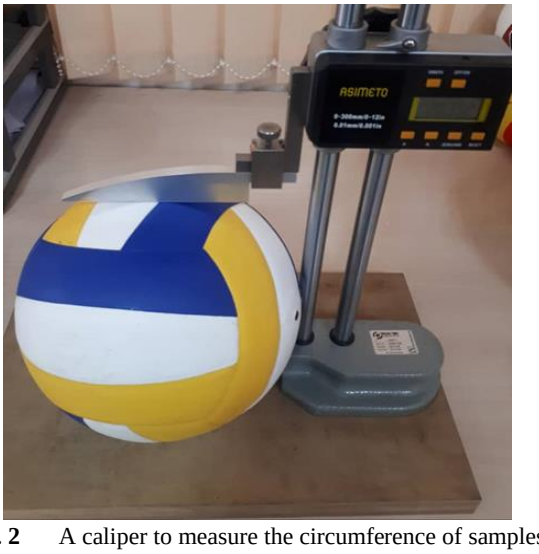

Fig. 2 A caliper to measure the circumference of samples.

2.3.2. Bounce Recording

The bounce of the volleyballs was examined using an advanced bounce machine, model Juiyi, manufactured in China (“Fig. 3”). The approach for measuring the balls’ bouncing top became that all samples were thrown from a top of one meter in 5 efforts with a mean jump of 60±66 cm, consistent with the FIVB. Photoelectric sensor measurement was done, and this machine used the PLC as the electric-controlled system. With such advanced technology, it features strong availability, convenient utility, wide adaptability, high reliability, strong anti-disturbance, simple program design, etc.

[1] https://data.epo.org/publication-server/rest/v1.2/patents/EP1709998NWB1/document.pdf

[2] EUROPEAN PATENT SPECIFICATION, EP 3 528 906 B1

Drop height and rebound height were displayed on the touch screen, accuracy was 1mm (“Fig. 3”).

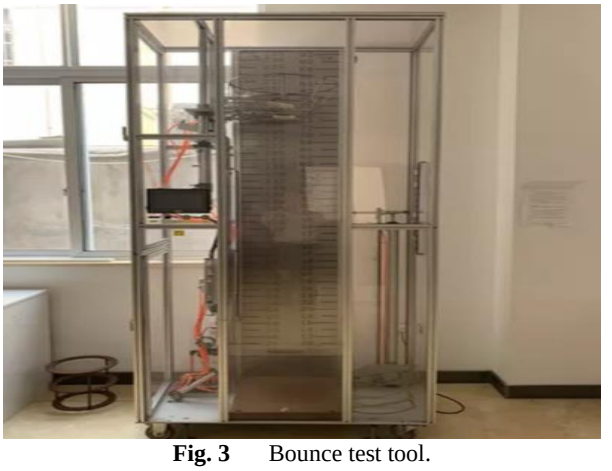

Fig. 3 Bounce test tool.

2.3.3. Weight and Pressure Recording

The weight of the samples was determined by a digital scale manufactured in Tehran, Kala Iran (model EB 9003). Also, a digital pressure gauge from MIKASA was utilized to measure the pressure of the balls. (“Fig. 4”).

Fig. 4 A used Pressure gauge.

2.3.4. Ground Reaction Force Recording

Three-dimensional GRFs were recorded using a force plate (Bertec Corporation, Columbus, 4060–07 Model, OH, United States) sampled at 1000 Hz. Kinetic data were recorded during the dropping of a sample of volleyballs on the force plate from a height of one meter (defined as the interval from ground contact (vertical GRF > 10 N) to ground Separated (vertical GRF < 10 N). Kinetic data were filtered using a third-order low-pass Butterworth filter with a cutoff frequency of 50 Hz.

Figure 5 illustrates the grand averages from the vGRF. The vertical force recorded during the dropping of a sample of volleyballs provided the volleyball contact time, active peak (defined as the highest peak after the impact peak), and the impact peak (defined as the first peak in the vertical force). The time to peak was computed from ground contact to the time of impact peak. The vertical impulse was calculated by extracting the area under the vertical force curve. If no impact peak was present, the highest tangential angle within the first 100 ms during the collision of a sample of volleyballs with a force plate was used to determine the impact peak [25].

Fig. 5 Recording the GRFS using a device designed to reduce the measurement error.

Impulse was calculated for all axes based on the trapezoid integration method [26] as follows:

$$\text{Impulse} = \Delta t\left(\left(\frac{F1 + Fn}{2}\right) + \sum_{i=2}^{n-1} Fi\right)$$

In this equation, delta t is the time period for which the impulse was calculated, F1 and Fn are reaction forces at the first and the last frame.

2.3.5. Stiffness Recording

To determine the Shore hardness, scale C of specimens and articles made of medium hardness rubber according to ASTM D-2240 standard were used. It is used in types of materials such as medium-hardness rubber and plastics, gypsum, plaster, and others [27]. Therefore, in the next step, the stiffness of the samples was measured using a Shore C (model VLX C4 made in China), (“Fig. 6”). For ZERO calibration of the Shore C stiffness tester, we kept the stiffness tester vertically so that the indenter was in the air and the indication in the display should have '0’. Otherwise, we pressed the 'ZERO' key to make the instrument display '0'. All the samples were cut into 10 cm, and the stiffness of the samples was recorded by

applying continuous force and without shock by repeating the effort 5 times using the Shore C device.

Fig. 6 Shore C stiffness tester.

2.4. Statistical Analysis

The standard distribution of the data was confirmed by the Shapiro-Wilk test. A one-way analysis of variance (one-way ANOVA) was used to conduct statistical analyses, along with LSD post hoc tests used for intergroup and between-group comparisons. Statistical Package for Social Sciences (SPSS) version 26 was utilized in all analyses with a significant level of $P< 0.05$.

3 DISCUSSIONS

The study was conducted to design and manufacture a new volleyball and compare its biomechanical properties to other types of volleyballs. One of the essential variables derived from the force-time curve is Impulse [28], biomechanically, the impulse variable covers a large portion of the surface below the force-time curve, therefore, it is expected to have a significant effect on all variables derived from the force-time curve [28]. To optimize athletic performance and prevent injury, biomechanics researchers must consider the importance of each of these variables on impulse, but as far as we know, volleyballs have not been researched in the literature. According to our findings, new and MIKASA volleyball have a lower impulse than BETA and FOX volleyball. Furthermore, the LSD Post Hoc test demonstrates that the new and the MIKASA volleyball had no significant difference in impulse. As a result, the impulse to create a new volleyball with MIKASA and FOX was similar. The impact force on modern soccer balls was examined by Kuizumi et al. 2014, which was used to measure the impulsive force during impact. The maximum impulsive force in the Cafusa sample was the lowest, while Jabulani's impulsive force was the highest among all balls tested at each speed .The flexibility of the surface material and structural characteristics of each ball may be related to these results [29]. Furthermore, according to our findings, new and MIKASA volleyballs have a lower stiffness and vGRF compared to 35BETA and FOX volleyballs. To enhance ball design for safety, it appears that understanding these mechanisms is essential. It was reported that ball types that have a higher peak impact force do not always lose a significant amount of kinetic energy [30]. Internal pressure and stiffness are among the factors that affect the amount of kinetic energy lost and peak force exerted during impact [30]. For example, the increase in stiffness can lead to an increase in impact force, but it can also reduce deformation, resulting in a lower loss of kinetic energy. Examining each variable's role in impact injuries could be valuable if we explore the different combinations of kinetic energy lost and peak impact force for various volleyballs [31]. Additionally, several injuries related to sports activity have been linked to vGRF parameters [31-32]. According to James et al. 2004, dropping cricket balls on the seam had lower impact forces than dropping them perpendicular to the seam [33]. The analysis of different volleyball collision mechanics was investigated by Chiu et al. 2018 at a range of incident velocities. These data indicate that each volleyball type has a distinct behavior during collisions; as a result, the material and speed of the ball have a direct effect on the interaction. The kinetic energy lost was unrelated to peak impact force; of the two ball types with the highest peak impact force, one had the highest and the other the lowest kinetic energy lost. To examine the role of each of these variables in collision injuries, it may be useful to examine the various combinations of kinetic energy lost and peak impact force [34]. In this regard, the findings of the present study demonstrate a significant difference between BETA and FOX volleyballs. However, there was no significant difference between new with MIKASA volleyball, therefore stiffness and vGRF of new with MIKASA volleyball were similar. Many other research projects on volleyballs is related to fluid dynamics and aerodynamic properties of the ball for example Shan Ho et al. 2015 studied to investigate mechanical factors associated with the development of volleyball training. The results indicated that different volleyballs of the same size, weight, and internal air pressure have dissimilar mechanical features and implied that slight adjustments to ball structure can cause substantial changes in the specific characteristics. In addition, the weight increased the momentum lost, which could cause the ball to bounce unexpectedly [35]. Some limitations need to be discussed in this study. First, we included volleyballs as a sample, which is why the outcomes of this study are specific to the population under investigation. As a result, they cannot be transferred to other sports balls. There is a need for more research in this area. Second, kinematic data was not

recorded in this study and this biomechanical component's response to different volleyball conditions is unknown to us. Future research should focus on this. Finally, our study has not prospectively recorded injury rates. Future studies should realize this.

Table 1 Mean and standard deviation of the weight (kg), deformation (cm), and bonce (cm) for all groups

Parameter	BETA	FOX	NEW BALL	MIKASA	P-values
Weight	268.00±.0.00	268.66±.0.57	268.66 ±0.57	268.66 ±0.57	0.330
Deformation	65.91±.0.792	65.73±0.753	66.90±0.796	64.78±0.750	0.850
Bounce	66.45±0.790	65.04±0.789	66.20±0.798	65.98±0.796	0.559

*Stand for significant difference p<0.05

4 FIGURES, TABLES, AND OTHER IMAGES

There was no significant difference between the four volleyball types in weight, deformation, and bonce. However, demographic characteristics of all types were similar (P>0.05, "Table 1").

There was a significant difference in all groups between stiffness, vertical ground reaction force (vGRF), and impulse (P<0.001), also the LSD Post Hoc test showed that stiffness, vGRF, and impulse in new volleyball and MIKASA volleyball were less than BETA and FOX volleyballs. Findings did not demonstrate any significant difference in time to peak (TT_P) among all groups (P>0.05, "Table 2").

Table 2 Mean and standard deviation of the stiffness and ground reaction force for all groups

Parameter	BETA	FOX	NEW BALL	MIKASA	P-values
Stiffness	61.80±.1.78	61.40±.1.67	54.20±.0.83	53.80±.0.83	0.000*
vGRF	620.35±.17.77	573.80±.10.78	525.57±.41.82	520.25±.5.98	0.000*
Impulse	10.05±.1.53	8.07±.0.63	7.53±.1. 28	7.72±0.97	0.012*
TT_p	6.00±0.00	6.20±0.44	6.40 ±.0.54	6.20±0.44	0.532

*Stand for significant difference P<0.05

*vGRF; Vertical ground reaction force, TTp; Time to peck, kg; Kilogram, cm; Centimeter, NEWBALL; New volleyball

There was a significant difference between the stiffness and vGRF of the new volleyball with BETA and FOX volleyballs (P<0.001), However, there was no significant difference between the new volleyball with MIKASA, therefore stiffness and the vGRF of the new volleyball with MIKASA were similar. There was a significant difference between the impulse of the new volleyball with BETA volleyball, Also, the LSD Post Hoc test showed that the impulse of a new volleyball with FOX and MIKASA was not significantly different. Therefore, the impulse of the new ball with MIKASA and FOX volleyball was similar (P>0.05, "Table 3").

Table 3 Statistically significant differences between all groups for biomechanical variable

Variables	Row	Group	P-values
Stiffness	NEW Ball	BETA	<0.001*
		FOX	<0.001*
		MIKSA	0.648
	BETA	FOX	0.648
		MIKSA	<0.001*
	FOX	MIKSA	<0.001*
vGRF	NEW Ball	BETA	<0.001*
		FOX	0.005
		MIKSA	0.725
	BETA	FOX	0.007
		MIKSA	<0.001*
	FOX	MIKSA	0.002
Impulse	NEW Ball	BETA	0.003
		FOX	0.471
		MIKSA	0.808
	BETA	FOX	0.016
		MIKSA	0.006
	FOX	MIKSA	0.630

TT_P	NEW Ball	BETA	0.150
		FOX	0.461
		MIKSA	0.461
	BETA	FOX	0.461
		MIKSA	0.461
	FOX	MIKSA	0.100

*Stand for significant difference $p<0.05$

5 CONCLUSIONS

The results indicate that the biomechanical components of the new volleyball with MIKASA were similar. Therefore, the new volleyball design appears to be suitable for an official competition. Nonetheless, more clinical studies are needed to evaluate the kinetic and kinematic parameters of using new volleyball.

REFERENCES

[1] Silva, M., Marcelino, R., Lacerda, D., and João, P.V., Match Analysis in Volleyball: a Systematic Review, Montenegrin Journal of Sports Science and Medicine, Vol. 5, No. 1, 2016, pp. 35.

[2] Reeser, J. C. J. H. O. S. M. Volleyball, S., Introduction: a Brief History of The Sport of Volleyball, 2023, pp. 1-7.

[3] Hendee, S. P., Greenwald, R. M., and Crisco, J. J., Static and Dynamic Properties of Various Baseballs, Journal of Applied Biomechanics, Vol. 14, No. 4, 1998, pp. 390-400.

[4] Chiu, L. Z., Von Gaza, G. L., Analysis of Different Volleyballs' Collision Mechanics Across a Range Of Incident Velocities, Sports Biomechanics, Vol. 19, No. 6, 2020, pp. 817-830.

[5] Miura, K., Tsuda, E., Kogawa, M., and Ishibashi, Y., The Effects of Ball Impact Position on Shoulder Muscle Activation During Spiking in Male Volleyball Players, JSES International, Vol. 4, No. 2, 2020, pp. 302-309.

[6] Queen, R. M.,Weinhold, P. S., Kirkendall, D. T., and Yu, B., Theoretical Study of The Effect of Ball Properties on Impact Force in Soccer Heading, Medicine & Science in Sports & Exercise, Vol. 35, No, 12, 2003, pp. 2069-2076.

[7] Komi, E., Roberts, J., and Rothberg, S., Measurement and Analysis of Grip Force During a Golf Shot, Part P: Journal of Sports Engineering, Technology, Vol. 222, No. 1, 2008, pp. 23-35.

[8] Rezaei, A.,Verhelst, R., and Van Paepegem, W., Degrieck, J., Finite Element Modelling and Experimental Study of Oblique Soccer Ball Bounce, Vol. 29, No. 11, 2011, pp. 1201-1213.

[9] Wiart, N., Kelley, J., James, D., and Allen, T., Part P: Journal of Sports Engineering, Technology, Effect of Temperature on the Dynamic Properties of Soccer Balls, Vol. 225, No. 4, 2011, pp. 189-198.

[10] Asai, T., Ito, S., Seo, K., and Hitotsubashi, A., Fundamental Aerodynamics of a New Volleyball, Sports Technology, Vol. 3, No. 4, 2010, pp. 235-239.

[11] Asai, T., Ito, S., Seo, K., and Hitotsubashi, A., Aerodynamics of a New Volleyball, Procedia Engineering, Vol. 2, No. 2, 2010, pp. 2493-2498.

[12] Mehta, R., Alam, F., and Subic, A., Review of Tennis Ball Aerodynamics, Sports Technology, Vol. 1, No. 1, 2008, pp. 7-16.

[13] Asai, T., Seo, K., Aerodynamic Drag of Modern Soccer Balls, Springer Plus, Vol. 2, No. 1, 2013, pp. 1-5.

[14] Alam, F., Chowdhury, H., Stemmer, M., Wang, Z., and Yang, J., Effects of Surface Structure on Soccer Ball Aerodynamics, Procedia Engineering, Vol. 34, 2012, pp. 146-151.

[15] Hong, S., Ozaki, H., Watanabe, K., and Asai, T., Aerodynamic characteristics of New Volleyball for the 2020 Tokyo Olympics, Applied Sciences, Vol. 10, No. 9, 2020, pp. 3256.

[16] Jiang, X., Napier, C., Hannigan, B., Eng, J. J., and Menon, C., Estimating Vertical Ground Reaction Force During Walking Using a Single Inertial Sensor, Sensors, Vol. 20, No. 15, 2020, pp. 4345.

[17] Ghasemlou, N., Kerr, B. J., and David, S., Tissue Displacement and Impact Force are Important Contributors to Outcome After Spinal Cord Contusion Injury, Experimental Neurology, Vol. 196, No., 2005, pp. 9-17.

[18] Hong, Y., Wang, S. J., Lam, W. K., and Cheung, J. T. M., Kinetics of Badminton Lunges in Four Directions, Journal of Applied Biomechanics, Vol. 30, No. 1, 2014, pp. 113-118.

[19] Munteanu, S. E., Barton, C. J., Lower Limb Biomechanics During Running in Individuals with Achilles Tendinopathy: A Systematic Review, Journal of Foot and Ankle Research, Vol. 4, 2011, pp. 1-17.

[20] Mousavi, S. H., Hijmans, J. M., Rajabi, R., Diercks, R., Zwerver, J., and Van der Worp, H., Kinematic Risk Factors for Lower Limb Tendinopathy in Distance Runners: A Systematic Review and Meta-Analysis, Gait & posture, Vol. 69, 2019, pp. 13-24.

[21] Ho, C. S., Lin, K. C., Chen, K. C., Yan, Z. T., and Chang, C. H., Mechanical factors Associated with The Development of Training Volleyballs, Part P: Journal of Sports Engineering, Technology, Vol. 230, No. 2, 2016, pp. 84-89.

[22] Knudson, D., Bahamonde, R., Effect of Endpoint Conditions on Position and Velocity Near Impact in Tennis, Vol. 19, No. 11, 2001, pp. 839-844.

[23] Smith, L. V., Duris, J. G., Progress and Challenges in Numerically Modelling Solid Sports Balls with Application to Softballs, Vol. 27, No. 4, 2009, pp. 353-360.

[24] Price, D., Jones, R., Harland, A., and Silberschmidt, V. V., Viscoelasticity of Multi-Layer Textile Reinforced Polymer Composites Used in Soccer Balls, Vol. 43, 2008, pp. 2833-2843.

[25] Jafarnezhadgero, A. A., Sorkhe, E., and Oliveira, A. S., Motion-Control Shoes Help Maintaining Low Loading Rate Levels During Fatiguing Running in Pronated Female Runners, Gait & posture, Vol. 73, 2019, pp. 65-70.

[26] Jafarnezhadgero, A., Fatollahi, A., Amirzadeh,N., Siahkouhian, M., and Granacher, U., Ground Reaction Forces and Muscle Activity while Walking on Sand Versus Stable Ground in Individuals with Pronated Feet Compared with Healthy Controls, PloS one, Vol. 14, No. 9, 2019, pp. e0223219.

[27] Zhao, H., Allanson, D., Ren, X. J., and Engineering, C., Use of Shore Hardness Tests for in-Process Properties Estimation/Monitoring of Silicone Rubbers, Vol. 3, No. 07, 2015, pp. 142-147.

[28] Mizuguchi, S., Sands, W. A., Wassinger, C. A., Lamont, H. S., and Stone, M. H., A New Approach to Determining Net Impulse and Identification of Its Characteristics in Countermovement Jumping: Reliability and Validity, Sports Biomechanics, Vol. 14, No. 2, 2015, pp. 258-272.

[29] Koizumi, A., Hong, S., Sakamoto, K., Sasaki, R., Asai, T., A Study of Impact Force on Modern Soccer Balls, Procedia Engineering, Vol. 72, 2014, pp. 423-428.

[30] Padua, D. A., DiStefano, L. J., Sagittal Plane Knee Biomechanics and Vertical Ground Reaction Forces are Modified Following ACL Injury Prevention Programs: A Systematic Review, Sports Health, Vol. 1, No. 2, 2009, pp. 165-173.

[31] Knowles, B. M., Dennison, C. R., Predicting Cumulative and Maximum Brain Strain Measures from HybridIII Head Kinematics: A Combined Laboratory Study and Post-Hoc Regression Analysis, Annals of Biomedical Engineering, Vol. 45, 2017, pp. 2146-2158.

[32] Van der Worp, H.,Vrielink, J. W., Bredeweg, S. W., Do Runners Who Suffer Injuries Have Higher Vertical Ground Reaction Forces Than Those Who Remain Injury-Free? A Systematic Review and Meta-Analysis, British Journal of Sports Medicine, Vol. 50, No. 8, 2016, pp. 450-457.

[33] Carre, M. E., James, D., Haake, S., Impact of a Non-Homogeneous Sphere on A Rigid Surface, Proceedings of the Institution of Mechanical Engineers, part C: Journal of Mechanical Engineering Science, Vol. 218, No. 3, 2004, pp. 273-281.

[34] Chiu, L. Z., Analysis of Different Volleyballs' Collision Mechanics Across a Range of Incident Velocities, Sports biomechanics, 2018.

[35] Ho, C. S., Lin, K. C., Chen, K. C., Chiu, P. K., and Chen, H. J., System Design and Application for Evaluation of Blocking Agility in Volleyball, Proceedings of the Institution of Mechanical Engineers, Part P: Journal of Sports Engineering and Technology, Vol. 230, No. 3, 2016, pp. 195-202.

Int. J. Advanced Design and Manufacturing Technology, 2024, Vol. 17, No. 3, pp. 39-48

DOI: ***ISSN: 2252-0406*** ***https://admt.isfahan.iau.ir***

Determination of Reinforcement Learning Reward Parameters to Solve Path Planning of Unknown Environments by Design of Experiments

Issa Alali Alfares, Ahmad Reza Khoogar *
Faculty of Materials & Manufacturing Technologies, Malek Ashtar University of Technology, Tehran, Iran
E-mail: issa.alifares@mut.ac.ir, khoogar@gmail.com
*Corresponding author

Received: 14 July 2024, Revised: 9 August 2024, Accepted: 8 September 2024

Abstract: The Reinforcement Learning Approach (RL) is used to solve the path-planning problem of an autonomous mobile robot in unknown environments. Despite that RL is a recent and powerful tool, it requires a lot of training processes because there are so many parameters in the agent's training process. Some of these parameters have a larger effect on the convergence of the learning process than others, so, knowing these parameters and their suitable values makes the training process more efficient, saves time, and consequently makes the trained agent execute the required task successfully. No analytical equations are available to determine the best values for these parameters, therefore, in this paper, a statistical analysis is made using the design and analysis of experiment (DoE) methods to determine the parameters that have the largest effect on the training process. After that, analysis is done to determine the values of the most effective parameters. Results show that the determined parameters lead to a successful autonomous path planning in different unknown environments

Keywords: Autonomous Path Planning, Design of Experiment, Mobile Robot, Reinforcement Learning, Reward, Training Parameters

Biographical notes: Issa Alali Alfares received his MSc in applied design and mechatronics from Malek Ashtar University of Technology (MUT), Iran, in 2010. Currently, he is a PhD student at Malek Ashtar University of Technology Tehran, Iran doing his research in robot navigation using machine learning and artificial intelligence methods. **Ahmad Reza Khoogar** received his PhD in Mechanical Engineering from the University of Alabama in Tuscaloosa in 1990. He is currently an Associate Professor at the Faculty of Materials & Manufacturing Technologies, Malek Ashtar University of Technology Tehran, Iran. His current research interests include Robotics and Mechatronic systems.

Research paper

1 INTRODUCTION

Mobile robot applications have been spread almost in everyday human life, and robots must be able to move efficiently and safely in various environments. Path planning is the fundamental task necessitated by any mobile robot and it is the most important part of any navigation process, it must address challenges such as perception, cognition, human-robot interaction, and obstacle avoidance. There exists a large number of path-planning methods that have been developed in recent decades to ensure the generation of collision-free trajectories. However, each method has its own set of advantages and disadvantages, thereby, this field of research is still one of the most extensively studied and investigated scientific domains.

Path planning methodologies are divided into two primary categories: classical and intelligent [1]. The major drawbacks of the classical approaches are the computational expenses, and the inability to deal with unknown environments [2]. Most of the new studies focus on intelligent methods such as artificial neural networks [3], reinforcement learning [4], genetic algorithms [5], fuzzy logic [6], cuckoo search [7], and various other techniques which are mainly based on artificial intelligence [8], and the ability of the robot to learn enabling it to acquire knowledge and make decisions in new scenarios.

There is a tendency among researchers to solve the mobile robot navigation problem using reinforcement learning (RL) methods since they are simple, diverse, and more suitable for unknown systems that have a great amount of uncertainty. The main problem with RL methods is that they require a lot of training processes to reach a successful training agent. The classical method is to try different values of these parameters manually but it is a very time-consuming operation.

Design and Analysis of Experiment (DoE) is a statistical method widely used for product design and development as well as optimization [9-10]. These methods find their way into almost all fields of engineering. For instance, in mechanical engineering, DoE methods are applied to study the suspension system of a car to improve the ride comfort of a vehicle at various speed domains [11], whereas Hussain et al. employ DoE methods to find the best combination of the parameters of the device that is used to measure the cylindricity of the engine cylinder core [12]. Another field for applying DoE methods is civil engineering and road construction in [13]. Also, DoE methods are applied vastly in material sciences and the study of the corrosion process on a steel alloy in a harsh salty environment [14]. Moreover, due to the simplicity and time cost-saving of DoE approaches, they are applied in medical researchers in radiotherapy [15]. Unlimited list can be mentioned here, in transport [16], product reliability improvement [17], electronics, and computer products industry [18], Energy production [19] and many other fields.

Other approaches are used in conjunction with DoE methods to execute efficient research. Vieira et al [20] employ the design and analysis of experiments approach in combination with an artificial neural network (ANN) to improve the operation of a steam generator used for a power generation plant. A model to estimate the efficiency of the steam generator using ANN is built then the DoE method is applied to study the effect of seven parameters on the steam generator performance. While another study applied the DoE with ANN to evaluate and optimize a chemical material that is used to produce fuels and other chemical products [21]. So, it can be said that DoE is a powerful and reliable tool to study the effect of multiple parameters on a certain process. DoE gives the best inference possible of the executed experiments and it notably decreases the total number of the necessary experiments.

In this paper, DoE is used to determine the parameters of a new reward function of a reinforcement learning agent defined especially to solve the path planning of an autonomous mobile robot in different unknown environments. The main goal of using DoE is to reduce the total number of the training operations of the RL agent which takes a very long time to be done.

The remainder of the paper is organized as follows: In the following section, a theoretical background is stated to clarify the definition of the new proposed reward function then a factorial design is suggested to decrease the total number of training operations and all the data collected is summarized in the designed table of experiment. After that analysis of the data to determine the parameters with the highest effect on the training process is done. To evaluate the training agent with the obtained values, experimental tests are carried out to solve path planning in different environments. Finally, a summary of what has been achieved in this paper is presented in the conclusion section.

2 THEORITICAL BACKGROUND

Reinforcement learning (RL) approaches depend on the interaction between the agent and the environment to achieve the learning of the agent. No previous model is required for RL methods, because they depend on trial and error to learn the agent. To solve any problem with RL, three phases must be carried out. Setup phase, training phase and test phase. In the setup phase, the problem should be defined and formulated which means to choose a suitable and meaningful definition of the RL problem components; the state space, the action space, and the reward signal.

The most distinguishing feature of RL is that taking good actions after training depends on maximizing a

reward function which is the most important component of the RL method. In order to define the reward function, previous studies and research divide the state space into four or five kinds of states: safe, unsafe, winning, and failure state [22-25]. Then they define the reward signal as a real number for each transition from one kind of state to another kind of state. Other researchers used a reward function that assigns a value of (+1) to the goal state, a value of (-1) for the collision state, and a value of (0) to all other states [26]. Other studies [27] even consider a much simpler definition of the reward to be (-1) if the distance between the robot and the obstacles becomes less than a certain limit, and a value of (0) otherwise. All the previous definitions simplify the real environment by considering an infinite number of real situations as one state, but this representation is unrealistic and inaccurate; however, those methods can find solutions only in simple cases and they are not applicable in complicated real environments.

To tackle this problem, we propose a totally new definition of the reward function taking into consideration the following points:

- The agent should receive a high positive reward for successfully reaching the target position because this behavior is highly desired.
- The agent should be highly penalized if it collides with an obstacle.
- The agent should get a small positive or a small negative reward due to the transition from one state to a "better" or "worse" state.

So, we suggest a total reward function r which is a weighted sum of five partial rewards r_1, r_2, r_3, r_4, r_5. These partial rewards are related respectively to: the distance between the robot and the goal point, the changes in distance between the robot and the goal, the distances between the robot and the different obstacles, the changes in distances between the robot and the obstacles, and finally how long the robot takes to reach the goal.

$$r = a_1.r_1 + a_2.r_2 + a_3.r_3 + a_4.r_4 + a_5.r_5 \quad (1)$$

Where; a_1, a_2, a_3, a_4, a_5 are the weights of partial rewards and the value of these parameters will be determined during the training process of the RL agent which is represented by a deep neural network. These weights express the relative importance of the different parts of the total reward, and determining the best values of these parameters is the core of our study.

As for r_1, it is related to the distance between the robot and the target. This amount must take an increasingly high value as the robot gets close to the target. So, r_1 is suggested to be in the next form:

$$r_1 = \frac{1}{(d_t(r,T))^2} \quad (2)$$

Where: $d_t(r,T)$ is the distance between the robot and the goal point at step t. "Eq. (2)" shows that if the distance between the robot and the target $d_t(r,T)$ becomes smaller, the reward r_1 will be bigger.

As for r_2, it takes the highest value possible of the reward, which is $(+100)$ when the robot reaches its target. Otherwise, the value of r_2 will depend on the distance change between the robot and the target. If the robot is coming closer to the target, then it will receive a positive reward proportional to the rate of how much this closeness happens. Symmetrically, if the robot is going farther from the target, then it will receive a negative reward proportional to the rate of how much this change happens.

$$r2 = \begin{cases} +100 & if\ the\ robot\ reaches\ the\ goal \\ \dfrac{d_{t-1}(r,T) - d_t(r,T)}{max\ (d_{t-1}(r,T), d_t(r,T))} & otherwise \end{cases} \quad (3)$$

Where: $d_{t-1}(r,T)$ is the distance between the robot and the goal at step $t-1$.

Regarding r_3, it is related to the distance between the robot and the different obstacles. Of course, if the distance between the robot and the obstacles becomes smaller, the negative reward must be bigger in this case. Taking that into consideration, we suggest the following definition of r_3:

$$r_{3i} = \frac{-1}{(d_t(r,o_i))^2} \qquad i = 1,2,\dots,n \quad (4)$$

$$r_3 = r_{31} + r_{32} + \cdots + r_{3n} \quad (5)$$

Where; $d_t(r,o_i)$ is the distance between the robot position and the obstacle position detected in direction i at step t. n is the number of the directions that the robot senses the existence of obstacles in that direction which falls in the range of the sensor.

As for r_4, It depends on the distance changes between the robot and other obstacles that are moving and sensed by the robot in different directions. We suggest the following definition of r_4:

$$r_{4i} = \frac{d_t(r,o_i) - d_{t-1}(r,o_i)}{d_t(r,o_i)} \qquad i = 1,2,\dots,n \quad (6)$$

$$r_4 = r_{41} + r_{42} + \cdots + r_{4n} \quad (7)$$

Where; $d_{t-1}(r,o_i)$ is the distance between the robot position and the obstacle position detected in direction i at step $t-1$.

As for the last part of the reward r_5, it is just a constant reward that reflects the effect of the number of steps needed to reach the goal, or in other words the less time spent to reach the goal the better performance the robot makes. So, a negative reward(punishment) is added at each extra time step. So, as stated above the main goal of this study is to find the best values of the parameters a_1, a_2, a_3, a_4, a_5 defined in "Eq. (1)".

3 PREPARING AND GATHERING DATA

In this section, the second phase of the RL approach which is training the RL agent and gathering the data needed to determine the best values of the reward function is explained.

In the RL approach, the training is done through the interaction between the agent and the environment. The agent that we propose to learn is a deep Q-neural network (DQN). To do that, a MATLAB platform was built to represent the simulation environment in which the RL algorithm will be implemented. This platform is provided with all the information that may be needed in the simulation process like the environment where the navigation is taking place, the start point, the goal point, and all the information related to the obstacles like their numbers, shapes, and positions, movement, and their speed ("Fig. 1").

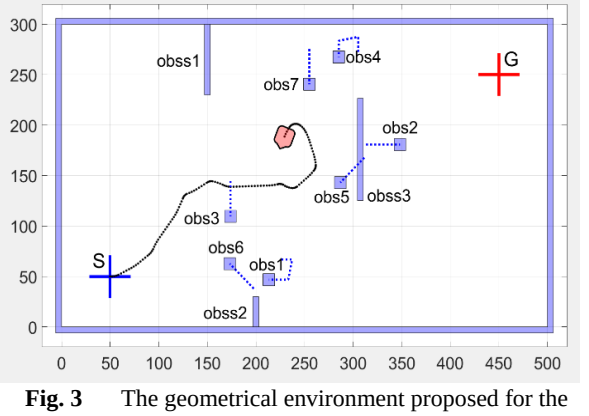

Fig. 3 The geometrical environment proposed for the training. S: start position, G: goal position, obss1, obss2, obss3: static obstacles. obs1, obs2,…, ob7: dynamic obstacles.

Also, this platform contains the definition of the state space, action space, and reward function. Finally, the platform enables the animation of the robot's motion, obstacles motion, and the development of the training process. So, one of the main goals of this platform is to generate the data needed for the training process and to test the trained robot. Figure 1 shows the proposed simulation environment for training which contains three static obstacles and seven moving ones.

The classical method to determine good values of the training parameters is to try a random group of values until we accidentally reach acceptable results. RL has too many parameters to adjust during the training process like: the learning rate for the neural network, number of layers, number of neurons in each hidden layer, mini-batch size, regularization parameter, dropout parameter, replay memory size, discount rate γ, number of maximum episodes, number of maximum steps per episode, and many other parameters and with our suggested definition of the reward, other parameters have been added so this will necessities a large number of training processes so we suggest to design an experiment from the beginning in order to save time.

Knowing that every single complete training process takes between 12 to 30 continuous hours; the 2^k factorial design came to mind. The goal of this design is to determine the most effective parameters of the reward function defined in "Eq. (1)". But first, a rough training operation is conducted to determine a rough domain for each value of the parameters a_i at which the training process has been converged. The next domain values are found:

$a_1 \in [0.01,0.5]$, $a_2 \in [1,20]$, $a_3 \in [0.01,0.5]$, $a_4 \in [1,2]$, $a_5 \in [0.1,2]$.

In the definition of our reward function, there are 5 parameters to determine and each parameter has 2 values then, the total number of experiments needed is $2^5 = 32$. Therefore, a table that includes all possible combinations of the reward parameters is prepared (Table 1). After each training process, a test process is executed. The test environment is different from the training environment. Figure 2 shows the test environment used to evaluate the trained agent.

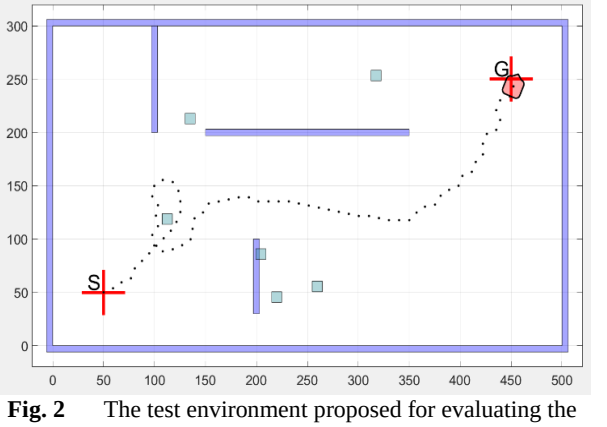

Fig. 2 The test environment proposed for evaluating the success rate after each training process.

This environment contains three static obstacles and six moving ones. Dimensions and positions of obstacles in the test environment are different from those in the

training environment. The trained agent is tested and the test is repeated three independent times. Each time, the robot has to conduct the test one thousand times, and in the end, the percentage of the robot's success in reaching the target, which is called the "Success rate" is calculated. The results are shown in "Table 1". The last three columns contain the values of the success rate for each experiment conducted.

Table 1 The success rate obtained for all the combinations of the reward parameters

trial	a_1	a_2	a_3	a_4	a_5	Success rate1 %	Success rate2 %	Success rate3 %
1	0.01	1	0.01	1	0.1	45.1	44	43.8
2	0.5	1	0.01	1	0.1	43.8	45	44.4
3	0.01	20	0.01	1	0.1	45	44.9	45
4	0.5	20	0.01	1	0.1	44.8	43.5	45.4
5	0.01	1	0.5	1	0.1	55.7	56.9	55.8
6	0.5	1	0.5	1	0.1	57.1	57.2	56.5
7	0.01	20	0.5	1	0.1	56.4	57.5	56.3
8	0.5	20	0.5	1	0.1	56.9	57	55.7
9	0.01	1	0.01	2	0.1	28.3	28.4	27.6
10	0.5	1	0.01	2	0.1	28.2	29	28.3
11	0.01	20	0.01	2	0.1	29.3	29.4	29.6
12	0.5	20	0.01	2	0.1	29.3	29.9	29.2
13	0.01	1	0.5	2	0.1	39.8	40.4	39.2
14	0.5	1	0.5	2	0.1	39.4	40.3	40.1
15	0.01	20	0.5	2	0.1	40.2	40.5	40.9
16	0.5	20	0.5	2	0.1	40.6	40.8	40.6
17	0.01	1	0.01	1	2	82.5	82.8	82.6
18	0.5	1	0.01	1	2	82.4	82.5	82.8
19	0.01	20	0.01	1	2	82.8	82	82.7
20	0.5	20	0.01	1	2	82.2	83	83.1
21	0.01	1	0.5	1	2	94.4	95.2	94.6
22	0.5	1	0.5	1	2	94	93.8	95.2
23	0.01	20	0.5	1	2	94.8	94.9	95.2
24	0.5	20	0.5	1	2	94	95.1	95.3
25	0.01	1	0.01	2	2	65.3	66.2	66
26	0.5	1	0.01	2	2	66	66.1	65.5
27	0.01	20	0.01	2	2	65.4	64.9	65.3
28	0.5	20	0.01	2	2	66	66	65.2
29	0.01	1	0.5	2	2	78.1	78.7	77.8
30	0.5	1	0.5	2	2	78.3	78.5	77.6
31	0.01	20	0.5	2	2	78.2	78.4	78.3
32	0.5	20	0.5	2	2	78.1	78.5	77.9

4 DETERMINATIONS OF REWARD PARAMETERS BY DESIGN OF EXPERIMENT

After the data was prepared, analysis was done with Minitab application and the following results were obtained. First, the normal distribution of effects ("Fig. 1") shows the effective factors on the success rate. The factors that are far from the line that represents the normal distribution are the most effective factors. Generally, the farther the factor from the line, the bigger the effect that it has. So, the most effective coefficients on the success rate are as follows, starting with the most effective ones:

1. Coefficient related to the distance change to obstacles, a_4.
2. Coefficient related to the distance to obstacles, a_3.
3. Coefficient related to the distance to the target, a_1.

Validation of the previous results is done through the observation of the residuals graphs ("Fig. 3") from which we can depict the following:
Figures 4a and b show the normal probability plot and the histogram of the residuals. It shows clearly that the residuals follow a Gaussian distribution. In "Fig. 4c and d", no particular pattern is followed by the residuals and it can be stated that these values show randomness, which assures the validation of the obtained results.
The effect of the five coefficients on the success rate is depicted independently in "Fig. 5 and Fig. 6". It shows that the coefficients related to the distance change of the target a_2 and the number of steps a_5 have negligible effect on the success rate. Whereas the remaining coefficients a_1, a_3, a_4 have a remarkable effect on the success rate as depicted previously in "Fig. 3".

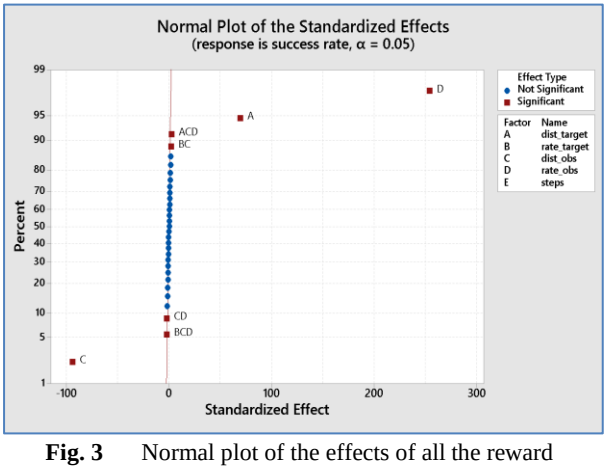

Fig. 3 Normal plot of the effects of all the reward coefficients and their interactions.

Since a_2, a_5 are not very effective, their values have been taken in the middle of their ranges. Figures 5 and 6 show an increasing success rate with increasing values of the parameters a_1, a_4 and with decreasing values of a_3 , so, a_1, a_4 have been taken to their highest limits whereas a_3 has been considered in its lower limit. The following values of all the parameters, that achieve a high success rate which is 98.2% are considered:

$a_1 = 0.5$, $a_2 = 10$, $a_3 = 0.01$, $a_4 = 2$, $a_5 = 1$

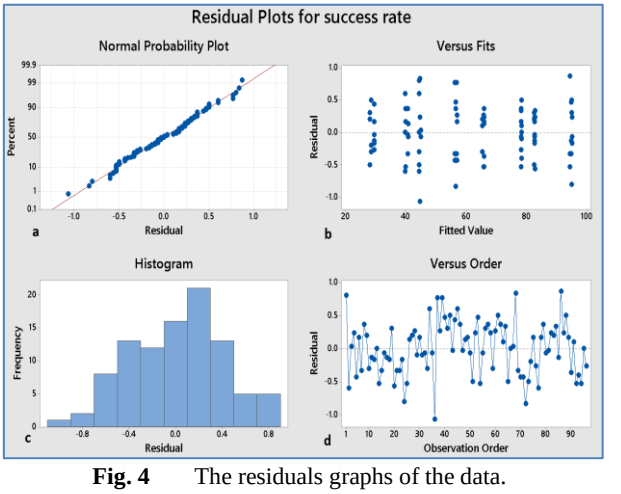

Fig. 4 The residuals graphs of the data.

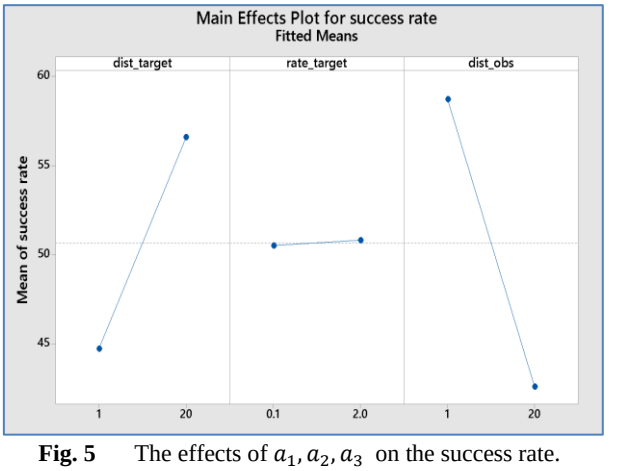

Fig. 5 The effects of a_1, a_2, a_3 on the success rate.

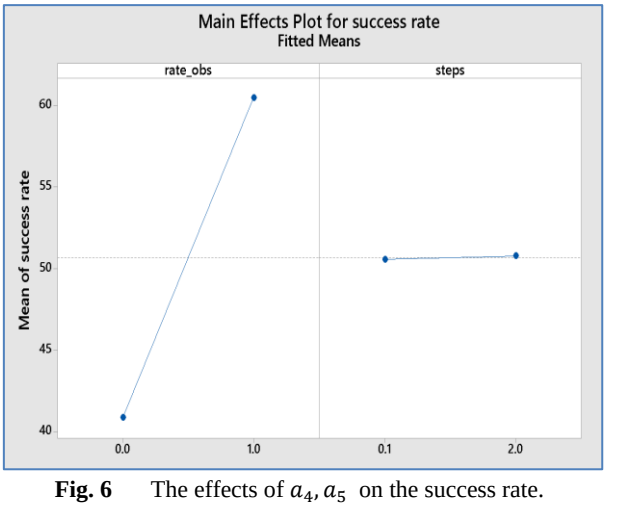

Fig. 6 The effects of a_4, a_5 on the success rate.

5 PATH PLANNING RESULTS

This section contains the tests of the trained agent with the resulting values of reward parameters. This test is done in totally new environments. Simulation tests and also real tests on real robots are done.

The environment consists of a group of obstacles like barriers forming a kind of maze between the start and the goal points, and then a few adjustments are made to get different scenarios based on the robot's behavior in order to assure the robustness of the proposed method. A successful trial is considered when the robot can avoid obstacles without collision and reach the goal point within a limited time.

5.1 Test Environment (E1)

The basic scenario (E1_1) in this environment consists of 10 obstacles in addition to the four external walls as shown in "Fig. 7a". The start point and the goal point are the same as the training environment: S(50, 50), G(450, 250). Applying the proposed path planning method, the robot takes the trajectory shown in "Fig. 7a" to reach the goal successfully without colliding with any obstacles.

Some changes are made to the first scenario which is, to lengthen obs2 in a way that closes the whole passage through which the robot has passed previously and after that reapply the test and observe the robot's performance ("Fig. 7b"). In this scenario, we notice that the robot has followed the same old path, but when it reaches the closed way, it turns and takes another path that leads to the goal.

To make it more complex for the robot, the previous way that represents the path executed by the robot is also closed by lengthening obstacle 11, and the experiment is performed again as shown in scenario E1-3. In this case, the robot tries to follow the first and second succeeding paths until it reaches a closed way and eventually, the robot could find a successful path to the goal point.

The final scenario in this environment E1-4 is achieved by changing the goal point to another point G(150, 200) which is in this case more difficult to reach as shown in scenario E1-4. It is noticed that the robot takes a new path after turning around the goal from the closed side until it successfully reaches the new goal. All these scenarios are depicted in online-resource01.

5.2. Test Environments (E2)

To assure the robustness and the power of the trained agent, different scenarios or mazes are tested, the main changes in these tests are the positions and lengths of the obstacles, and consequently, different shapes of the environments are formed. The start and the goal points have been also changed. As we can see in "Fig. 8", with all its subfigures, all the trials were successful and all four scenarios are depicted in online-resource02.

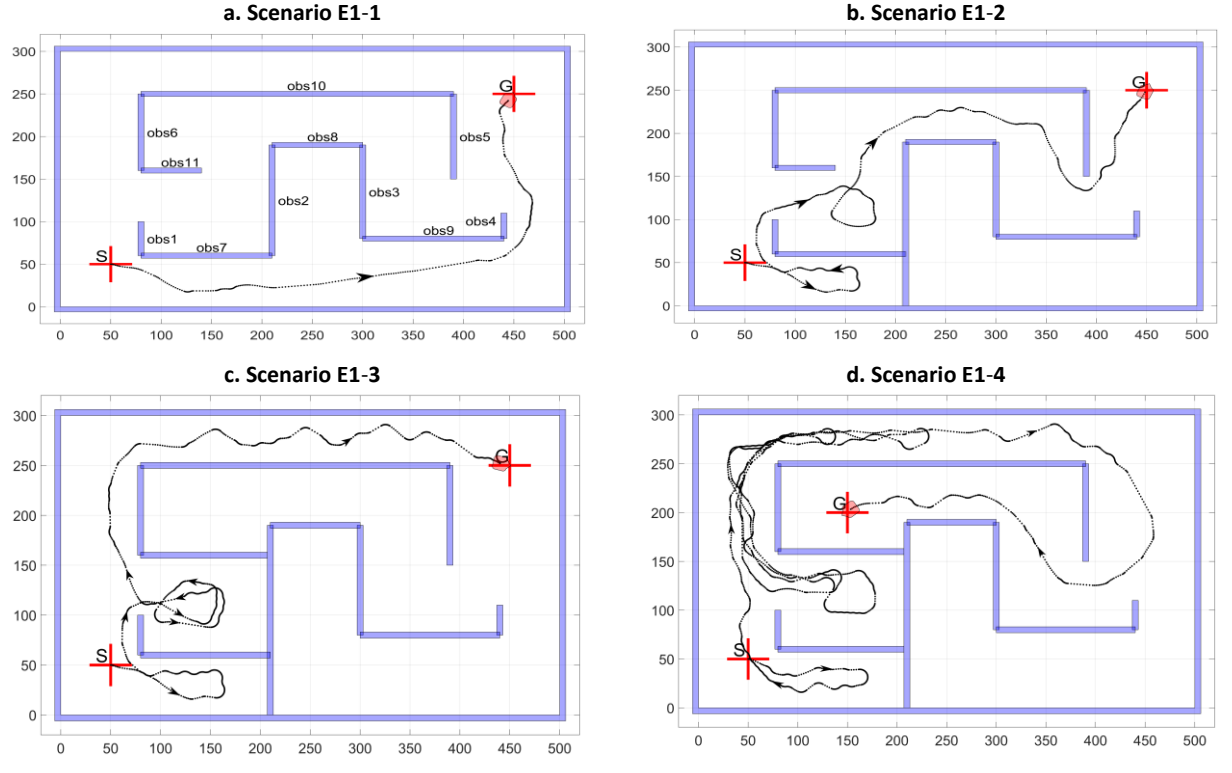

Fig. 7 Solving path planning for different scenarios in the test environment (E1).

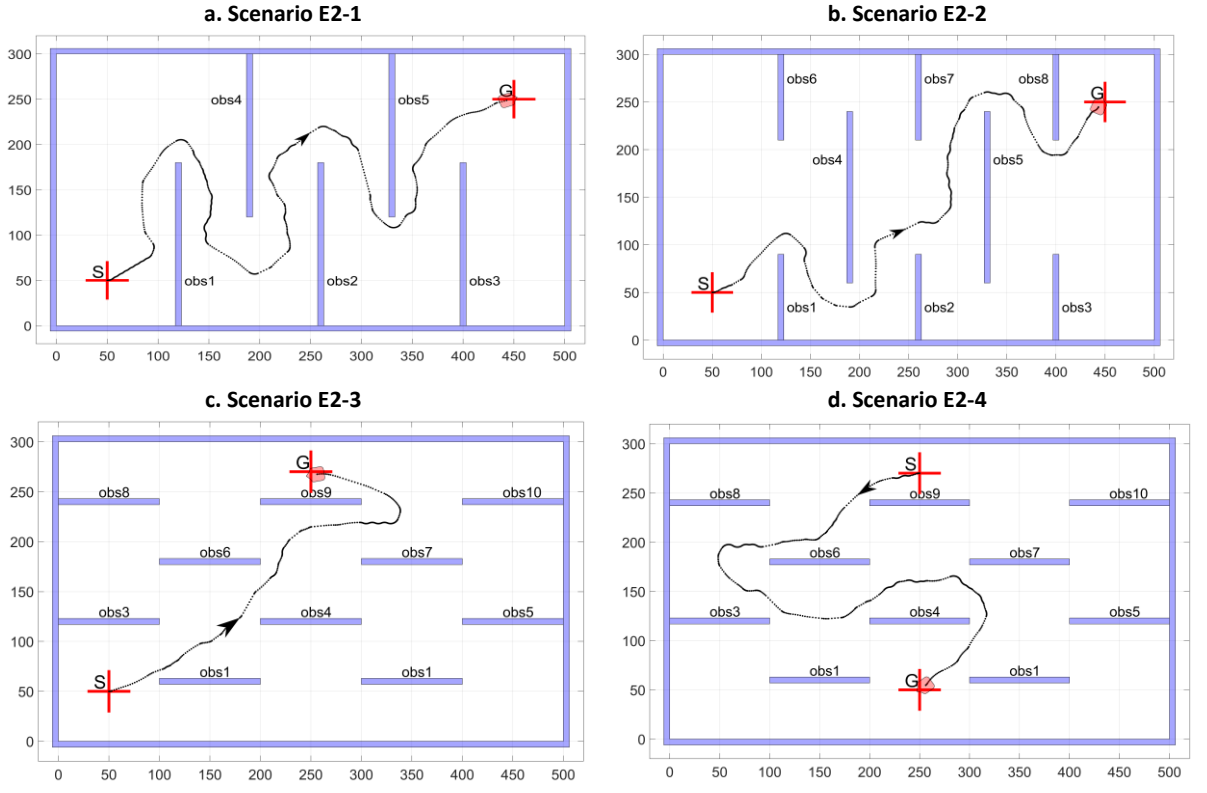

Fig. 8 Solving path planning for different scenarios and different start and goal points in the test environment (E2).

5.3. Test in Real Environment

Real experiments that apply the new approach are carried out using the TurtleBot3 Burger robot shown in "Fig. 9". The TurtleBot3 Burger is a small, programmable, ROS-based (Robot Operating System) mobile robot for use in education, research, and product prototyping. It is a Two-wheeled differential drive type platform.

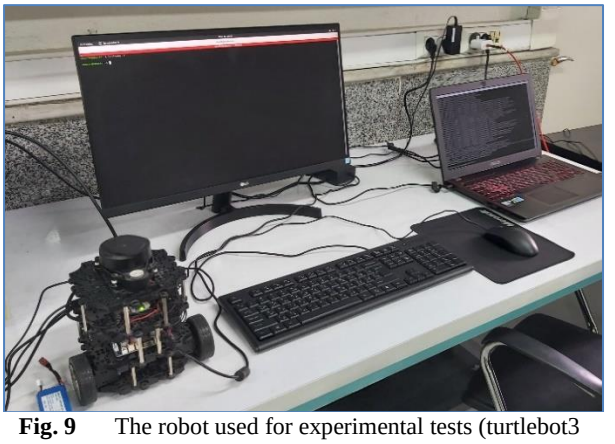

Fig. 9 The robot used for experimental tests (turtlebot3 burger), and the remote laptop used to control the robot.

The TurtleBot3 Burger is equipped with two servo motors, an OpenCR ARM Cortex-M7 control board, and a Raspberry Pi3 embedded computer. In addition to that it includes a gyroscope, accelerometer, 3-axis magnetometer, and 360 deg LiDAR.

The trained neural network with the obtained parameters of the reward has been fed up to TurtleBot3 Burger robot through a ROS2 code. Then, experiments were done to evaluate the proposed approach and to show its ability to be executed on real robots. The test environments shown in "Fig. 10" have a dimension of (250 × 200) cm. The test is done in a completely new environment in which the robot can successfully move from the start point and reach the goal point. The path is shown completely in online-resource3.

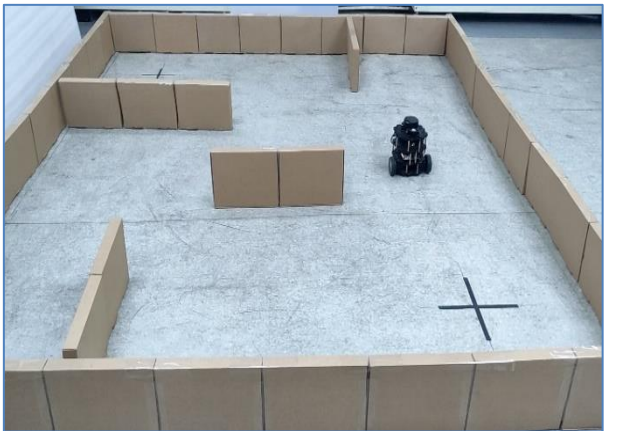

Fig. 10 Path planning test in the real environment.

6 CONCLUSIONS

A new reward function is defined to solve the path-planning problem of a mobile robot working in an unknown dynamic environment. This reward consists of five weighted parts. The coefficients of this reward definition had to be determined and optimized to achieve the most path-planning successful algorithm. Because the training process takes a very long time, a DoE approach is adopted to decrease the number of training operations. This statistical study leads to determining the most effective coefficients of the reward and determining their values. These coefficients are the ones related to the distance and the distance change to the obstacles. Finally, experimental tests of path planning were conducted to prove the efficiency of the trained agent with the obtained parameters and the results show successful training values.

REFERENCES

[1] Zhou, C., Huang, B., and Fränti, P., A Review of Motion Planning Algorithms for Intelligent Robots, Journal of Intelligent Manufacturing, Vol. 33, No. 2, 2022, pp. 387-424, 2022/02/01 2022.

[2] Patle, B., Pandey, A., Parhi, D., and Jagadeesh, A., A Review: on Path Planning Strategies for Navigation of Mobile Robot, Defence Technology, 2019.

[3] Li, Q. L., Song, Y., and Hou, Z. G., Neural Network Based Fastslam for Autonomous Robots in Unknown Environments, Neurocomputing, Vol. 165, 2015, pp. 99-110.

[4] Hart, F., Okhrin, O., Enhanced Method for Reinforcement Learning Based Dynamic Obstacle Avoidance by Assessment of Collision Risk, Neurocomputing, Vol. 568, 2024, pp. 127097.

[5] Lamini, C., Benhlima, S., and Elbekri, A., Genetic Algorithm Based Approach for Autonomous Mobile Robot Path Planning, Procedia Computer Science, Vol. 127, 2018, pp. 180-189.

[6] Abiyev, R., Ibrahim, D., and Erin, B., Navigation of Mobile Robots in The Presence of Obstacles, Advances in Engineering Software, Vol. 41, No. 10-11, 2010, pp. 1179-1186.

[7] Mohanty, P. K., Parhi, D. R., Optimal Path Planning for a Mobile Robot Using Cuckoo Search Algorithm, Journal of Experimental & Theoretical Artificial Intelligence, Vol. 28, No. 1-2, 2016, pp. 35-52.

[8] Cebollada, S., Payá, L., Flores, M., Peidró, A., and Reinoso, O., A State-of-The-Art Review on Mobile Robotics Tasks Using Artificial Intelligence and Visual Data, Expert Systems with Applications, Vol. 167, 2021, pp. 114195.

[9] Bailey, R., Reiss, J., Design and Analysis of Experiments Testing for Biodiversity Effects in Ecology, Journal of Statistical Planning and Inference, Vol. 144, 2014, pp. 69-80.

[10] Montgomery, D. C., Design and Analysis of Experiments, John Wiley & Sons, 2017.

[11] Chen, S., Wang, D., Zuo, A., Chen, Z., Li, W., and Zan, J., Vehicle Ride Comfort Analysis and Optimization Using Design of Experiment, in 2010 Second International Conference on Intelligent Human-Machine Systems and Cybernetics, Vol. 1, 2010, pp. 14-18, IEEE.

[12] Hussain, M., Gu, J., Engel, R., and Shortt, D., Designed Experiment to Find the Optimal Combination of The Factors for The Coordinate Measuring Machine (CMM) to Measure Cylindricity of Engine Cylinder Bore, in 2015 International Conference on Industrial Engineering and Operations Management (IEOM), 2015, pp. 1-8, IEEE.

[13] Zou, G., Xu, J., and Wu, C., Evaluation of Factors that Affect Rutting Resistance of Asphalt Mixes by Orthogonal Experiment Design, International Journal of Pavement Research and Technology, Vol. 10, No. 3, 2017, pp. 282-288.

[14] Hu, Q., Liu, Y., Zhang, T., Geng, S., and Wang, F., Modeling the Corrosion Behavior of Ni-Cr-Mo-V High Strength Steel in the Simulated Deep Sea Environments Using Design of Experiment and Artificial Neural Network, Journal of Materials Science & Technology, Vol. 35, No. 1, 2019, pp. 168-175.

[15] Dufreneix, S., and et al., Design of Experiments in Medical Physics: Application to the AAA Beam Model Validation, Physica Medica, Vol. 41, 2017, pp. 26-32.

[16] Mondragón, J. E., García, J. A. J., Flores, J. M. M., López, A. V., and Vázquez, S. T., Experiments Simulation and Design to Set Traffic Lights' Operation Rules, Transport policy, Vol. 67, 2018, pp. 2-12.

[17] Lv, S., Niu, Z., Cui, Q., He, Z., and Wang, G., Reliability Improvement through Designed Experiments with Random Effects, Computers & Industrial Engineering, Vol. 112, 2017, pp. 231-237.

[18] Qi, H., Osterman, M., and Pecht, M., Design of Experiments for Board-Level Solder Joint Reliability of PBGA Package Under Various Manufacturing and Multiple Environmental Loading Conditions, IEEE Transactions on Electronics Packaging Manufacturing, Vol. 32, No. 1, 2009, pp. 32-40.

[19] Nowzari, R., Mirzaei, N., and Aldabbagh, L., Finding the Best Configuration for a Solar Air Heater by Design and Analysis of Experiment, Energy Conversion and Management, Vol. 100, 2015, pp. 131-137.

[20] Vieira, L. W., et al., Methodology for Ranking Controllable Parameters to Enhance Operation of a Steam Generator with a Combined Artificial Neural Network and Design of Experiments approach, Energy and AI, Vol. 3, 2021, pp. 100040.

[21] Saidi, M., Yousefi, M., Minbashi, M., and Ameri, F. A., Catalytic Upgrading of 4-Methylaniosle as a

Representative of Lignin-Derived Pyrolysis Bio-Oil: Process Evaluation and Optimization Via Coupled Application of Design of Experiment and Artificial Neural Networks, International Journal of Hydrogen Energy, Vol. 46, No. 12, 2021, pp. 8411-8430.

[22] Zhou, Y., Van Kampen, E. J., and Chu, Q., Hybrid Hierarchical Reinforcement Learning for Online Guidance and Navigation with Partial Observability, Neurocomputing, Vol. 331, 2019, pp. 443-457.

[23] Duguleana, M., Mogan, G., Neural Networks Based Reinforcement Learning for Mobile Robots Obstacle Avoidance, Expert Systems with Applications, Vol. 62, 2016, pp. 104-115.

[24] Jaradat, M. A. K., Al-Rousan, M., and Quadan, L., Reinforcement Based Mobile Robot Navigation in Dynamic Environment, Robotics and Computer-Integrated Manufacturing, Vol. 27, No. 1, 2011, pp. 135-149.

[25] Xia, C., El Kamel, A., Neural Inverse Reinforcement Learning in Autonomous Navigation, Robotics and Autonomous Systems, Vol. 84, 2016, pp. 1-14.

[26] Smart, W. D., Kaelbling, L. P., Effective Reinforcement Learning for Mobile Robots, in Proceedings 2002 IEEE International Conference on Robotics and Automation (Cat. No. 02CH37292), Vol. 4, 2002, pp. 3404-3410, IEEE.

[27] Wei, M., Wang, S., Zheng, J., and Chen, D., UGV Navigation Optimization Aided by Reinforcement Learning-Based Path Tracking, IEEE Access, Vol. 6, 2018, pp. 57814-57825.

Int. J. Advanced Design and Manufacturing Technology, 2024, Vol. 17, No. 3, pp. 49-64

DOI: ***ISSN: 2252-0406*** ***https://admt.isfahan.iau.ir***

Friction-Adaptive Integrated Position Control for Vehicles on Curved Paths

Hadi Sazgar *
Department of Mechanical Engineering,
Iranian Research Organization for Science and Technology (IROST), Iran
E-mail: sazgar@irost.ir
*Corresponding author

Ali Keymasi-Khalaji
Department of Mechanical Engineering, Faculty of Engineering,
Kharazmi University, Iran
E-mail: keymasi@khu.ac.ir

Received: 6 January 2024, Revised: 12 June 2024, Accepted: 4 August 2024

Abstract: In critical manoeuvres where the maximum tire-road friction capacity is used, the vehicle's dynamic behaviour is highly nonlinear, and there are strong couplings between longitudinal and lateral dynamics. If the tire-road friction conditions change suddenly during these manoeuvres, the vehicle control will be very complicated. The innovation of this research is a control algorithm to manage vehicles on a curved path with sudden tire-road friction change. The main advantage of the proposed controller is that it is robust to the change of the friction coefficient and other unmodeled uncertainties and ensures vehicle stability with low computational volume. The evaluation of the proposed adaptive controller has been done using the full vehicle model in CarSim software and by defining three different manoeuvres, moving at a constant speed on a curved road, lane-change, and lane-change with braking. Also, in the obtained results, the noise of the yaw speed signals and longitudinal and lateral accelerations are considered. The estimation of the longitudinal and lateral velocities is also done using these data. The obtained results showed that the proposed integrated control can manage the highly nonlinear dynamics of the vehicle in the existence of a sudden and significant change in the friction coefficient.

Keywords: Integrated Longitudinal and Lateral Control, Kinetic Control, Kinematic Control, Nonlinear Tire, Seven Degrees of Freedom Dynamic Model, Tire-Road Friction Estimation,

Biographical notes: Hadi Sazgar earned his BSc degree from Shahid Bahonar University of Kerman (SBUK), Kerman, Iran, in 2007, followed by his MSc and PhD in Mechanical Engineering from K. N. Toosi University of Technology (KNTU), Tehran, in 2009 and 2019, respectively. He is an assistant professor in the Mechanical Engineering Department at the Iranian Research Organization for Science and Technology (IROST) in Tehran. His research interests focus on the modeling and control of mechanical systems, vehicle dynamic control, and advanced driver assistance systems (ADAS). **Ali Keymasi-Khalaji** received his BSc from Iran University of Science and Technology (IUST), Tehran, Iran, in 2007, and his MSc and PhD in Mechanical Engineering from K. N. Toosi University of Technology (KNTU), Tehran, in 2009 and 2014 respectively. He has been an associate professor with the Mechanical Engineering Department at Kharazmi University (KHU) in Tehran since 2015. His research interests include modeling and control of mechanical systems, nonlinear control, and adaptive and robust control with applications to mobile robotic systems and mechatronics.

Research paper

1 INTRODUCTION

Autonomous driving started in the 1980s [1-2] and has developed and progressed significantly over the past few decades [3]. Automatic driving can save time and reduce air pollution by reducing traffic. In addition, self-driving vehicles can significantly increase the comfort and safety. Based on accident statistics and the proportion of accidents caused by human error, there is a growing need for self-driving cars. The World Health Organization states that more than 1.35 million people die, and 20 to 50 million people are injured due to annual accidents worldwide. Economic studies also show that the costs caused by accidents are more than 3% of the gross domestic product of the countries [4]. A study by the National Highway Traffic Safety Administration (NHTSA) in 2015 shows that human error was effective in about 94 percent of all car accidents [5].

The self-driving car has different parts, one of the most important of which is the control algorithm. The control section must perform the path tracking with the desired accuracy and also ensure vehicle stability. In a critical maneuver in which the longitudinal and lateral movements are performed simultaneously, the tire is in its saturated range. During the manoeuvre, the tire-road friction conditions also change. Due to uncertainties and very strong couplings between longitudinal and lateral dynamics in several levels of dynamics, kinematics, and tire forces, the problem of path following and maintaining the stability of the vehicle in a critical manoeuvre will be very challenging and complex.

Literature review: So far, various control approaches have been proposed to solve this problem. One of the important manoeuvres in which longitudinal and lateral movements are performed at the same time is the lane change maneuverer. In [6-7], a review of the methods presented in the field of lane change control has been done. Depending on the desired manoeuvre, different controllers can be used. For simple manoeuvres where tire slip is negligible, a kinematic model can be used, and a controller can be designed for that [8-10]. Assuming that the slip of the tires is small, the relationship between force and slip is linear and it will be logical to use the linear dynamic model. In some references, the control algorithm has been studied based on a linear dynamic model [11-18]. One of the very important manoeuvres that play a role in reducing accidents is the collision avoidance manoeuvre. Numerous researchers have studied the problem of longitudinal and lateral integrated control with an emphasis on collision avoidance [19-23]. Model predictive control has been used many times in various areas of vehicle control due to its high capability in managing multi-objective constrained systems with uncertainty [24-26]. In some cases, predictive control has been used along with other methods. In [27], the direct Lyapunov approach has been used for longitudinal velocity control and nonlinear predictive control (NMPC) for lateral control. Despite having many capabilities, predictive control also brings challenges. By growing the model order, nonlinear terms, and constraints, the computational cost increases, and the possibility of getting stuck in the local minimum while doing the optimization problem increases.

In [28], a comprehensive approach that combines planning and control mechanisms to enhance the quality of trajectories produced by intelligent vehicles is introduced. The trajectory planning component is engineered using the principles of the Iterative Linear Quadratic Regulator (ILQR), which incorporates the vehicle's nonlinear dynamics to optimize trajectory planning. In [29], a combined H∞ control approach is designed to enhance both the path-following capabilities and the lateral stability of autonomous in-wheel-motor-driven electric vehicles (AIEVs) is presented.

Motivation and innovation: The prior surveys show that valuable research has been conducted in this field. However, the problem of integrated longitudinal and lateral control of the vehicle in critical manoeuvres still needs more investigation. The primary objective of this work is to develop an adaptive control algorithm capable of providing integrated longitudinal and lateral control for highly nonlinear vehicle dynamics, while being robust to sudden changes in the friction coefficient and other uncertainties. A key goal is also to enable the control system to effectively follow curved paths, in addition to managing linear manoeuvres, by separating the control architecture. These objectives are motivated by the need to enhance vehicle safety and performance in challenging driving conditions where the available tire-road friction can vary unexpectedly. In [30-31], the motion control and integrated longitudinal and lateral control in the critical lane change manoeuvre on the highways have been done. To manage the variations of tire and road friction conditions, an adaptive control algorithm is proposed in [32]. This control algorithm uses the sliding mode approach, and by considering the nonlinear tire dynamics, it updates the tire forces in the control law by changing the friction conditions of the tire and the road. Despite having many advantages such as low computational cost, stability, and high tracking accuracy, this controller also has a fundamental limitation.

This control algorithm is only used for lane change manoeuvres on the highways, where the lateral position variation is small compared to the longitudinal position. This article proposes a new control algorithm for critical manoeuvres to overcome this limitation. This algorithm can be used for the integrated longitudinal and lateral dynamics control of the vehicle on all roads (straight and curved roads). The accuracy of trajectory tracking of this algorithm is very high, and it also guarantees vehicle stability. This controller also can adapt to variations in

the tire-road friction conditions. This algorithm is robust to unmodeled uncertainties and parameter changes, and it will be helpful for manoeuvres where the vehicle dynamics are highly nonlinear and the tire capacity is in the saturated range. The details related to the design of the integrated controller, as well as the estimation algorithm of tire forces and friction coefficient, will be presented in sections 3 and 4, respectively.

2 VEHICLE DYNAMIC MODEL

In high-speed manoeuvres, it is possible to analyse the real behaviour of the vehicle only with a nonlinear dynamic model with many degrees of freedom. On the other hand, due to unmodeled uncertainties and the unknown value of the parameters, it is practically impossible to design a model-based controller based on complex dynamic models with high degrees of freedom. Considering these considerations, in this research, 7 degrees of freedom model, including three degrees for movements in the yaw plane (x, y and ψ) and four degrees of freedom for four wheels, are used. The overview of this model is shown in "Fig. 1". This model considers longitudinal and lateral load transfer caused by longitudinal and lateral accelerations. The simulations performed on a complete vehicle model show that the design of the controller based on the 7-degree-of-freedom model $(x, y, \psi, \omega_{f,l}, \omega_{f,r}, \omega_{r,r}, \omega_{r,l})$ was practical and appropriate (Section 5).

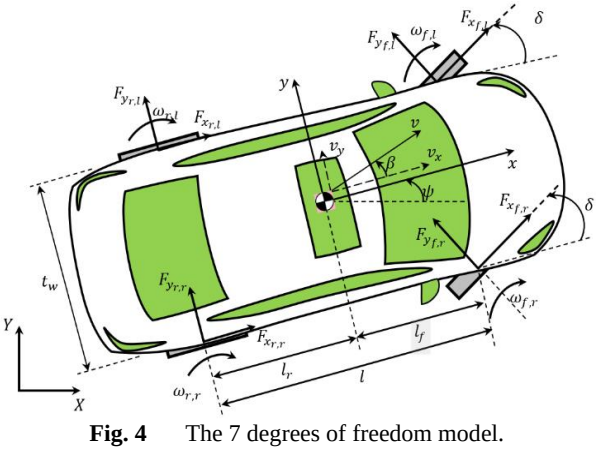

Fig. 4 The 7 degrees of freedom model.

In "Fig. 1", $X-Y$ are the inertial coordinate axes, and x-y are the local coordinate axes connected to the centre of mass (CG). Subscripts f and r refer to the front axle and rear axle of the vehicle. Also, the pairs (f,l), (f,r), (r,r), and (r,l)refer to the left front, right front, right rear, and left rear tires, respectively. F_x and F_y represent the longitudinal and lateral forces of the tire, respectively. The symbol ω also indicates the rotation around the wheel spinning axis. The longitudinal and lateral speeds at the CG are measured in local coordinates and are introduced by variables v, v_x and v_y, respectively. δ, ψ, and β stand for the front wheel steering angle, vehicle yaw angle, and vehicle side-slip angle, respectively. The description and values of dynamic model parameters are presented in "Table 1". The values of this table are extracted from D-Class Sedan vehicle in the CarSim software.

In the following, the details of other parts of the dynamic model are stated.

Table 1 Vehicle dynamic model parameters [30]

Parameter	Value	Unit	Description
m	1530	kg	The total mass of the vehicle
I_z	2315	kgm^2	Vehicle yaw moment of inertia
l_f	1.11	m	Front axle CG distance
l_r	1.67	m	Rear-axle CG distance
t_w	1.55	m	Track width
h_{CG}	0.52	m	Height of CG
C_d	0.3	---	Aerodynamic drag coefficient
k_b	700	(N. m) /MPa	Braking gain
τ_b	0.06	---	Brake actuator time constant
τ_{bd}	31	msec	Brake delay
η_d	0.85	---	Driveline efficiency
k_{diff}	4.1	---	Driveline gain
r_w	0.325	m	Effective wheel radius
I_w	0.9	$\mathrm{kg.m}^2$	Wheel's moment of inertia
f_r	0.015	---	Rolling resistance coefficient

2.1. Vehicle Motion Equations [33]

$$\begin{aligned}(\dot{v}_x - v_y\dot{\psi}) = \Big[&\left(F_{x_{f,l}} + F_{x_{f,r}}\right)\cos\delta \\ &- \left(F_{y_{f,l}} + F_{y_{f,r}}\right)\sin\delta \\ &+ \left(F_{x_{r,l}} + F_{x_{r,r}}\right) - F_{aero}\Big]\end{aligned} \tag{1}$$

$$\begin{aligned}m(\dot{v}_y + v_x\dot{\psi}) = \Big[&\left(F_{x_{f,l}} + F_{x_{f,r}}\right)\sin\delta \\ &+ \left(F_{y_{f,l}} + F_{y_{f,r}}\right)\cos\delta \\ &+ \left(F_{y_{r,l}} + F_{y_{r,r}}\right)\Big]\end{aligned} \tag{2}$$

$$\begin{aligned}I_z\ddot{\psi} = l_f\Big[&\left(F_{x_{f,l}} + F_{x_{f,r}}\right)\sin\delta + \left(F_{y_{f,l}} + F_{y_{f,r}}\right)\cos\delta\Big] \\ &- l_r\left(F_{y_{r,l}} + F_{y_{r,r}}\right)\end{aligned} \tag{3}$$

Where, $\dot{\psi}$ and $\ddot{\psi}$ are the rotational velocity and

acceleration of the vehicle, respectively. F_{aero} also represents the aerodynamic force applied to the front surface of the vehicle defined by "Eq. (4)", [33]:

$$F_{aero} = \frac{1}{2}\rho C_d A_F (v_x + v_{wind})^2 \quad (4)$$

Where, ρ is the air density and v_{wind} is the wind speed. A_F also represents the effective front surface of the vehicle and is equal to $1.6 + 0.00056(m - 765)$, [33].

2.2. Tire Model

For the behaviour of the tire model to be close to the real behaviour, complex and accurate models should be used [33-35]. Accurate models have many parameters that must be identified. Identifying these parameters will be a major challenge considering the variations in tire and road conditions. Even if these parameters are identified, due to the accumulation of dynamic modelling errors and identification errors, the resulting tire and road friction model may significantly differ from the actual friction behaviour. In addition, the selected model for controlling the base model should be as simple as possible. Fortunately, if robust control approaches are used, it can be ensured that the unmodeled uncertainties of the tire will be well covered. Considering these considerations, based on the friction circle, a version of Pacejka's tire model, which has been used for control applications in this field [36-37], will be used [38]. Of course, for integrated control with friction estimation, this tire model will be used with modifications that will be explained in section 4.

$$F_{\gamma_{\tau,\varepsilon}} = \frac{\sigma_{\kappa_{\tau,\varepsilon}}}{\sigma_{\tau,\varepsilon}} \mu_{\tau,\varepsilon} F_{z_{\tau,\varepsilon}}, \quad \kappa \in \{x, y\}, \quad \tau \in \{f, r\}, \quad \varepsilon \in \{l, r\} \quad (5)$$

In this Equation, $F_{z_{\tau,\varepsilon}}$ represents the vertical load of each tire and $\mu_{\gamma_{\tau,\varepsilon}}$ stands for the longitudinal or lateral tire-road friction coefficient. $\sigma_{\tau,\varepsilon}$ also represents the total tire slip, which is a function of the longitudinal slip ($\sigma_{x_{\tau,\varepsilon}}$) and lateral slip ($\sigma_{y_{\tau,\varepsilon}}$) of the tire ($\sigma_{\tau,\varepsilon} = \sqrt{\left(\sigma_{x_{\tau,\varepsilon}}\right)^2 + \left(\sigma_{y_{\tau,\varepsilon}}\right)^2}$) [38]. By considering the effect of load transfer caused by longitudinal and lateral accelerations using D'Alembert's principle, the vertical force of tires can be approximated with the following relationship. It must be recognized that the effect of vehicle suspension has been ignored.

$$F_{z_{f,l}} = m\left[\frac{g l_r - a_x h_{CG} - F_{aero} h_{aero}/m}{2l} - \frac{l_r}{l}\frac{h_{CG}}{t_w} a_y\right] \quad (6)$$

$$F_{z_{f,r}} = m\left[\frac{g l_r - a_x h_{CG} - F_{aero} h_{aero}/m}{2l} + \frac{l_r}{l}\frac{h_{CG}}{t_w} a_y\right] \quad (7)$$

$$F_{z_{r,l}} = m\left[\frac{g l_f + a_x h_{CG} + F_{aero} h_{aero}/m}{2l} - \frac{l_f}{l}\frac{h_{CG}}{t_w} a_y\right] \quad (8)$$

$$F_{z_{r,r}} = m\left[\frac{g l_f + a_x h_{CG} + F_{aero} h_{aero}/m}{2l} + \frac{l_f}{l}\frac{h_{CG}}{t_w} a_y\right] \quad (9)$$

2.2.1. Longitudinal Slip Ratio [38]

$$\sigma_{x_{\tau,\varepsilon}} = \frac{v_{rw_{\tau,\varepsilon}} - v_{cw_{\tau,\varepsilon}}}{\max\left(v_{rw_{\tau,\varepsilon}}, v_{cw_{\tau,\varepsilon}}\right)}, \tau \in \{f, r\}, \varepsilon \in \{l, r\} \quad (10)$$

In the above Equations, $v_{cw_{\tau,\varepsilon}}$ is the longitudinal velocity of the tire contact point with the road surface and $v_{rw_{\tau,\varepsilon}}$ is the longitudinal velocity equivalent to the rotation of the wheel [34].

2.2.2. Tire Slip Angle [33]

$$\sigma_{f,l} = \sigma_{f,r} = \delta - \arctan\left(\frac{v_y + \dot{\psi} l_f}{v_x}\right) \quad (11)$$

$$\sigma_{r,l} = \sigma_{r,r} = -\arctan\left(\frac{v_y - \dot{\psi} l_r}{v_x}\right) \quad (12)$$

2.3. Wheel Dynamics

The wheel motion Equation establishes the relationship between the longitudinal force and the traction and braking torques [33].

$$I_w \dot{\omega}_{\tau,\varepsilon} = -F_{x_{\tau,\varepsilon}} . r_w + \left(T_{d_{\tau,\varepsilon}} - T_{b_{\tau,\varepsilon}}\right) - f_r F_{z_{\tau,\varepsilon}} r_w, \quad \tau \in \{f, r\}, \quad \varepsilon \in \{l, r\} \quad (13)$$

Where, $\dot{\omega}$ is the angular acceleration of the wheel, $T_{d_{\tau,\varepsilon}}$ is the traction torque, $T_{b_{\tau,\varepsilon}}$ is the braking torque applied to the wheel.It is assumed that the torque applied to the left and right wheels of the front axle are equal to each other. This assumption is also valid for the wheels of the rear axle. It must be recognized that the traction torque is applied only to the front wheels. It is also assumed that in the braking mode, the distribution ratio of the rear-to-front braking torques is equal to γ. The parameter γ is determined using the pressure distribution valve of the hydraulic system [33]. Therefore, the torques applied to the wheels can be defined as "Eq. (14) and Eq. (15)".

$$T_{d_{f,l}} = T_{d_{f,r}} = \frac{T_d}{2}, \quad T_{d_{r,l}} = T_{d_{r,r}} = 0 \tag{14}$$

$$T_{b_{\tau,l}} = T_{b_{\tau,r}} = \frac{T_{b_\tau}}{2}, \quad \tau \in \{f, r\} \tag{15}$$

It should be noted that T_d and T_b represent the sum of traction and braking torques applied to the wheels, respectively.

2.4. Power Train Model

It can be presumed that the torque converter is completely locked in high-speed maneuvers. So, the relationship between the engine torque (T_e) and the total traction torque (T_d) can be expressed as "Eq. (16)", [33].

$$T_e = \frac{T_d}{\eta_d k_{diff} n_g} \tag{10}$$

Where, n_g is the gear transmission ratio.
Also, the throttle opening percentage is a function of the engine's net torque (T_e) and its rotation speed (ω_e). This function is available as a lookup table ($\alpha_{th} = f(\omega_e, T_e)$).

2.5. Brake Dynamics

The relationship between the brake torque and the pressure in the main cylinder (P_b) can be approximately expressed by "Eq. (17)", [39]:

$$\frac{T_b(s)}{P_b(s)} = \frac{k_b e^{-\tau_{bd} s}}{\tau_b s + 1} \tag{17}$$

3 LONGITUDINAL AND LATERAL INTEGRATED CONTROL

The proposed control method is a robust control approach that can also be used for curved roads. This controller includes two kinematic and dynamic parts. Separating the system control into two kinematic and dynamic parts makes it possible to control the system position variables. Therefore, in this way, it becomes possible to follow curved paths. The general structure of the controller is such that first, in the kinematics section, the desired longitudinal and lateral velocity is determined based on the tracking longitudinal and lateral position errors. Then, in the dynamic control, appropriate inputs are calculated to reach the desired velocities required in the kinematic control, considering the vehicle dynamics.

3.1. Kinematic Control

The desired position vector is $p_R = \begin{bmatrix} X_R \\ Y_R \end{bmatrix}$, which represents the desired longitudinal and lateral positions, respectively. Also, the vehicle position vector is defined as $p = \begin{bmatrix} X \\ Y \end{bmatrix}$ ("Fig. 2"). The error vector, e, is also expressed as the difference between the desired position vector and the vehicle position vector.

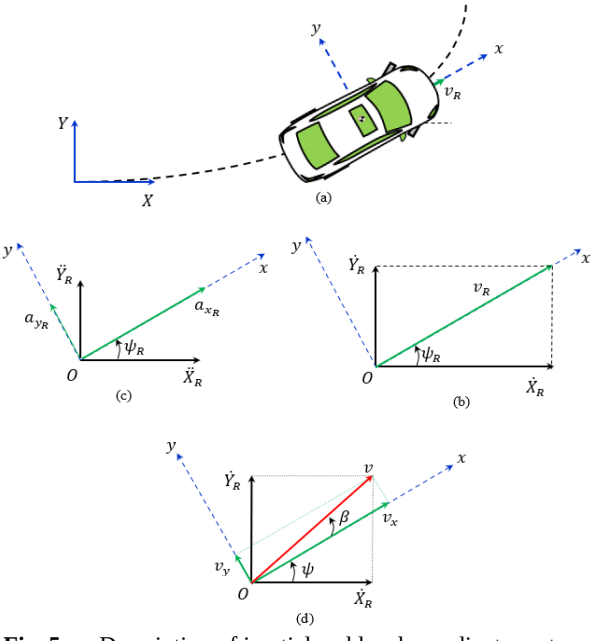

Fig. 5 Description of inertial and local coordinate system: (a): positions, (b): velocities (β=0), (c): accelerations, and (d): velocities (β≠0).

$$e = p_R - p = \begin{bmatrix} X_R - X \\ Y_R - Y \end{bmatrix}$$

The error dynamics for kinematic control is also expressed as:

$$\dot{e} + K_c e + K_{i,c} \int_0^t e \, dt = 0 \tag{18}$$

Where, K_c and $K_{i,c}$ are positive definite control gain matrixes. According to "Fig. 2" and assuming $R = \begin{bmatrix} \cos\psi & -\sin\psi \\ \sin\psi & \cos\psi \end{bmatrix}$, the velocity components in the inertial coordinates can be related to the components of the local coordinates as:

$$\begin{bmatrix} \dot{X} \\ \dot{Y} \end{bmatrix} = R \begin{bmatrix} v_x \\ v_y \end{bmatrix} \tag{19}$$

By combining "Eq. (18) and Eq. (19)", the desired velocity vector v_c can be written as:

$$v_c = \begin{bmatrix} v_{x_c} \\ v_{y_c} \end{bmatrix} = R^{-1} \left[\dot{p}_R + K_c e + K_{i,c} \int_0^t e \, dt \right] \tag{20}$$

3.2. Dynamicic Control

The goal of dynamic control is to make v_x and v_y tend to values v_{x_c} and v_{y_c} respectively. Therefore, the error of longitudinal and lateral velocities can be expressed as:

$$e_{v_x} = v_{x_c} - v_x \tag{21}$$

$$e_{v_y} = v_{y_c} - v_y \tag{22}$$

The error dynamics of longitudinal and lateral velocities can be defined as:

$$\dot{e}_{v_x} + K_{v_x} e_{v_x} + K_{i,v_x} \int_0^t e_{v_x}\, dt = 0 \tag{23}$$

$$\dot{e}_{v_y} + K_{v_y} e_{v_y i} + K_{i,v_y} \int_0^t e_{v_y}\, dt = 0 \tag{24}$$

Where K_{v_x}, K_{i,v_x}, K_{v_y} and K_{i,v_y} are positive definite control gain matrixes.

3.2.1. Longitudinal Control

Equation (23) can be used to calculate the longitudinal control input (throttle opening rate or brake cylinder pressure). By simplifying, we have:

$$\dot{v}_x = \dot{v}_{x_c} + K_{v_x} e_{v_x} + K_{i,v_x} \int_0^t e_{v_x}\, dt \tag{25}$$

On the other hand, by combining the Equation of longitudinal motion and wheel dynamics ("Eq. (1) and Eq. (13)"), $\dot{v}_x$ can be defined as:

$$\dot{v}_x = \frac{1}{m}\left[\frac{T_f - f_r r_w F_{z_f} - I_w\left(\dot{\omega}_{f,l} + \dot{\omega}_{f,r}\right)}{r_w}\cos\delta + \left(\frac{T_r - f_r r_w F_{z_r} - I_w\left(\dot{\omega}_{r,l} + \dot{\omega}_{r,r}\right)}{r_w}\right) - F_{y_f}\sin\delta - F_{aero}\right] + v_y\dot{\psi} \tag{26}$$

By setting the right side of "Eq. (25) and Eq. (26)" equal, the total torque applied to the front and rear wheels can be calculated as:

$$\begin{aligned} T_f\cos\delta + T_r = mr_w\Bigg(&\dot{v}_{x_c} + K_{v_x} e_{v_x} \\ &+ K_{i,v_x}\int_0^t e_{v_x}\, dt + v_y\dot{\psi}\Bigg) \\ &+ r_w\left(F_{y_f}\sin\delta + F_{aero}\right) \\ &+ I_w\left(\left[\dot{\omega}_{f,l} + \dot{\omega}_{f,r}\right]\cos\delta + \dot{\omega}_{r,l} + \dot{\omega}_{r,r}\right) \\ &+ r_w\left[f_r F_{z_f}\cos\delta + f_r F_{z_r}\right] \end{aligned} \tag{27}$$

The dynamics of the brake system and the power train are different, and each has its inputs. So, in the following steps, extracting the control input for each one is described separately.

3.2.1.1. Braking Mode

In braking mode, the ratio of the braking torque of the rear wheels to the front is assumed to be γ. In addition, the torque applied to the left and right wheels is the same in each of the axles. According to these assumptions and "Eq. (27)", the braking torque applied to each can be expressed by:

$$\begin{aligned} T_b = 1/(\cos\delta + \gamma)\Bigg[mr_w\Bigg(&\dot{v}_{x_c} + K_{v_x} e_{v_x} \\ &+ K_{i,v_x}\int_0^t e_{v_x}\, dt + v_y\dot{\psi}\Bigg) \\ &+ r_w\left(F_{y_f}\sin\delta + F_{aero}\right) \\ &+ I_w\left(\left[\dot{\omega}_{f,l} + \dot{\omega}_{f,r}\right]\cos\delta + \dot{\omega}_{r,l} + \dot{\omega}_{r,r}\right) \\ &+ r_w\left(f_r F_{z_f}\cos\delta + f_r F_{z_r}\right)\Bigg] \end{aligned} \tag{28}$$

By determining the total braking torque, the brake cylinder pressure can be determined using "Eq. (17)".

3.2.1.2. Traction Mode

As mentioned, torque is not applied to the rear wheels in traction mode. According to "Eq. (16) and Eq. (27)", the required engine torque can be expressed as:

$$\begin{aligned} T_b = 1/\left(\eta_d k_{diff} n_g\cos\delta\right)\Bigg[mr_w\Bigg(&\dot{v}_{x_c} + K_{v_x} e_{v_x} \\ &+ K_{i,v_x}\int_0^t e_{v_x}\, dt + v_y\dot{\psi}\Bigg) \\ &+ r_w\left(F_{y_f}\sin\delta + F_{aero}\right) \\ &+ I_w\left(\left[\dot{\omega}_{f,l} + \dot{\omega}_{f,r}\right]\cos\delta + \dot{\omega}_{r,l} + \dot{\omega}_{r,r}\right) \\ &+ r_w\left(f_r F_{z_f}\cos\delta + f_r F_{z_r}\right)\Bigg] \end{aligned} \tag{29}$$

The throttle opening percentage can be determined by determining the engine torque and the engine speed.

3.2.2. Lateral Control

First, we multiply both sides of "Eq. (2)" by l_r and add the resulting Equation with Equation (3).

$$\begin{aligned} ml_r\left(\dot{v}_y + v_x\dot{\psi}\right) + I_z\ddot{\psi} \\ = l\left[\left(F_{x_{f,l}} + F_{x_{f,r}}\right)\sin\delta + \left(F_{y_{f,l}} + F_{y_{f,r}}\right)\cos\delta\right] \end{aligned} \tag{30}$$

By combining "Eq. (5), Eq. (11), and Eq. (30)", $\dot{v}_y$ can be defined as "Eq. (31)".

$$\dot{v}_y = \frac{l}{ml_r}\Bigg[F_{x_f}\sin\delta + b\left(\delta - \arctan\left(\frac{v_y + \dot{\psi}l_f}{v_x}\right)\right) - I_z\ddot{\psi}\Bigg] - v_x\dot{\psi} \quad (31)$$

Where $b = \frac{l\cos\delta}{ml_r}\left(\frac{\mu_{f,l}}{s_{f,l}}\ F_{z_{f,l}} + \frac{\mu_{f,r}}{s_{f,r}}\ F_{z_{f,r}}\right)$. On the other hand, using "Eq. (24)", $\dot{v}_y$ can be written as:

$$\dot{v}_y = \dot{v}_{y_c} + K_{v_y}e_{v_y} + K_{i,v_y}\int_0^t e_{v_y}\,dt \quad (32)$$

By setting the right side of "Eq. (31) and Eq. (32)" equal, the steering angle δ can be determined as:

$$\delta = \frac{1}{b}\Bigg[\frac{ml_r}{l}\left(\dot{v}_{y_c} + K_{v_y}e_{v_y} + K_{i,v_y}\int_0^t e_{v_y}\,dt + v_x\dot{\psi}\right) - F_{x_f}\sin\delta_{-1} + I_z\ddot{\psi}\Bigg] + \arctan\left(\frac{v_y + \dot{\psi}l_f}{v_x}\right) \quad (33)$$

4 ONLINE ESTIMATION ALGORITHM OF TIRE FORCES AND TIRE-ROAD FRICTION COEFFICIENTS

It can be seen carefully in "Eq. (28), Eq. (29), and (33)" that the tire forces must also be known to calculate the control inputs. Since the complex dynamics of tires depend on environmental changes, tire wear, and unpredictable road conditions, the online estimation of these forces is necessary. In references [40-44], methods of identifying parameters of complex tire models, friction coefficient, and tire forces have been reviewed. Generally, past research in this field can be classified into cause-based and effect-based estimation methods. The concentration of cause-based methods is on studying and diagnosing effective factors in the tire-road interaction, and the friction coefficient is identified using specific analytical theories [43]. Effect-based techniques also use vehicle response to determine the friction coefficient [44].

In this research, according to the concept of friction circle and the use of vehicle kinematic characteristics that can be measured or estimated by sensors, tire forces, and friction coefficients are computed online with a straightforward algebraic algorithm and updated in the control law.

Since the proposed method works based on the vehicle response, it is an effect-based estimation technique. The details of the proposed method are presented below.

4.1. Calculation of The Longitudinal and Lateral Tire Forces

For simplicity, the vehicle's motion Equations are first rewritten in the following form:

$$ma_x = F_{x_f}\cos\delta - F_{y_f}\sin\delta + F_{x_r} - F_{aero} \quad (34)$$

$$ma_y = F_{x_f}\sin\delta + F_{y_f}\cos\delta + F_{y_r} \quad (35)$$

$$ma_y = F_{x_f}\sin\delta + F_{y_f}\cos\delta + F_{y_r} \quad (36)$$

Now, we multiply both sides of "Eq. (35)" by $(-l_f)$ and add both sides of the resulting Equation with Eq. (36) to obtain "Eq. (37)".

$$F_{y_r} = \frac{l_f ma_y - I_z\ddot{\psi}}{l} \quad (37)$$

Knowing a_y and $\ddot{\psi}$ then F_{y_r} can be calculated. According to "Eq. (34) and Eq. (35)", to calculate F_{y_f}, the longitudinal forces of the tires must be determined first. Besides, because the distribution of traction and braking torques are unlike, $F_{x_f}$and F_{x_r} are also different for braking and traction modes. Therefore, these two states are separated from each other in the following.

4.1.1. Traction Mode

For front-wheel drive vehicles, F_{x_f} can be computed from the wheel dynamic "Eq. (13)".

$$F_{x_r} = \frac{I_w}{r_w}\left(\dot{\omega}_{r,l} + \dot{\omega}_{r,r}\right) + f_r F_{z_r} \quad (38)$$

Considering that the values of F_{x_r} and F_{y_r} have been determined to calculate F_{x_f} and F_{y_f} both sides of "Eq. (34) and Eq. (35)" are multiplied by $\cos\delta$ and $\sin\delta$, respectively, and next, the sum of the sides of two Equations yields:

$$m\left(a_x\cos\delta + a_y\sin\delta\right) = F_{x_f} + \left(F_{x_r} - F_{aero}\right)\cos\delta + F_{y_r}\sin\delta \quad (39)$$

By replacing the equivalent terms for F_{y_r} and F_{x_r} from "Eq. (37) and Eq. (38)" in "Eq. (39)", the value of F_{x_f} can be determined as:

$$F_{x_f} = \left(ma_x + F_{aero} - \frac{I_w \dot{\omega}_r}{r_w} - f_r F_{z_r}\right)\cos\delta + \left(ma_y + \frac{I_z \ddot{\psi} - l_f m a_y}{l}\right)\sin\delta \quad (40)$$

Finally, by replacing the equivalent terms for F_{x_f} and F_{y_r} from "Eq. (40) and Eq. (37)" in "Eq. (35)", the value of F_{y_f} will be obtained as:

$$F_{y_f} = \frac{ma_y - F_{x_f}\sin\delta - F_{y_r}}{\cos\delta} \quad (41)$$

4.1.2. Braking Mode

Considering the traditional braking torque distribution strategy, "Eq. (34)" can be written as:

$$ma_x = (\gamma + \cos\delta)F_{x_f} - F_{y_f}\sin\delta - F_{aero} \quad (42)$$

Now multiplying the sides of "Eq. (35) and Eq. (42)" by $\sin\delta$ and $\cos\delta$, respectively, and then adding the two sides of the resulting Equations together yields:

$$m(a_x\cos\delta + a_y\sin\delta) = (\gamma\cos\delta + 1)F_{x_f} - F_{aero}\cos\delta + F_{y_r}\sin\delta \quad (43)$$

By replacing F_{y_r} from "Eq. (37)" in "Eq. (43)" and making appropriate simplifications for F_{x_f}, the "Eq. (44)" will be obtained as:

$$F_{x_f} = \left[\frac{(ma_x + F_{aero})\cos\delta + \left(\frac{I_z\ddot{\psi} + l_r m a_y}{l}\right)\sin\delta}{(\gamma\cos\delta + 1)}\right] \quad (44)$$

By replacing the equivalent terms for F_{x_f} and F_{y_r} from (45) and (37) in "Eq. (41)", the value of F_{y_f} can be determined. Until this stage, the values of F_{x_f}, F_{x_r}, F_{y_f}, F_{y_r} have been determined.

4.2. Calculation of Tire Friction Coefficients

According to "Eq. (28), Eq. (29), and (33)", it can be seen that it is not necessary to calculate the tire-road friction coefficients to determine the control inputs at any moment. However, to check the accuracy of the considered tire model and to evaluate the method of estimating the longitudinal and lateral forces of the tire, in this section, the method of calculating the friction coefficient of front axle tires ($\mu_{f,l}$ and $\mu_{f,r}$) will be explained. Similarly, the friction coefficient values of rear axle tires ($\mu_{r,l}$ and $\mu_{r,r}$) can be calculated. To calculate the friction coefficient of the front axle tires ($\mu_{f,l}$ and $\mu_{f,r}$), the longitudinal and lateral forces of each of the front axle tires should be calculated. In the dynamic model section, it was stated that for each axis, the longitudinal forces of the left and right tires are almost equal.

$$F_{x_{\tau,l}} \approx F_{x_{\tau,r}} \approx \frac{F_{x_\tau}}{2}, \quad \tau \in \{f, r\} \quad (45)$$

Using "Eq. (5), Eq. (11), and Eq. (47)" for the front tires, we have:

$$\frac{F_{x_f}}{2} = \sigma_{x_{f,l}}\frac{\mu_{f,l}}{\sigma_{f,l}}F_{z_{f,l}} \quad (46)$$

$$\frac{F_{x_f}}{2} = \sigma_{x_{f,r}}\frac{\mu_{f,r}}{\sigma_{f,r}}F_{z_{f,r}} \quad (47)$$

$$F_{y_{f,l}} = \sigma_{y_f}\frac{\mu_{f,l}}{\sigma_{f,l}}F_{z_{f,l}} \quad (48)$$

$$F_{y_{f,r}} = \sigma_{y_f}\frac{\mu_{f,r}}{\sigma_{f,r}}F_{z_{f,r}} \quad (49)$$

By dividing both sides of "Eq. (47)" by "Eq. (48)" and dividing "Eq. (49)" by "Eq. (50)", "Eq. (51) and Eq. (52)" will be obtained, respectively.

$$\frac{\sigma_{x_{f,r}}}{\sigma_{x_{f,l}}} = \frac{\sigma_{f,r}}{\sigma_{f,l}}\frac{\mu_{f,l}}{\mu_{f,r}}\frac{F_{z_{f,l}}}{F_{z_{f,r}}} \quad (50)$$

$$\frac{F_{y_{f,l}}}{F_{y_{f,r}}} = \frac{\sigma_{f,r}}{\sigma_{f,l}}\frac{\mu_{f,l}}{\mu_{f,r}}\frac{F_{z_{f,l}}}{F_{z_{f,r}}} \quad (51)$$

By combining "Eq. (51) and Eq. (52)", between the lateral force of the front tires, "Eq. (53)" is obtained.

$$\frac{F_{y_{f,l}}}{F_{y_{f,r}}} = \frac{\sigma_{x_{f,r}}}{\sigma_{x_{f,l}}} \quad (52)$$

Considering that the value of F_{y_f} is known, the lateral force of each of these tires can be calculated using "Eq. (53)". By determining the normal force, longitudinal force, and lateral force of each of the front tires, the approximate value of the tire-road friction coefficient of each of these tires can be calculated as:

$$\mu_{f,\varepsilon} = \frac{\sqrt{\left(F_{x_{f,\varepsilon}}\right)^2 + \left(F_{y_{f,\varepsilon}}\right)^2}}{F_{z_{f,\varepsilon}}}, \quad \varepsilon \in \{l, r\} \tag{53}$$

5 OBTAINED RESULTS

To evaluate the effectiveness of the proposed adaptive control, CarSim and MATLAB/Simulink software packages have been used. The dynamic model used for simulation has 14 degrees of freedom to include the dynamics of the suspension system, brake system, power chain, steering system, and the dynamics of the steering wheel actuator. Pacejka 5.2 (Symmetric) tire model is also used for tires. The vehicle used in the simulations is a typical D-class sedan with default parameters from CarSim database.

The block diagram of longitudinal-lateral adaptive integrated control is shown in Fig. 3. To evaluate the performance of the control algorithm in conditions closer to reality, the Vehicle State Calculation block is considered. This block is responsible for estimating the speed, filtering the noise of the sensors, and calculating some vehicle states. In this simulation, it is presumed that longitudinal acceleration, lateral acceleration, and steering angle rate are measured by IMU and have noise. To consider the effect of noise, the Band-Limited White Noise block of Simulink is used. It is also assumed that the coordinates of the vehicle CG, wheel speed, and gear ratio are accessible. The considered noise power value for $\dot{\psi}$, a_x and a_y is equal to 0.001 deg/sec, $0.5 \times 10^{-6} g$ and $10^{-6} g$, respectively. A 1st order low-pass Butterworth filter with a pass frequency of 10 Hz was used for filtering. For the steering wheel angle, the saturation limit is ±10 deg. In the simulation, the steering wheel angular position actuator's dynamics is also considered a second-order transfer function with a natural frequency of 6.3 Hz and damping of 0.95 [45]. The reference method [30] has also been used to estimate longitudinal and lateral velocities.

To evaluate the performance of the integrated control proposed in this section, three different maneuvers have been planned, including moving on a curved road, the critical lane change in braking mode, and the critical lane change in traction mode. In the following, the details of the obtained results of these scenarios are described in detail.

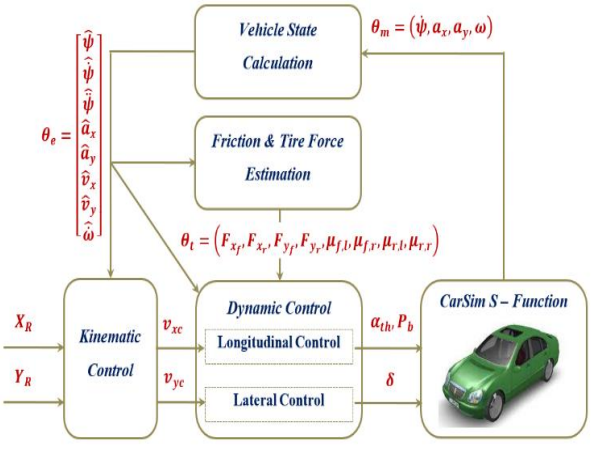

Fig. 6 Block diagram of integrated longitudinal and lateral control.

5.1. Maneuver I: Constant Speed on A Curved Road

In this maneuver, the vehicle speed is assumed to be constant and equal to 36 km/h. Figure 4a shows the desired path and the direction of the vehicle. With a general look, it can be said that the desired path of the vehicle has been followed with appropriate accuracy. In order to investigate the tracking more precisely, the longitudinal and lateral tracking errors are shown in "Fig. 4c and Fig. 4d", respectively. According to these figures, it can be seen that the maximum of longitudinal and lateral tracking errors is insignificant and is around 0.4 m. In the part with the curved path, as expected, the steering angle of the wheel is almost constant and its value is equal to 1.6 deg ("Fig. 4-b"). Considering the constant speed during the maneuver, it is expected that the amount of throttle opening and the torque applied to the wheels will be constant. Examining "Fig. 4e and Fig. 4f" confirms this point well. The amount of throttle opening is 10%, and the amount of torque applied to each front wheel is 20 N.m.

5.2. Maneuver Ii: Lane Change with Braking

This maneuver is planned to evaluate the integrated control performance in high-speed braking maneuvers. The vehicle's initial speed is assumed to be 140 km/h. It is assumed that the vehicle first moves for 3 seconds with a constant braking acceleration of -2.5 m/sec^2 and then changes lanes with the same braking acceleration. After the lane change, the vehicle continues to move with the same acceleration for 10 seconds ("Fig. 5").

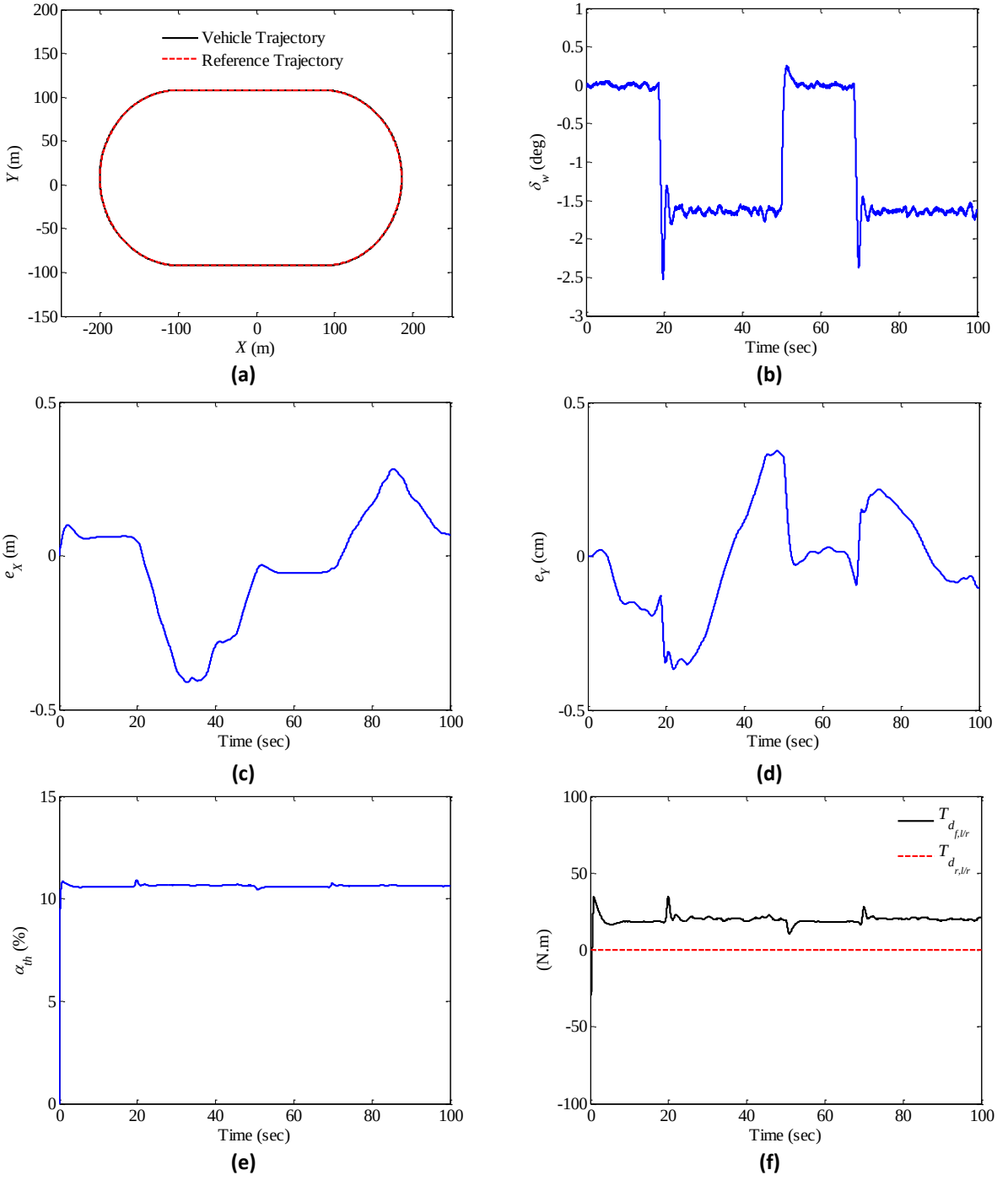

Fig. 4 Integrated control performance in the curved path: (a): reference path and vehicle path, (b): steering wheel angle, (c): longitudinal tracking error, (d): lateral tracking error, (e): throttle opening percentage, and (f): traction torque applied to the wheels.

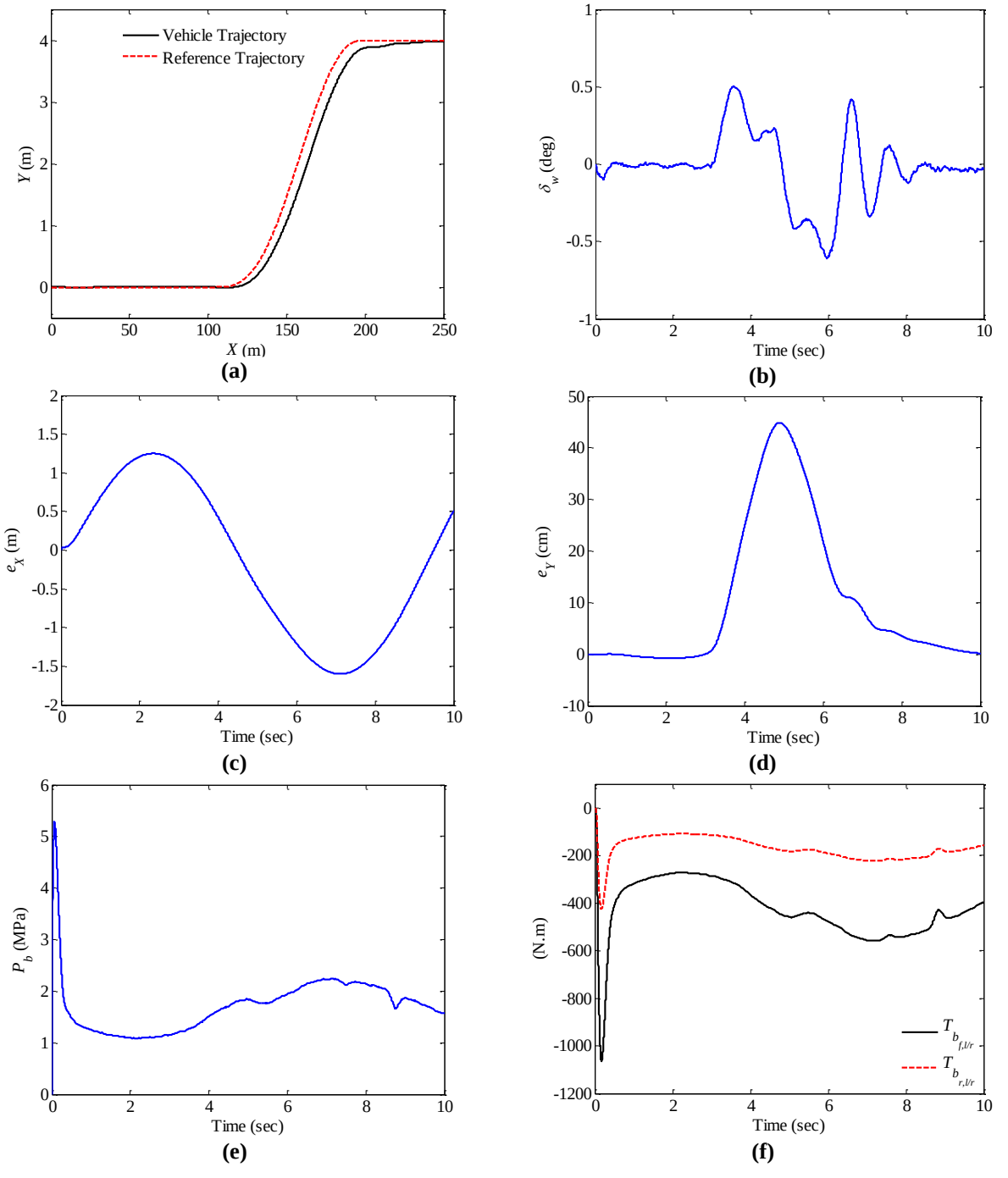

Fig. 5 Integrated control performance in braking lane change: (a): reference path and vehicle path, (b): steering wheel angle, (c): longitudinal tracking error, (d): lateral tracking error, (e): master cylinder brake pressure, and (f): braking torque

5.3. Maneuver Iii: Lane Change with Accelerating

The characteristics of the maneuver are shown in "Fig. 6 and Fig. 7a". This maneuver includes two lane changes, the first lane change is done with a constant acceleration of 1.5 m/sec^2, and the second lane change is done with a constant speed. The changes in the maximum available tire-road friction coefficient ($\mu_{ro,max}$) in terms of the longitudinal position of the road are presented in "Fig. 6a". In the middle of the first lane change (150 m to 155 m), $\mu_{ro,max}$ changes from 0.9 to 0.7. Also, In the middle of the second lane change (410 m to 415 m), $\mu_{ro,max}$ decreases from 0.7 to 0.4. The initial speed of the vehicle is 100 km/h.

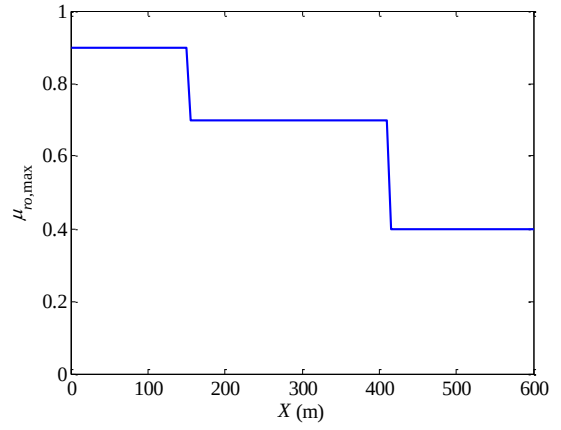

(a)

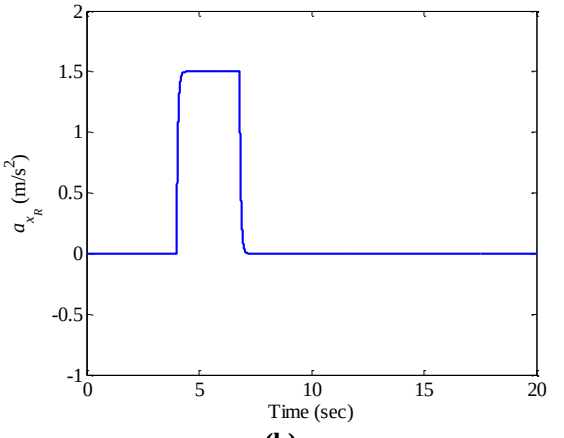

(b)

Fig. 6 Traction Lane change maneuver: (a): variations of road friction coefficient, and (b): reference longitudinal acceleration.

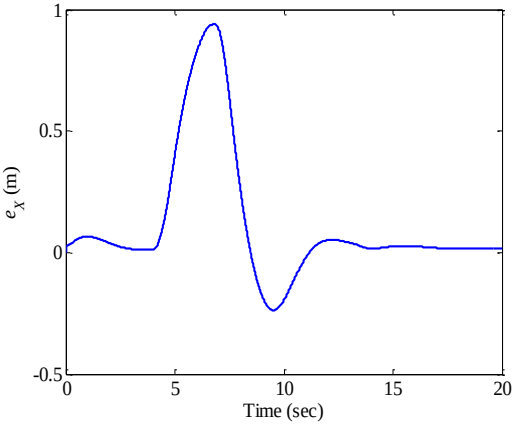

(b)

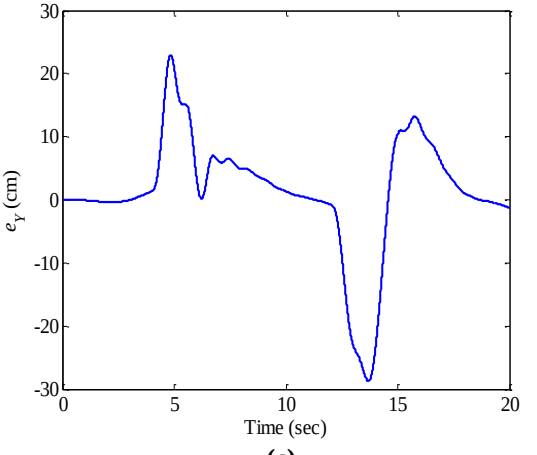

(c)

Fig. 7 The complete performance of the integrated control in lane change: (a): reference path and vehicle path, (b): longitudinal tracking error, and (c): lateral tracking error.

The vehicle motion path and tracking errors are shown in "Fig. 7". It can be seen in this figure that the desired motion path has been followed well and with little error. The maximum longitudinal tracking error is less than 1 m ("Fig. 7b"), and the maximum lateral tracking error is less than 30 cm ("Fig. 7c").

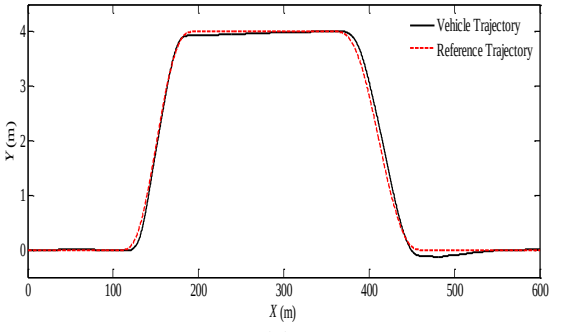

(a)

The longitudinal and lateral control inputs are also shown in "Fig. 8a and Fig. 8b", respectively.

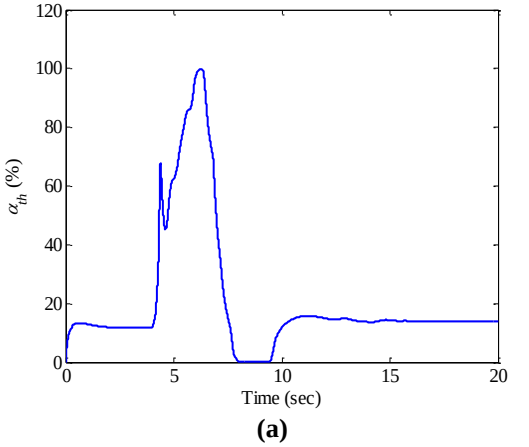

(a)

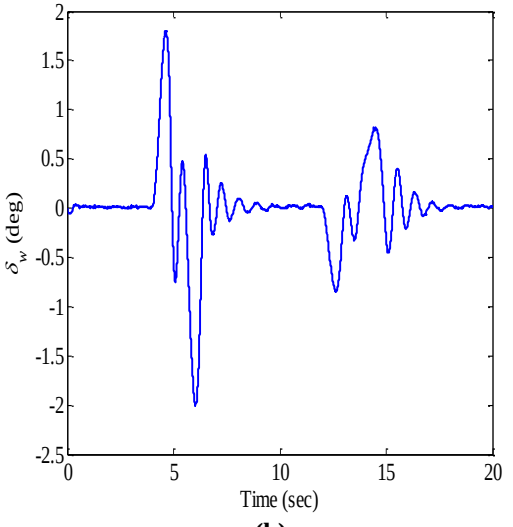

(b)

Fig. 8 Integrated control inputs in traction lane change: (a): Throttle valve opening percentage, and (b): Wheel steering angle.

In order to assess the changes in the longitudinal and lateral speed variations and the accuracy of the speed estimation, the longitudinal and lateral speeds of the vehicle, along with their estimated values, are shown in "Fig. 9a and Fig. 9b", respectively.

Finally, car friction coefficients and their estimated values are presented in "Fig. 10." The accuracy of the tire friction coefficient estimation can be assessed by examining "Fig. 10". In "Fig. 10b", it can be observed that the friction coefficient of the tire reaches its maximum available value of 0.7 within 6.2 seconds. This indicates that the tire has reached its maximum frictional capacity at this point in time. Considering this finding, it can be concluded that the proposed integrated adaptive control strategy is capable of performing its task effectively and following the desired path with acceptable accuracy, even under critical driving conditions involving changes in road friction and tire dynamic nonlinearities.

One of the key advantages of the proposed control approach is its robustness. The controller was designed based on a 7-degree-of-freedom vehicle model, yet the simulations were conducted using the full vehicle dynamic model. This suggests that the presented control strategy has successfully accounted for various parametric and unmodeled uncertainties, demonstrating its ability to handle the complexity of the actual vehicle dynamics. Furthermore, the ability of the control system to fully utilize the tire's maximum frictional capacity, as evident from the friction coefficient reaching 0.7, implies that the control strategy is effectively managing the available tire-road adhesion.

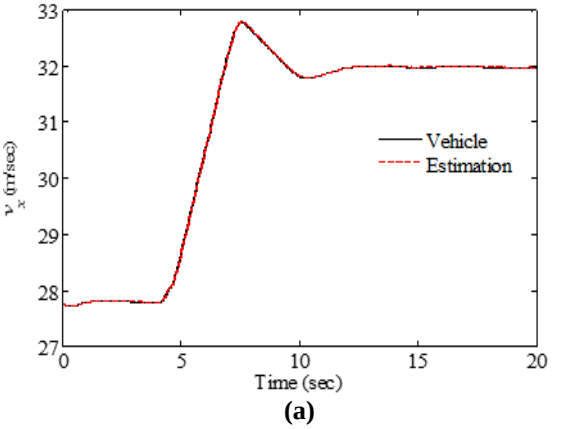

(a)

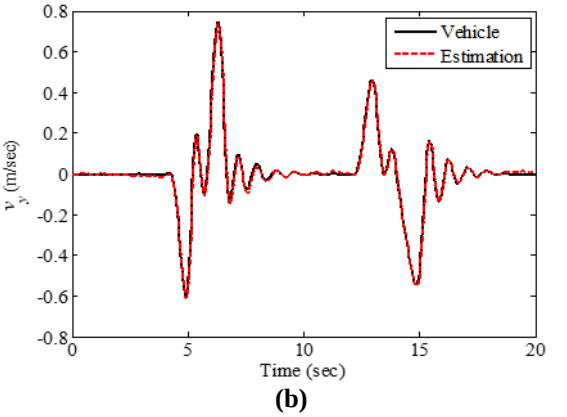

(b)

Fig. 9 Estimation of velocities in traction lane change: (a): longitudinal speed, and (b): lateral speed.

This is a crucial aspect, especially in critical driving scenarios where the vehicle's performance and stability are heavily dependent on the optimal utilization of the tire-road interface. By combining the accurate estimation of the tire friction coefficient, the effective handling of tire dynamic nonlinearities, and the demonstrated robustness against uncertainties, the proposed integrated adaptive control approach shows promise in maintaining the vehicle's desired path-tracking performance and stability, even in challenging driving conditions characterized by changes in road friction and other nonlinear vehicle dynamics.

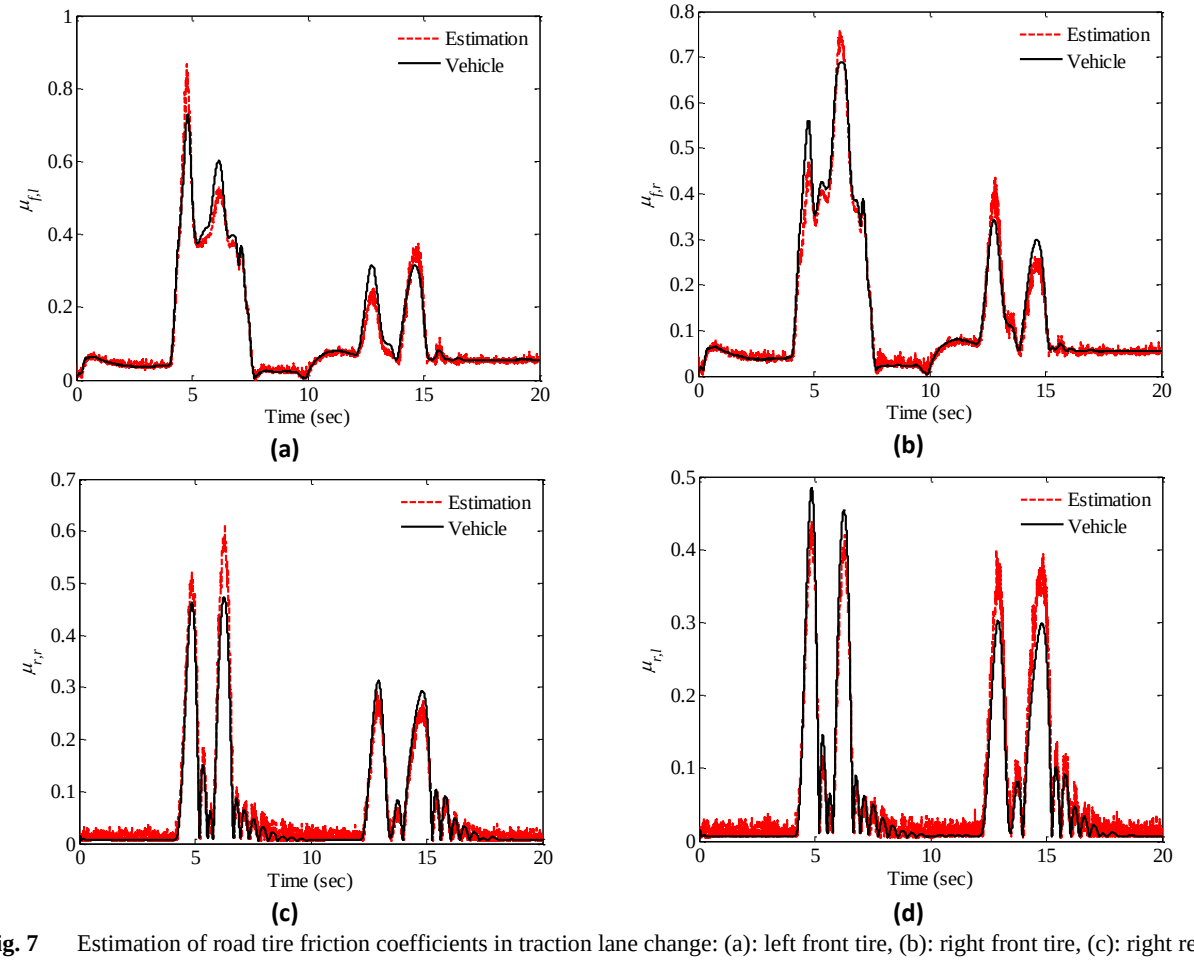

Fig. 7 Estimation of road tire friction coefficients in traction lane change: (a): left front tire, (b): right front tire, (c): right rear tire, and (d): left rear tire.

6 CONCLUSIONS

The proposed adaptive control algorithm represents a significant advancement in managing highly nonlinear vehicle dynamics and sudden changes in friction coefficients. This control strategy has substantial potential for real-world driving applications. The key practical implications include the controller's robustness to accommodate changes in friction coefficient and other uncertainties, as well as its capability to accurately track curved paths. These features are critical for enhancing driving safety and control, especially in challenging road conditions or when integrated with advanced driver assistance systems. The simulation results demonstrate the effectiveness of the integrated adaptive control in managing complex maneuvers, such as constant-speed cornering, lane changes under braking, and lane changes under traction. These findings suggest the controller could be successfully implemented in real-world vehicles, providing enhanced stability and performance. Furthermore, the accurate estimation of the friction coefficient underscores the potential for this control approach to contribute to advanced tire-road interaction models and friction estimation algorithms, with far-reaching implications for vehicle safety and performance systems. For future work, it is recommended to evaluate the controller's performance when integrated with electronic stability control (ESC), as well as to validate the simulation results through extensive testing on physical prototypes. Exploring the controller's behavior under extreme conditions, such as split-μ scenarios, and investigating the potential for incorporating machine learning techniques could further enhance the controller's adaptability and robustness. By addressing these future research directions, the practical applicability and impact of the proposed adaptive control algorithm can be expanded, paving the way for its widespread adoption in real-world vehicle applications.

REFERENCES

[1] Thorpe, C., Herbert, M., Kanade, T., and Shafter, S., Toward Autonomous Driving: the CMU Navlab, II. Architecture and Systems, IEEE Expert, Vol. 6, No. 4, pp. 44-52, 1991, doi: 10.1109/64.85920.

[2] Dickmanns E. D., Zapp, A., Autonomous High Speed Road Vehicle Guidance by Computer Vision1, IFAC Proceedings Volumes, Vol. 20, No. 5, Part. 4, pp. 221-226, 1987/07/01/ 1987, doi: https://doi.org/10.1016/S1474-6670(17)55320-3.

[3] Ni, J., Hu, J., and Xiang, C., A Review for Design and Dynamics Control of Unmanned Ground Vehicle, Proceedings of the Institution of Mechanical Engineers, Part D: Journal of Automobile Engineering, Vol. 235, No. 4, pp. 1084-1100, 2021, doi: 10.1177/0954407020912097.

[4] Road Traffic Injuries, https://www.who.int/news-room/fact-sheets/detail/road-traffic-injuries accessed.

[5] Administration, N. H. T. S., Motor Vehicle Crashes: Overview, Traffic Safety Facts: Research Note, Vol. 2016, 2016, pp. 1-9.

[6] You, F., Zhang, R., Lie, G., Wang, H., Wen, H., and Xu, J., Trajectory Planning and Tracking Control for Autonomous Lane Change Maneuver Based on The Cooperative Vehicle Infrastructure System, Expert Systems with Applications, Vol. 42, No. 14, pp. 5932-5946, 2015.

[7] Dixit S., et al., Trajectory Planning and Tracking for Autonomous Overtaking: State-of-The-Art and Future Prospects, Annual Reviews in Control, Vol. 45, pp. 76-86, 2018/01/01/ 2018, doi: https://doi.org/10.1016/j.arcontrol.2018.02.001.

[8] Wang, L., Zhao, X., Su, H., and Tang, G., Lane Changing Trajectory Planning and Tracking Control for Intelligent Vehicle on Curved Road, SpringerPlus, Vol. 5, No. 1, 2016, pp. 1150.

[9] Kayacan, E., Ramon, H., and Saeys, W., Robust Trajectory Tracking Error Model-Based Predictive Control for Unmanned Ground Vehicles, IEEE/ASME Transactions on Mechatronics, Vol. 21, No. 2, 2016, pp. 806-814, doi: 10.1109/TMECH.2015.2492984.

[10] Petrov P., Nashashibi, F., Modeling and Nonlinear Adaptive Control for Autonomous Vehicle Overtaking, IEEE Transactions on Intelligent Transportation Systems, Vol. 15, No. 4, pp. 1643-1656, 2014, doi: 10.1109/TITS.2014.2303995.

[11] Wnag, C., Zhao, W., Xu, Z., and Zhou, G., Path Planning and Stability Control of Collision Avoidance System Based on Active Front Steering, Science China Technological Sciences, Vol. 60, No. 8, pp. 1231-1243, 2017.

[12] Rasekhipour, Y., Khajepour, A., Chen, S. K., and Litkouhi, B., A Potential Field-Based Model Predictive Path-Planning Controller for Autonomous Road Vehicles, IEEE Transactions on Intelligent Transportation Systems, Vol. 18, No. 5, pp. 1255-1267, 2016.

[13] Suh, J., Chae, H., and Yi, K., Stochastic Model-Predictive Control for Lane Change Decision of Automated Driving Vehicles, IEEE Transactions on Vehicular Technology, Vol. 67, No. 6, pp. 4771-4782, 2018, doi: 10.1109/TVT.2018.2804891.

[14] Cai, J., Jiang, H., Chen, L., Liu, J., Cai, Y., and Wang, J., Implementation and Development of a Trajectory Tracking Control System for Intelligent Vehicle, Journal of Intelligent & Robotic Systems, 2018/05/09 2018, doi: 10.1007/s10846-018-0834-4.

[15] Feng, P., Jin, H., Zhao, L., and Lu, M., Active Lane-Changing Control of Intelligent Vehicle on Curved Section of Expressway, Modelling and Simulation in Engineering, Vol. 2022, 2022.

[16] Xiong, L., Yang, X., Leng, B., Zhang, R., Fu, Z., and Zhuo, G., Integrated longitudinal and lateral control for autonomous vehicles with active load transfer strategy at the handling limits, Proceedings of the Institution of Mechanical Engineers, Part D: Journal of Automobile Engineering, Vol. 235, No. 4, 2021, pp. 961-974.

[17] Wang, H., Zhang, T., Zhang, X., and Li, Q., Observer-Based Path Tracking Controller Design for Autonomous Ground Vehicles with Input Saturation, IEEE/CAA Journal of Automatica Sinica, Vol. 9, 2022, pp. 1-13.

[18] Hossain, T., Habibullah, H., and Islam, R., Steering and Speed Control System Design for Autonomous Vehicles by Developing an Optimal Hybrid Controller to Track Reference Trajectory, Machines, Vol. 10, No. 6, 2022, pp. 420.

[19] Guo, J., Hu, P., and Wang, R., Nonlinear Coordinated Steering and Braking Control of Vision-Based Autonomous Vehicles in Emergency Obstacle Avoidance, IEEE Transactions on Intelligent Transportation Systems, Vol. 17, No. 11, 2016, pp. 3230-3240, doi: 10.1109/TITS.2016.2544791.

[20] Choi, J., Yi, K., Suh, J., and Ko, B., Coordinated Control of Motor-Driven Power Steering Torque Overlay and Differential Braking for Emergency Driving Support, IEEE Transactions on Vehicular Technology, Vol. 63, No. 2, 2014, pp. 566-579, doi: 10.1109/TVT.2013.2279719.

[21] Funke, J., Brown, M., Erlien, S. M., and Gerdes, J. C., Collision Avoidance and Stabilization for Autonomous Vehicles in Emergency Scenarios, IEEE Transactions on Control Systems Technology, Vol. 25, No. 4, 2017, pp. 1204-1216, doi: 10.1109/TCST.2016.2599783.

[22] Song, J., Development and Comparison of Integrated Dynamics Control Systems with Fuzzy Logic Control and Sliding Mode Control, J. Mech Sci Technol, Vol. 27, No. 6, 2013, pp. 1853-1861.

[23] Zhang, Z., Wang, C., Zhao, W., and Feng, J., Longitudinal and Lateral Collision Avoidance Control Strategy for Intelligent Vehicles, Proceedings of the Institution of Mechanical Engineers, Part D: Journal of Automobile Engineering, 2022, pp. 09544070211024048.

[24] Chen, R., Chen, Z., Duan, Y., Wu, DJ., and Zhang, Y., Coupled Longitudinal and Lateral Control for Trajectory

Tracking of Autonomous Vehicle Based on LTV-MPC Approach, SAE Technical Paper, 0148-7191, 2022.

[25] Li, Z., Chen, Liu, H., Wang, P., and Gong, X., Integrated Longitudinal and Lateral Vehicle Stability Control for Extreme Conditions With Safety Dynamic Requirements Analysis, IEEE Transactions on Intelligent Transportation Systems, 2022.

[26] Li, Z., Wang, P., Cai, S., Hu, X., and Chen, H., NMPC-Based Controller for Vehicle Longitudinal and Lateral Stability Enhancement Under Extreme Driving Conditions, ISA Transactions, Vol. 135, 2023, pp. 509-523.

[27] Attia, R., Orjuela, R., and Basset, M., Combined Longitudinal and Lateral Control for Automated Vehicle Guidance, Vehicle System Dynamics, Vol. 52, No. 2, 2014, pp. 261-279, doi: 10.1080/00423114.2013.874563.

[28] Liu, Y., Pei, Guo X., Chen, C., and Zhou, H., An Integration Planning and Control Method of Intelligent Vehicles Based on The Iterative Linear Quadratic Regulator, Journal of the Franklin Institute, Vol. 361, No. 1, 2024, pp. 265-282.

[29] Jin, X., Wang, Q., Yan, Z., Yang, H., and Yin, G., Integrated Robust Control of Path Following and Lateral Stability for Autonomous in-Wheel-Motor-Driven Electric Vehicles, Proceedings of the Institution of Mechanical Engineers, Part D: Journal of Automobile Engineering, 2024, pp. 09544070241227266.

[30] Sazgar, H., Azadi, S., and Kazemi, R., and Khalaji, A. K., Integrated Longitudinal and Lateral Guidance of Vehicles in Critical High Speed Maneuvers, Proceedings of the Institution of Mechanical Engineers, Part K: Journal of Multi-body Dynamics, Vol. 233, No. 4, 2019, pp. 994-1013, doi: 10.1177/1464419319847916.

[31] Sazgar, H., Azadi, S., and Kazemi, R., Trajectory Planning and Combined Control Design for Critical High-Speed Lane Change Maneuvers, Proceedings of the Institution of Mechanical Engineers, Part D: Journal of Automobile Engineering, Vol. 234, No. 2-3, 2020, pp. 823-839, doi: 10.1177/0954407019845253.

[32] Sazgar, H., Khalaji, A. K., Nonlinear Integrated Control with Friction Estimation for Automatic Lane Change on The Highways, Proceedings of the Institution of Mechanical Engineers, Part K: Journal of Multi-body Dynamics, Vol. 236, No. 3, 2022, pp. 453-469.

[33] Rajamani, R., Vehicle Dynamics and Control. Springer Science & Business Media, 2011.

[34] Kiencke, U., Nielsen, L., Automotive Control Systems: for Engine, Driveline, and Vehicle, ed: IOP Publishing, 2000.

[35] Pacejka H., Besselink, I., Tire, and Vehicle Dynamics. Elsevier Science, 2012.

[36] Hwan J. J., et al., Optimal Motion Planning with the Half-Car Dynamical Model for Autonomous High-Speed Driving, in 2013 American Control Conference, Vol. 17-19, 2013, pp. 188-193, doi: 10.1109/ACC.2013.6579835.

[37] Velenis, E., Tsiotras, P., and Lu, J., Optimality Properties and Driver Input Parameterization for Trail-Braking Cornering, European Journal of Control, Vol. 14, No. 4, 2008, pp. 308-320.

[38] Bakker, E., Nyborg, L., and Pacejka, H. B., Tyre Modelling for Use in Vehicle Dynamics Studies, 1987. [Online], Available: https://doi.org/10.4271/870421.

[39] Milanés, V., González, C., Naranjo, J., Onieva, E., and De Pedro, T., Electro-Hydraulic Braking System for Autonomous Vehicles, International Journal of Automotive Technology, Vol. 11, No. 1, 2010, pp. 89-95.

[40] Khaleghian, S., Emami, A., and Taheri, S., A Technical Survey on Tire-Road Friction Estimation, Friction, Vol. 5, No. 2, 2017, pp. 123-146.

[41] Singh, K. B., Arat, M. A., and Taheri, S., Literature Review and Fundamental Approaches for Vehicle and Tire State Estimation, Vehicle System Dynamics, 2018, pp. 1-23.

[42] Guo, H., Yin, Z., Cao, D., Chen, H., and Lv, C., A Review of Estimation for Vehicle Tire-Road Interactions Toward Automated Driving, IEEE Transactions on Systems, Man, and Cybernetics: Systems, No. 99, 2018, pp. 1-17.

[43] Peng, Y., Chen, J., and Ma, Y., Observer-Based Estimation of Velocity and Tire-Road Friction Coefficient for Vehicle Control Systems, Nonlinear Dynamics, Journal article, Vol. 96, No. 1, 2019, pp. 363-387, doi: 10.1007/s11071-019-04794-0.

[44] Beal, C. E., Rapid Road Friction Estimation using Independent Left/Right Steering Torque Measurements, Vehicle System Dynamics, 2019, pp. 1-27, doi: 10.1080/00423114.2019.1580377.

[45] Cerone, V., Milanese, M., and D. Regruto, Combined Automatic Lane-Keeping and Driver's Steering through a 2-DOF Control Strategy, IEEE Transactions on Control Systems Technology, Vol. 17, No. 1, 2008, pp. 135-142.